6-28-2018

Structure-Function Relationships in Hexacoordinate Heme Proteins: Mechanism of Cytoglobin Interactions with Exogenous Ligands

Antonija Tangar
Florida International University, atangar@yahoo.com

DOI: 10.25148/etd.FIDC006907

FLORIDA INTERNATIONAL UNIVERSITY

Miami, Florida

STRUCTURE-FUNCTION RELATIONSHIPS IN HEXACOORDINATE HEME PROTEINS: MECHANISM OF CYTOGLOBIN INTERACTIONS WITH EXOGENOUS LIGANDS

A dissertation submitted in partial fulfillment of the

requirements for the degree of

DOCTOR OF PHILOSOPHY

in

CHEMISTRY

by

Antonija Tangar

2018

To: Dean Michael R. Heithaus
College of Arts, Sciences and Education

This dissertation, written by Antonija Tangar, and entitled Structure-Function Relationships in Hexacoordinate Heme Proteins: Mechanism of Cytoglobin Interactions with Exogenous Ligands, having been approved in respect to style and intellectual content, is referred to you for your judgement.

We have read this dissertation and recommend that it be approved.

_____
Xiaotang Wang

_____
Yi Xiao

_____
David Chatfield

_____
Prem Chapagain

_____
Jaroslava Miksovska, Major Professor

Date of Defense: June 28, 2018

The dissertation of Antonija Tangar is approved.

_____
Dean Michael R. Heithaus
College of Arts, Sciences and Education

_____
Andrés G. Gil
Vice President for Research and Economic Development
and Dean of the University Graduate School

DEDICATION

I dedicate this work to the memory of my grandmother,

the wisest and kindest person I have ever met

ACKNOWLEDGMENTS

First and foremost, I would like to express sincere gratitude to my advisor Dr. Jaroslava Miksovska, for providing me with the knowledge and tools to pursue my projects, for encouraging independent work, professional development and overall continuous support. In addition, I would like to thank my committee members, Dr. Prem Chapagain, Dr. David Chatfield, Dr. Xiaotang Wang, Dr and Yi Xiao, as well as Dr. Alexander Morozov, for insightful discussions and suggestions over the years. I would also like to acknowledge my former instructors Kathy Smith and Dr. Donna Gosnell, who inspired me to pursue biochemistry research.

Over the course of my graduate studies, the members of the Miksovska group have become my close friends. I wish to thank my former and current lab mates: Dr. Luisana Astudillo, Dr. Walter Gonzalez, Dr. Khoa Pham, Dr. David Butcher, Ruipeng Lei, Maria Santiago, Samiol Azam and Setareh Sakhdari, for helpful advice and fun times in the lab. I also need to acknowledge my high school and undergraduate students, especially Michael Gonçalves and Jessica Lopez, for their dedication and help with my projects.

This dissertation would not be possible without the enormous support system I was lucky to have. I have to thank all of my friends and family for believing in me and encouraging me. I am eternally grateful to Mirella Fenner and her family for loving, teaching, and caring for Izzy while I was at work.

A very special thanks to my parents and sisters for their never ending support, advice, encouragement and all of the sacrifices that they have made on my behalf. Thank you for showing me what it means to work hard and to be resilient. You have taught and given me everything.

Last but not the least, I would like to thank my husband, for his love, understanding, patience, and support, and most importantly for giving me my daughter, the light of my life, my motivation and inspiration. I love you both to the moon and back.

ABSTRACT OF THE DISSERTATION

STRUCTURE-FUNCTION RELATIONSHIPS IN HEXACOORDINATE HEME PROTEINS: MECHANISM OF CYTOGLOBIN INTERACTIONS WITH EXOGENOUS LIGANDS

by

Antonija Tangar

Florida International University, 2018

Miami, Florida

Professor Jaroslava Miksovska, Major Professor

Cytoglobin (Cygb) and neuroglobin (Ngb) are among the newest members of vertebrate globin family characterized by a classical 3-over-3 α-helical fold and a heme prosthetic group capable of reversibly binding small ligands such as O_2, CO and NO. The physiological functions of Cygb and Ngb remain to be determined; however, current data suggest that both proteins have a significant role in cytoprotection in hypoxic and genotoxic conditions. Cytoglobin and Ngb are distinct from their better-known counterparts, hemoglobin (Hb) and myoglobin (Mb), in several structural features. First, in the absence of an external ligand, the sixth coordination site of the heme iron in Cygb and Ngb is occupied by a distal histidine residue, leading to a complex ligand rebinding mechanism dependent on the rate of distal His dissociation from the heme iron. Although hexacoordination was observed before in plant and bacterial hemoglobins, the

physiological role of this feature remains unknown. Second, both Ngb and Cygb are capable of forming an intraprotein disulfide bond, which has been shown to regulate ligand binding affinity, leading to a hypothesis that intracellular function of these proteins is redox-dependent. Lastly, Cygb contains ~20 amino acid long extensions on both N- and C- termini, a unique feature among vertebrate globins with unknown physiological function.

The work presented in the dissertation reveals that hexacoordinate heme reactivity is distinct from that of pentacoordinate heme and is strongly influenced by the distal histidine residue and the disulfide bond. In the case of human Cygb, experimental and computational approaches demonstrated that the disulfide bond regulates the flexibility of the N terminus and the accessibility of the 1,8-ANS binding site. Furthermore, molecular dynamics of the hexa- and pentacoordinate human Ngb were probed computationally to elucidate structural requirements that govern signal transmission between CD loop and the distal pocket. Lastly, Ngb and Cygb were reconstituted with fluorescent analog of the native heme group to produce hexacoordinate variants with favorable photophysical properties that can be used to characterize protein-protein interactions.

TABLE OF CONTENTS

CHAPTER PAGE

LIST OF TABLES

TABLE PAGE

LIST OF FIGURES

FIGURE PAGE

LIST OF ABBREVIATIONS AND ACRONYMS

ABBREVIATION	FULL NAME
1,8-ANS	1-anilinonaphtalene-8-sulfonic acid
AHb3	Truncated hemoglobin from *A. thaliana*
CO	Carbon monoxide
CygbWT	Cytoglobin wild-type with the disulfide bond
FePPIX	Iron protoporphyrin IX
Hb	Hemoglobin
HbA	Human hemoglobin
$hCygbWT^{ox}$	Human CygbWT with oxidized disulfide bond
$hCygbWT^{red}$	Human CygbWT with reduced disulfide bond
hhMb	Horse heart myoglobin
GuHCl	Guanidine hydrochloride
HisE7	Distal histidine
HisF8	Proximal histidine
$hNgbWT^{ox}$	Human NgbWT with oxidized disulfide bond
$hNgbWT^{red}$	Human NgbWT with reduced disulfide bond
k_{-H}	Distal histidine rate of dissociation
K_d	Dissociation constant
Mb	Myoglobin
NgbWT	Neuroglobin wild-type with the disulfide bond
NiR	Nitrite reductase

NO	Nitric oxide
NOD	Nitric oxide reductase
O_2	Oxygen
PDB	Protein Data Bank
Φ_F	Fluorescence quantum yield
Φ_P	Phosphoresence quantum yield
ROS	Reactive oxygen species
RMSD	Root mean square deviation
swMb	Sperm whale myoglobin
SHG	Second harmonic generator
TA	Transient absorption
ZnPPIX	Zinc protoporphyrin IX

1. INTRODUCTION

Porphyrin is a biologically ubiquitous molecule that serves as a building block for heme cofactors. The structure of the porphyrin macrocycle is formed by four methine-linked pyrrole rings coordinated to a metal center (Figure 1.1). Each pyrrole is able to accommodate two substituent groups of varying size and charge, generating heme classes of differing reactivity and spectral signature (Marks 1969). When bound to a protein moiety, the heme prosthetic group is found at the center of fundamental physiological functions such as electron transfer (cytochromes), NO production (NO synthases), hydrogen peroxide decomposition (catalases, peroxidases), as well as ligand sensing (FixL, CooA, soluble guanylyl cyclase), oxygen storage (myoglobin) and transport (hemoglobin).

Physico-chemical and structural requirements that govern heme-mediated reactions remained elusive until the Nobel prize-winning discovery of the three-dimensional structures of hemoglobin (Hb) and myoglobin (Mb) (Kendrew et al. 1960; Perutz et al. 1960). These landmark studies provided for the first time atomic-level insight into heme-protein complex and subsequently allowed correlation between the protein structure and function. As a result, Mb and Hb are among the most extensively studied proteins to date and serve as model systems for ligand binding, protein folding and allosteric modulation mechanisms.

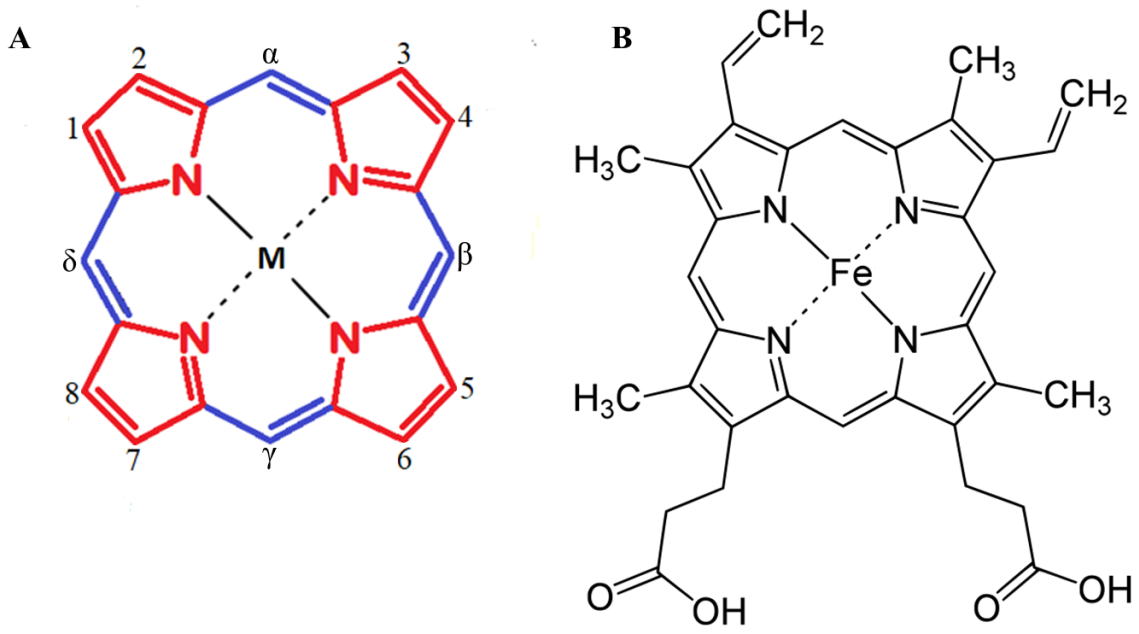

Figure 1.1. (A) Porphyrin is composed of pyrrole rings (red), methine bridges (blue; α, β, γ, δ) and a central metal ion, M. Conventional enumeration for the substituent group positions (1-8) is shown. (B) The structure of iron protoporphyrin IX, heme cofactor found in globins.

1.1 Myoglobin and Hemoglobin

Globins are a functionally versatile superfamily of proteins that reversibly bind small ligands such as O_2, CO and NO. Human Hb (HbA) acts as an oxygen-transport protein expressed in high concentrations (20 mM heme) in red blood cells (Romero et al. 2003). The quaternary structure of HbA shows a symmetrical arrangement of two α and two β globin subunits. The individual HbA subunits share sequence homology (~25 %) and similar ligand affinity (P_{50} ~1 torr) with Mb. However, when assembled into a noncovalently-interacting αβαβ tetramer, affinity for oxygen decreases (P_{50}~ 22 torr) and binding becomes cooperative. Several external factors were found to modulate oxygen binding to HbA, including pH and/or allosteric effectors, such as 2,3-biphosphoglyceric acid.

In comparison, human Mb is an oxygen-storing monomer (P_{50} ~1 torr) found predominantly in the cytoplasm of skeletal and cardiac muscles, with intracellular concentrations ranging from 100-350 μM (J. B. Wittenberg and Wittenberg 1990). Lawrie was the first to observe that Mb concentration is proportional to the cytochrome *c* oxidase and ATP content in red muscles (Lawrie 1953), pointing towards intercommunication between Mb and mitochondria. Although it has been postulated that Mb mediates delivery of O_2 to cytochrome *c* oxidase and consequently supports ATP generation (B. A. Wittenberg and Wittenberg 1987), the role of Mb in intracellular O_2 transport is still debated (Papadopoulos et al. 2001).

Both Hb and Mb have been proposed to have a secondary role in nitric oxide metabolism via NO dioxygenase (NOD) and nitrite reductase (NiR) functions (Doyle and Hoekstra 1981; Gardner 2012). Interestingly, NO dioxygenation was found to be an ancient function of the globin superfamily (Vinogradov and Moens 2008), suggesting that globins were initially involved in detoxification and sensing, rather than ligand storage or transport. In addition to acting as NO sinks, Mb and Hb are capable of generating NO, especially under the conditions of low O_2 concentrations, which induces vasodilation and therefore regulates access of oxygenated blood to the hypoxic tissues (Cosby et al. 2003; Shiva et al. 2007).

NOD reaction: $Fe^{2+} - O_2 + NO \rightleftharpoons Fe^{3+} - ONOO^- \rightarrow Fe^{3+} + NO_3^-$

NiR reaction: $Fe^{2+} + NO_2^- \rightarrow Fe^{3+} + OH^- + NO$

1.2 Newest members of the vertebrate globin family

In the last two decades, bioinformatic analysis of vertebrate genomes revealed the existence of additional globins, namely neuroglobin (Ngb) (Burmester et al. 2000), cytoglobin (Cygb) (Burmester et al. 2002; Kawada et al. 2001; Trent and Hargrove 2002), globin E (GbE) (Kugelstadt et al. 2004), globin X (GbX) (Roesner et al. 2005), globin Y (GbY) (Fuchs, Burmester, and Hankeln 2006) and androglobin (Adgb) (Hoogewijs et al. 2012). The newly discovered globins are diverse in taxonomic and tissue distribution. For example, GbE is found in the eyes of birds (Blank, Kiger, et al. 2011; Kugelstadt et al. 2004), whereas GbX is found in fish, amphibians and reptiles with variable expression patterns across different species (Blank, Wollberg, et al. 2011; Corti et al. 2016; Dröge and Makałowski 2011; Roesner et al. 2005). Androglobin is abundant in mammalian testes (Hoogewijs et al. 2012), whereas GbY has only been observed in a few jawed vertebrates (Storz, Opazo, and Hoffmann 2011). Limited structural and biophysical data are available on GbE, GbX, GbY and Adgb. However, Cygb and Ngb have received substantial attention from the scientific community, especially following several *in vivo* studies which reported potent cytoprotective properties of these two proteins (Khan et al. 2006; Shaw et al. 2006; Thuy et al. 2016).

1.3 Cytoglobin and neuroglobin

Compared to other vertebrate globins, Cygb displays unprecedented expression across a wide spectrum of organs (Nakatani et al. 2004; Trent and Hargrove 2002). So far, Cygb has been found in the cytoplasm of fibroblast-related cell types such as hepatic stellate cells, chondroblasts, osteoblasts, vascular smooth muscle cells, and pericytes

(Halligan, Jourd'heuil, and Jourd'heuil 2009; Schmidt et al. 2004; Thuy et al. 2016). Furthermore, Cygb was observed in select populations of human and rat neurons, not only in cytoplasm but, surprisingly, in nucleus as well (Hundahl et al. 2013; Reuss et al. 2016; Schmidt et al. 2004). Intracellular concentration of Cygb is low (~1 μM), but increases under hypoxic/genotoxic conditions (John et al. 2014; Schmidt et al. 2004; Shaw et al. 2009). Although the physiological role of Cygb is yet to be determined, several functions have been proposed including tumor suppression (Shivapurkar et al. 2008; Thuy et al. 2016), ROS scavenging (S. Zhang et al. 2017), lipid-based signaling (Reeder, Svistunenko, and Wilson 2011) and collagen synthesis (Schmidt et al. 2004). Similarly to Hb and Mb, Cygb appears to play a role in NO metabolism as well (Halligan, Jourd'heuil, and Jourd'heuil 2009). Zweier group found that Cygb mediates NO generation in hypoxic conditions (H. Li et al. 2012), whereas Kawada and coworkers reported significant accumulation of NO metabolites in Cygb knockdown mice (Thuy et al. 2016).

On the other hand, Ngb expression is associated with cytoplasm and mitochondria (Lechauve et al. 2012) of brain (Burmester et al. 2000), retina (Schmidt et al. 2003), and endocrine tissues (Geuens et al. 2003). The intracellular concentration of Ngb varies, and is estimated to be in submicromolar amounts in brain, but in the 100-200 μM range in the retina (Schmidt et al. 2003). Oxygen binding is pH dependent (Nienhaust, Kriegl, and Nienhaust 2004) and is characterized by a surprisingly fast autoxidation rate (k_{ox}).

$$Fe^{2+} - O_2 \xrightarrow{k_{ox}} Fe^{3+} + O_2^-$$

Similarly to Cygb, Ngb was reported to have cytoprotective properties in conditions of hypoxia (Sun et al. 2001) and oxidative stress (Antao et al. 2010; S. Q. Ye et al. 2009), although the underlying molecular mechanism remains unclear. Furthermore, Ngb was found to have a role in tumor suppression, as overexpression of Ngb downregulated the Raf/MEK/Erk oncogenic cascade through interaction with c-Raf-1 (J. Zhang et al. 2013). In addition to inhibiting tumorigenesis, Ngb was proposed to have a function in the regulation of cell death, as it binds apoptosis regulators such as alpha subunit of the heterotrimeric G protein (Gα) and ferric cytochrome *c* (Cyt *c*) (Fago et al. 2006; Wakasugi, Nakano, and Morishima 2003).

1.4 Vertebrate globin structure

With the exception of Cygb, typical vertebrate globin consists of ~150 amino acids that form eight helices denoted A through H (Figure 1.2). The characteristic 3-over-3 globin fold forms a large hydrophobic cavity that binds a heme prosthetic group (Fe-protoporphyrin IX) through a coordination bond with a strictly conserved, proximal histidine residue in the 8^{th} position of the helix F (HisF8). The phenylalanine residue located in the loop connecting short C and D helices (PheCD1) is the only other amino acid that is strongly conserved across all globins and plays a key role in the stabilization of heme in the binding pocket (Hargrove et al. 1994; Honig et al. 1990). Solvent-accessible (propionate) and inaccessible (methyl, vinyl) side chains, along with the heme hydrophobic core interact with approximately 19 surrounding residues, thus securing the heme within the central cavity through an extensive network of noncovalent interactions.

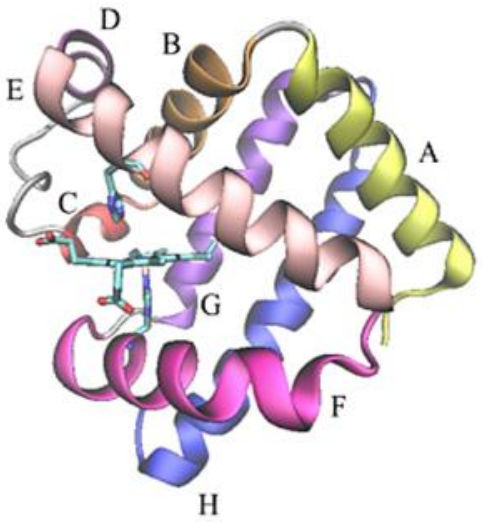

Figure 1.2. Three-dimensional structure of sperm whale Mb (swMb). Color coded helices A-H are shown as ribbons, whereas heme prosthetic group, proximal and distal histidines are shown in stick representation

1.5 Heme hexacoordination

Unexpectedly, Ngb and Cygb differ from vertebrate globins in several structural features. In Hb and Mb, the heme is linked to the protein matrix through a single coordination bond with HisF8, resulting in a pentacoordinate heme with a virtually unobstructed sixth ligation site. However, in Ngb and Cygb, the heme coordinates to an additional "distal" histidine residue (HisE7), yielding an internally hexacoordinated heme iron. Since sixth coordination site is occupied by HisE7, binding of an external ligand is rate-limited by dissociation of distal histidine. Although hexacoordination was previously observed in non-symbiotic plant, bacterial, and invertebrate globins (Kakar et al. 2010), the physiological role of this structural feature is not yet understood. Interestingly, phylogenetic analysis of the recently expanded globin superfamily revealed that hexacoordination is an ancestral feature (Figure 1.3) (Blank and Burmester 2012),

leading to a hypothesis that pentacoordination was an evolutionary response to an increased demand for a more efficient O_2 diffusion (Burmester and Hankeln 2014).

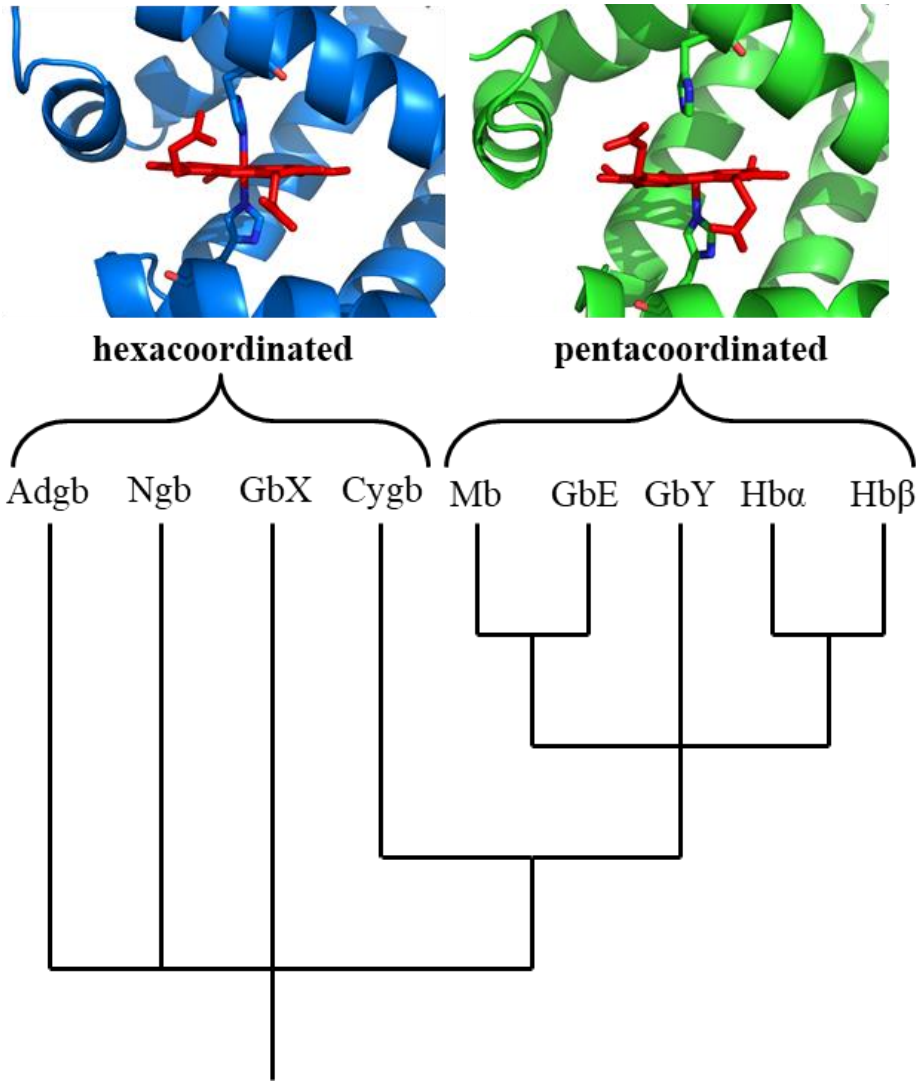

Figure 1.3. Simplified phylogenetic tree representing evolution of selected globins. Heme coordination of GbY has not yet been experimentally confirmed. The figure was adopted from Burmester and Hankeln. (Burmester and Hankeln 2014)

1.6 Disulfide bond and regulation of ligand binding

Furthermore, cysteine residues in Ngb (CysCD5, CysD5) and Cygb (CysB2, CysE9) are capable of forming intra- and inter-molecular disulfide bonds (Figure 1.4). Neuroglobin is assumed to be a monomer under physiological conditions (17 kDa),

although several groups have observed formation of a dimer as well (Hamdane et al. 2003; Lechauve et al. 2012; Ostojić et al. 2006). On the other hand, Cygb was reported to oligomerize by forming disulfide-linked dimers (Beckerson et al. 2015; Makino et al. 2006); however, it is probably a monomer at physiological concentration (Lechauve et al. 2010).

Formation of the disulfide bond induces conformational changes that regulate ligand interactions with hexacoordinate globins. For example, the disruption of the disulfide bridge lowers the heme affinity for oxygen by a factor of two and ten for Cygb and Ngb, respectively (Hamdane et al. 2003). In addition, presence of the disulfide bond enhances nitrite reductase activity in both Cygb and Ngb (Reeder and Ukeri 2018; Tiso et al. 2011). Lipid peroxidation by Cygb is also a disulfide-dependent function that occurs only in the presence of the disulfide bridge (Tejero et al. 2016).

Furthermore, disulfide bond regulates overall stability of Ngb and Cygb. While rupture of the disulfide bond was found to increase thermostability of Ngb (Hamdane et al. 2005), analogous impact was not observed in Cygb (Tangar, unpublished data). Interestingly, hexacoordinate globins are more thermostable than pentacoordinate, as melting temperatures of Cygb and Ngb are 14 and 22°C higher than measured for Mb (Hamdane et al. 2005).

Given the regulatory role of the disulfide bond, physiological functions of Cygb and Ngb were proposed to be modulated by the redox status of the cell (Hamdane et al. 2003).

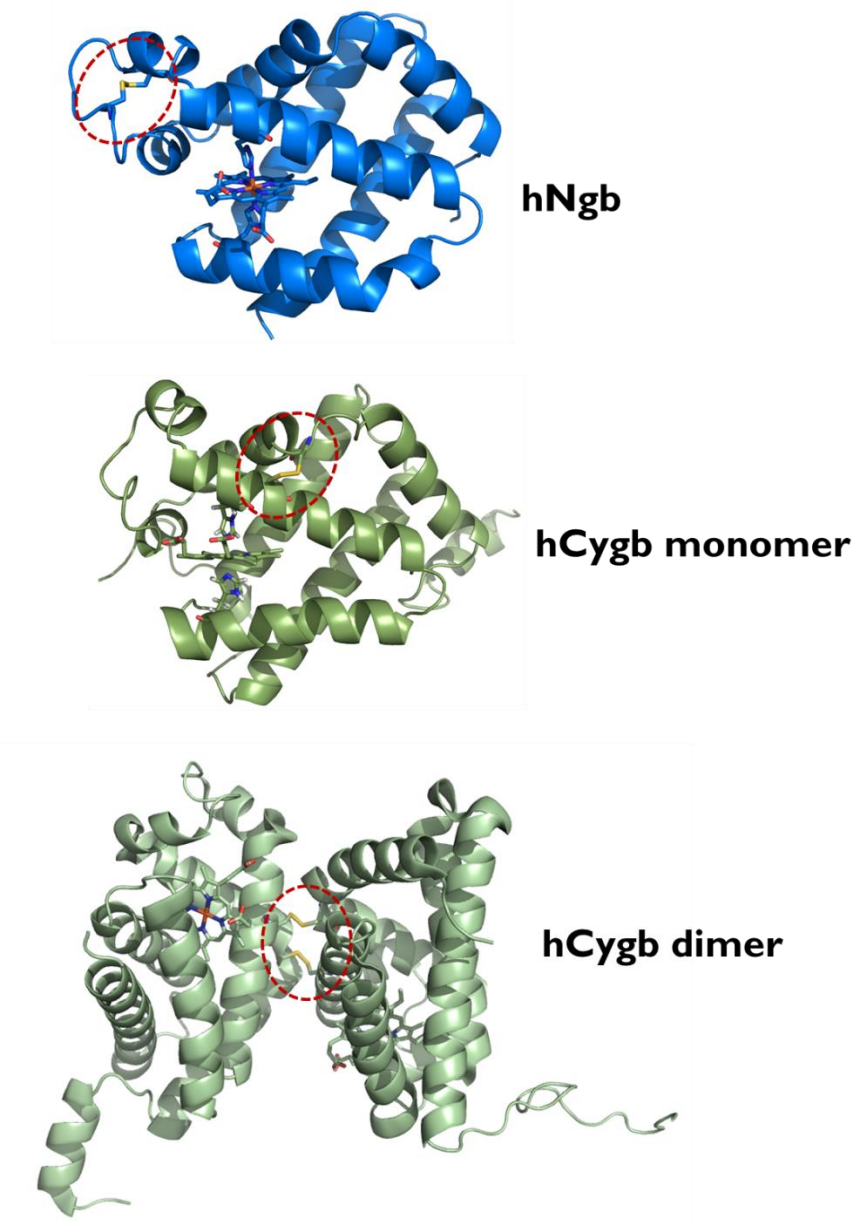

Figure 1.4. Dashed ellipse indicates the location of the disulfide bridge (yellow) in human Ngb (PDB: 4MPM; chain A), monomeric (full-length model based on PDB: 2DC3) and dimeric human Cygb (PDB: 2DC3). (Guimarães et al. 2014; Makino et al. 2006)

1.7 Terminal extensions

Unlike other vertebrate globins, Cygb has ~20 amino acid long terminal extensions on both N- and C- terminal that flank the globin core. Although there are 9

crystal structures of human Cygb deposited in the Protein Data Bank (PDB), the terminal fragments were partially resolved in only one structure, indicating a high degree of disorder (Makino et al. 2006). The N terminal extension forms a short helix and is overall negatively charged (-3), whereas the C terminus contains five proline residues and lacks a secondary structure (Makino et al. 2006). The physiological role of the terminal extensions is yet to be determined, although it was proposed that they may play a role in intracellular interactions (de Sanctis et al. 2004a).

1.8 Heme isomerism

The NMR and X-ray crystallographic studies revealed poor heme orientational selectivity in human and mouse Ngb scaffolds, where iron protoporphyrin IX (FePPIX) incorporates in two different conformations, rotated 180° with respect to the α-γ meso axis (Du et al. 2003; Guimarães et al. 2014). Heme orientational heterogeneity in Ngb is proposed to be structurally allowed by the unusually large cavity in the interior of the protein matrix, adjacent to the heme binding pocket (Vallone, Nienhaus, Brunori, et al. 2004). It is important to note that heme orientation affects ligand binding, as 5-fold difference in rate of cyanide association was observed for heme isomers in Ngb (Bocahut et al. 2013).

1.9 Globin interactions with diatomic ligands

Ligand association to heme is primarily dependent on the spin/oxidation state of the heme iron. In globins, Fe^{3+} binds water and anionic ligands such as CN^-, N_3^-, NO_2^-, F^-, whereas O_2 and CO bind to ferrous species only (Antonini and Brunori 1971). Nitric oxide, on the other hand, binds to both ferrous and ferric species (Traylor and Sharma

1992). Globins have a remarkable ability to discriminate between different diatomic ligands, despite their similarity in size. The advancement of the X-ray crystallography and site-directed mutagenesis techniques played a key role in elucidation of the physico-chemical properties that modulate ligand affinity for heme iron. Decades of research converge on three major determinants that regulate ligand affinity in globins (Capece et al. 2013): (1) accessibility of the heme binding site, (2) electrostatic interactions in the distal pocket, and (3) non-covalent interactions and orientation of the proximal histidine residue.

1.10 Accessibility of the binding site

In 1966, Perutz and Matthews proposed that the ligand access to heme iron is gated by the swinging motion of HisE7 sidechain (Perutz and Mathews 1966). Although crystallographic evidence for this hypothesis exists only for Mb at low pH, time-resolved spectroscopic studies provide evidence for the role of the HisE7 in the regulation of heme access, as substitution of distal histidine with bulkier residues (Tyr, Trp) reduced the rate of ligand association (Birukou, Schweers, and Olson 2010).

Time-resolved X-ray crystallography was also employed to map out the path of ligand migration following the photocleavage of iron-CO bond. The fate of the photodissociated CO molecule was found to be correlated with the locations of the internal cavities. Indeed, the typical globin fold is characterized by the presence of small hydrophobic pockets (30-100 $Å^3$) (Tilton, Kuntz, and Petsko 1984) that act as transient docking sites for ligand migration into and out of the heme binding site (M Brunori et al. 2000; Šrajer et al. 1996). The locations of these apolar pockets are determined by

exposing crystallized proteins to a xenon or krypton atmosphere prior to collection of the X-ray diffraction patterns. The size and connectivity of internal pockets are modulated by intrinsic protein dynamics, and vary across the globin superfamily, as seen in Figure 1.5 (de Sanctis et al. 2004b; Savino et al. 2009; Vallone, Nienhaus, Matthes, et al. 2004). Migration of the diatomic ligand through the globin matrix is often probed by computational techniques, which reveal multiple ligand entry/exit pathways (Bocahut et al. 2009; Cohen, Olsen, and Schulten 2008; Elbert and Karplus 1990; Orlowski and Nowak 2007; Pietra 2013).

Analysis of Xe binding sites in the newly discovered hexacoordinate globins revealed the formation of an unusually large cavity (240-330 $Å^3$) in the protein interior (de Sanctis et al. 2004b; Vallone, Nienhaus, Brunori, et al. 2004). The physiological function of this "packing defect" remains to be explored, however, molecular dynamics studies revealed that the shape and size of the cavity change as a function of the presence or absence of the disulfide bond (Bocahut et al. 2009). Furthermore, experimental data suggest that, in the presence of disulfide bond CO escapes by means of the distal His gate in Cygb (Astudillo et al. 2013), but not in Ngb (Astudillo et al. 2012; Bocahut et al. 2009).

It should be noted that polarity, but not the ligand size dictate the magnitude of barriers along the ligand migration pathway (Elbert and Karplus 1990). Schulten group computed energy barriers for the escape of CO, O_2 and NO from Mb, and observed higher energetic cost (3-5 kcal/mol) for CO transitions between the internal cavities and/or direct escape to the solvent than in the other two gases (Cohen et al. 2006).

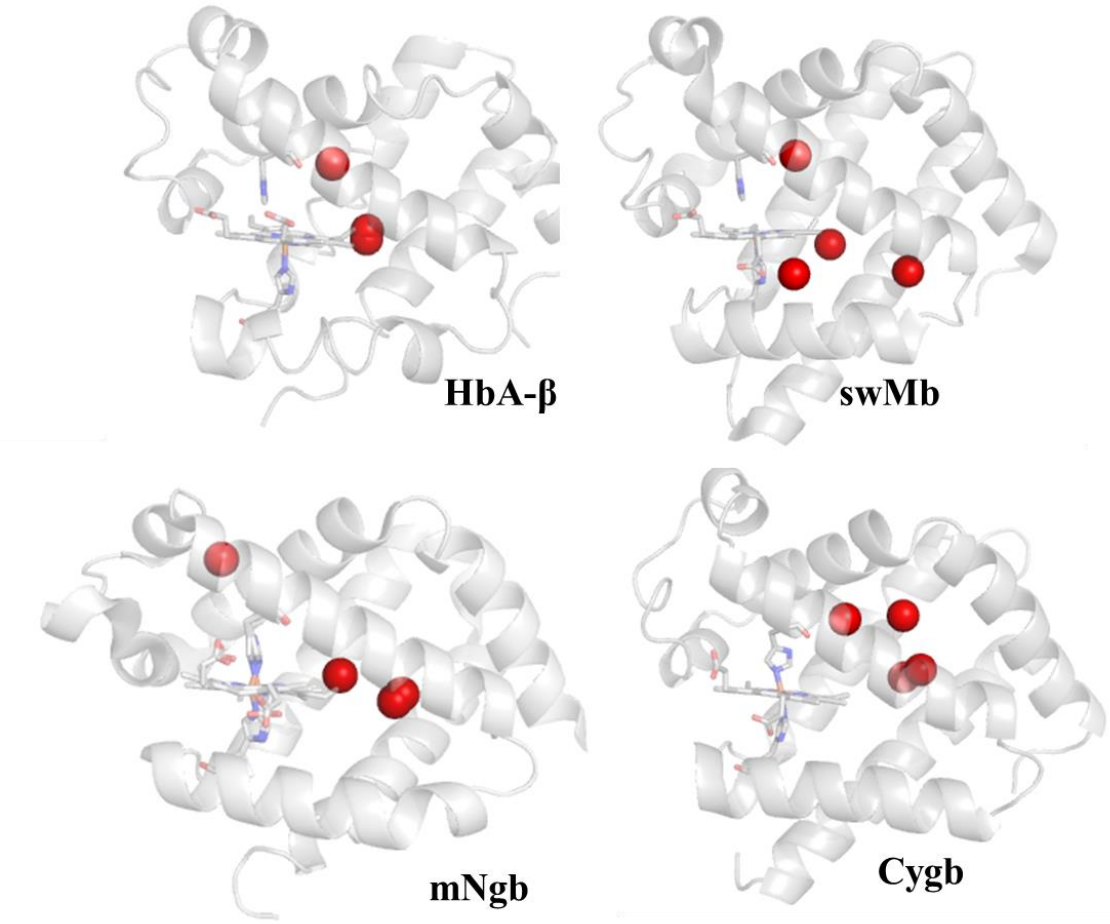

Figure 1.5. Distribution of xenon atoms (red spheres) occupying internal cavities in vertebrate globins. (Moschetti et al. 2009; de Sanctis et al. 2004b; Savino et al. 2009)

1.11 Distal histidine interaction with the bound ligand

In addition to acting as a gate, distal histidine aids in ligand discrimination by forming a strong hydrogen bond with iron-bound O_2, but not with CO and NO (Olson et al. 1988). Crystallographic data shown in Figure 1.6 illustrate the difference in orientation of HisE7 relative to the heme-bound ligand in sperm whale Mb. As indicated in Table 1.1, the geometry for HisE7-O_2 hydrogen bonding is more favorable than for HisE7-CO, resulting in enhanced stabilization of the bound state in the former case.

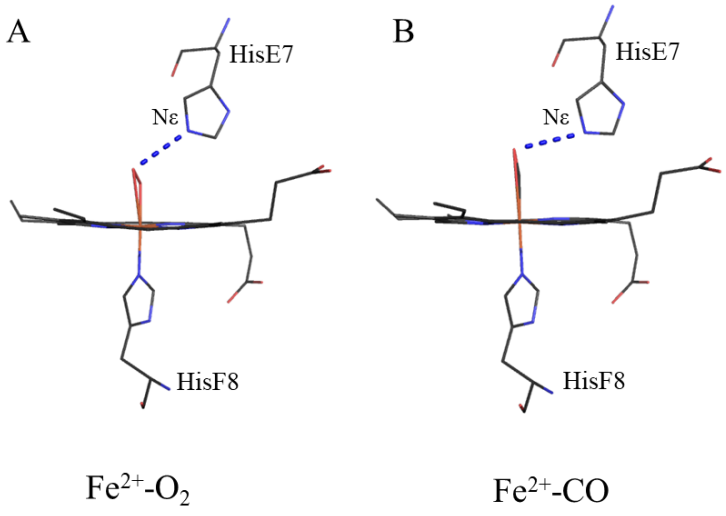

Figure 1.6. Oxygen- and CO-bound structures (PDB: 2VLY, 1DWR) of a horse heart Mb, showing the orientation of distal histidine sidechain with respect to the external ligand. Distance between hydrogen donor ($HisE7_{N\varepsilon}$) and hydrogen acceptor atoms is indicated with a dashed line.

		donor-acceptor distance (Å)	**donor-hydrogen-acceptor angle (°)**
pdb	**ligand**	**$HisE7_{N\varepsilon}$ - O**	**$HisE7_{N\varepsilon}$- $HisE7_{NH}$- O**
2VLY	O_2	2.91 (2.9)	16.1 (< 30)
1DWR	CO	3.07 (2.9)	55.3 (< 30)

Table 1.1. Comparison of hydrogen donor-acceptor distances and angles between distal histidine (HisE7) and heme ligands in horse heart myoglobin. Optimal values for N-H:::O donor-acceptor pair are showed in parentheses.

Ligand discrimination by distal His is also evident from kinetic studies on HisE7→Gly substituted Mb (Table 1.2). In the case of swMb, mutation of the distal histidine increases the rate of ligand dissociation by more than 100-fold for O_2, but only by a factor of 2 in the case of CO. In turn, substitution of HisE7 with Gly weakens the Fe-O_2 bond 13-fold, but strengthens the Fe-CO bond (Olson et al. 1988), providing clear evidence for distinct HisE7-mediated stabilization of heme-bound oxygen. An analogous effect was observed for the α and β subunits of HbA as well (Birukou, Schweers, and Olson 2010).

The substitution of HisE7 has lesser impact in hexacoordinate proteins than in pentacoordinate globins. Depending on the amino acid substitution (HisE7Val or HisE7Gln), the strength of the Fe-O_2 bond decreases only 2-4 times in Ngb-O_2, suggesting that the role of HisE7 in stabilization of heme-bound ligand is not as dominant as in Mb and Hb. These data are consistent with rates of autoxidation, which are three orders of magnitude faster in Ngb than in swMb, indicating a more labile Fe-O_2 bond in the hexacoordinate globin (Fago et al. 2004; Shikama 1998).

protein	ligand	k_{on} (μM^{-1} s^{-1})[a]	k_{off} (s^{-1})[a]	K_d (μM)
Mb-HisE7	O_2	14	12	0.86
Mb-HisE7Gly	O_2	140	1600	11.4
Mb-HisE7	CO	0.51	0.019	0.04
Mb-HisE7Gly	CO	5.8	0.038	0.007
Ngb-HisE7	O_2	140	0.8	0.006
Ngb-HisE7Gln	O_2	800	11	0.014

Table 1.2. Sperm whale Mb and Ngb values for rates of ligand association (k_{on}) and dissociation (k_{off}), as well as dissociation constant (K_d) (Hamdane et al. 2003; Olson et al. 1988),

1.12 Impact of proximal ligand on ligand affinity

The role of the proximal residue (HisF8) in modulation of ligand affinity was explored as well. Barrick crystallized the Mb HisF8Gly mutant with imidazole bound in the proximal site (Figure 1.7.) and found that, in the absence of a direct link to the protein moiety (1) imidazole rings rotates, and (2) the length of the imidazole-Fe bond decreases (Barrick 1994). The rotation of the imidazole ring from an eclipsed to a staggered conformation with respect to the pyrrole nitrogens was proposed to relieve steric strain, and in return contract the proximal bond (Figure 1.7.). Quantum mechanical calculations of O_2 binding energies relative to HisF8 sidechain orientation revealed that staggered

conformation and hydrogen bonding of N_{δ}- hydrogen yield the highest Fe-O_2 affinity (Capece et al. 2006). In addition, the HisF8-Fe bond was also found to be regulated by heme propionate interactions with surrounding residues. Specifically, Hayashi and coworkers reported that Mb reconstituted with heme lacking heme-7-propionate weakened the Fe-HisF8 bond, which increased rate of CO dissociation by a factor of ~3 (Hayashi et al. 2002). Therefore, the proximal histidine has a role in fine-tuning the ligand affinity.

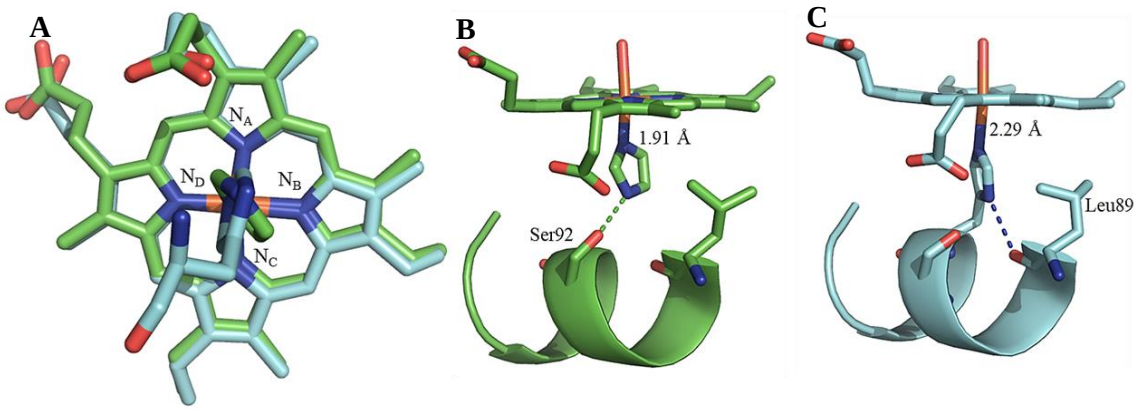

Figure 1.7. Impact of oxidation and ligation states of horse heart myoglobin on heme iron interaction with its coordination partners, as determined from crystallographic data. (A) Eclipsed (blue) and staggered (green) conformations or HisF8 and imidazole ligands, respectively. (B) Proximal site of imidazole- and (C) CO-bound Mb HisF8Gly. Putative noncovalent interactions between HisF8-N_{δ} hydrogen and adjacent amino-acids are shown as dashed lines.

1.13 Summary

Although it has been almost two decades since the discovery of Ngb and Cygb, the physiological roles of these proteins remain to be determined. It is well accepted that oxygen storage and/or transport functions are not likely for the new globins, due to their low intracellular concentration. Several *in vivo* studies have demonstrated potent cytoprotective properties of these two proteins, however, the underlying molecular

mechanisms that governs the Cygb- and Ngb-mediated prevention of cytotoxic damage are still poorly understood.

The presence of several structural features not observed in other vertebrate globins adds to the intrigue surrounding Ngb and Cygb function. Although heme hexacoordination was previously observed in bacteria and plants, the physiological impact is still not understood. In Ngb and Cygb, the strength of the HisE7-heme bond is regulated by the formation or disruption of the disulfide bond, and is inversely correlated to the gaseous ligand affinity for heme iron. The intercommunication between heme binding pocket and the disulfide link is remarkable and points toward redox-regulated function of the hexacoordinate globins.

This study is divided into several parts designed to answer the following questions: (1) Since Cygb and Ngb are not ligand storage/transport vessels, are they structurally predisposed to play a role in ligand sensing and signaling?; (2) How are structural changes following the rupture of the disulfide bond coupled to the distal histidine residue? (3) Do Cygb termini extensions impact protein stability, or gaseous ligand and lipid binding? Could termini segments provide a hydrophobic interface for protein-protein interactions?; (4) Can hexacoordinate globins like Ngb and Cygb incorporate fluorescent heme analogs?

2. OBJECTIVES

In the following chapters, experimental and computational approaches were combined to determine structure-function relationships in Cygb and Ngb with respect to their interactions with internal (distal histidine) and external ligands.

In chapter 4, femtosecond transient absorption spectroscopy was employed for the first time to characterize ultrafast kinetics following the photodissociation of the iron-CO bond in Ngb and Cygb. The aim of this project was to compare the reactivity of the heme iron in the hexacoordinate globins to pentacoordinate ones, as well as to determine the impact of the distal histidine and the intramolecular disulfide bond on ligand rebinding on subnanosecond timescales.

In chapter 5, the photophysical properties of Ngb and Cygb reconstituted with zinc protoporphyrin IX, a fluorescent analog of the native heme, were characterized. The goal of this project was to provide a tool for future biophysical characterizations of protein-protein interactions, as complexes between hexacoordinate globins and their intracellular partners remain largely unexplored.

In chapter 6, Cygb constructs lacking one or both termini extensions were characterized *in vitro*. Specifically, the impact of terminal extensions on secondary structure and stability of human Cygb were determined. Furthermore, the role of terminal extensions on regulation of diatomic ligand and lipid binding was characterized. To establish if terminal segments provide a hydrophobic site for potential intracellular interactions, 1,8-ANS binding of Cygb constructs was characterized experimentally and computationally.

In chapter 7, molecular dynamics simulations of hexa- and pentacoordinate human Ngb were performed to elucidate the role of the intraprotein disulfide bond and Tyr44 sidechain on reorganization of residues in the distal pocket and regulation of ligand accessibility to the distal pocket. The computational data were correlated with kinetic studies to elucidate how structural information between CD loop is transmitted to the heme binding pocket.

3. METHODS

3.1 Introduction

Chromophoric characters of heme prosthetic group, peptide bonds and aromatic residues serve as optical probes that were monitored by a wide variety of spectroscopic techniques to obtain information about protein structure, stability and mechanisms of protein-ligand interactions. In addition to steady-state characterizations, the photodissociable character of the iron-CO bond was exploited by time-resolved methods to determine the kinetic and thermodynamic profiles associated with CO interactions with hexacoordinate globins. Experimental studies were complemented by molecular dynamics simulations to elucidate protein dynamics and major conformations associated with different redox states of hexacoordinate globins. The techniques used in the study are summarized here.

3.2. Experimental Techniques

3.2.1 Protein Expression and Purification

Transformed cells for all proteins studied in this thesis were kindly provided by Sophie Bernad, Valerie Derrien and Pierre Sebban. Cloning and expression were prepared as reported before (Astudillo et al. 2013). Briefly, cDNA sequence coding for human Cygb constructs were cloned into pET15b vector. DNA sequence was confirmed with a sequencing method prior to transformation of the plasmid into competent *E. coli* BL21 cells. Previous expression protocol for Cygb (Astudillo et al., 2013) was optimized to produce higher yield of recombinant holoprotein. A single colony of *E. coli* containing a plasmid of a Cygb construct was transferred to a 50 mL of sterile Terrific Broth (TB) in

the presence of 100 mg/L of ampicillin. The culture was placed in a shaker for 6-8 hours at 175 rpm at 37°C. Ampicilin (100 mg/L), L-aminolevulinic acid (170mg/L) and 10 mL of cell culture were transferred into four Pyrex shaker flasks containing 250 mL of sterile TB (1 L total). The flasks were placed in a shaker (200 rpm, 37°C) until absorbance at 600 nm reached 0.9- 1.1. Protein expression was then induced by addition of isopropyl β-D-1-thiogalactopyranoside (IPTG) to a final concentration of 0.4 mM. The cells were grown overnight in a shaker (175 rpm, 30°C) and were collected after 16-24 hours. Culture was centrifuged at 5000 rpm for 15 minutes and stored at -20°C. Typical yield of 1 L prep was about 9 grams of cells.

Protein purification was initiated by homogenizing thawed cells in lysis buffer (50 mM Tris HCl, 5 mM dithiothreitol, pH 8.0). The mixture was placed on ice and sonicated in three-minute intervals for a total of 55 minutes. Cell lysate was centrifuged for 90 minutes at 5000 rpm, while Ni-NTA Superflow resin (Qiagen) was equilibrated with 10 volumes of 10 mM Tris HCl pH 8.0. Cell lysate was loaded onto the column and washed with equilibration buffer until $A_{280} < 0.3$. Buffers containing 10 mM TrisHCl pH 8.0 and increasing concentrations of imidazole were used to elute the recombinant proteins. Reinheitszahl (Rz) factor was used to combine proteins with similar A_{Soret}/A_{280} ratio above 2.4. Resulting fractions were concentrated using Amicon Millipore tubes with 10 kDa cutoff and dialyzed against 50 mM TrisHCl pH 7.0. Protein purity was checked using SDS-PAGE, and proteins were stored at -30°C in 200 µL aliquots. The detailed procedure for SDS-PAGE protocol suitable for Cygb protein preparations were described in detail before (Astudillo 2014).

3.2.2. UV-vis Absorption Spectroscopy

Absorption spectroscopy applications on biomolecules rely on Beer-Lambert law (Eq. 3.1), which states that the absorbance of a molecule depends on cell path (l), extinction coefficient (ε) and concentration of the absorbing species (c).

$$A = \varepsilon l c \qquad \text{Eq. 3.1}$$

All proteins absorb strongly in the 180-240 nm region, which is associated with n-π* and π-π* transitions of the peptide bond (Holde, Johnson, and Ho 1998; Rosenheck and Doty 1961). The dependence of the spectral shape on secondary structure of a peptide was probed by modulating pH and temperature to achieve conformational transitions in poly-L-lysine (Rosenheck and Doty 1961). It was found that random coil and β-sheet conformations are characterized by absorption maxima at 192 nm (ε_{192} = 7.1 mM^{-1} cm^{-1}) and 194 nm, respectively. Formation of poly-L-lysine α-helix induced a bathochromic shift of the absorption maximum to 205 nm (ε_{205} = 4.4 mM^{-1} cm^{-1}), with a shoulder at 215 nm (Rosenheck and Doty 1961). Although absorption data can reveal information about α-helical or β-sheet content, UV-vis spectra are rarely used to characterize changes in secondary structure of proteins.

In addition to the peptide bond, electronic π-π* transitions of aromatic sidechains of tryptophan (ε_{280} = 5.5 mM^{-1} cm^{-1}), tyrosine (ε_{280} = 1.49 mM^{-1} cm^{-1}), and phenylalanine (ε_{280} = 0.2 mM^{-1} cm^{-1}) exhibit absorbance between 260-280 nm (Mach, Middaugh, and Lewis 1992). Furthermore, hemoproteins have a unique spectral signature across near-UV and visible regions as a result of an extended electron delocalization of the heme prosthetic group. The maximum intensity peak of a hemoprotein is conventionally

denoted as the Soret band and absorbs in the 400-430 nm with ε_{Soret} > 100 mM^{-1} cm^{-1} (Weissbluth 1974). In addition, lower intensity peaks observed in the 500-600 nm region are denoted as Q bands with $\varepsilon_Q \sim$ 10-15 mM^{-1} cm^{-1} (Weissbluth 1974). The presence of the heme chromophore provides an invaluable advantage in protein characterization as changes in spectral features of hemoprotein are indicative of changes in heme iron spins and reflect subtle conformational changes in the heme microenvironment.

3.2.3. Circular Dichroism

Circular dichroism (CD) spectroscopy is a valuable tool in structural biology as it provides information about secondary structure of biomolecules. In CD spectroscopy, the difference in absorbance of left (A_L) and right (A_R) circularly polarized light of the sample (Eq. 3.2) is measured by a spectropolarimeter.

$$\Delta A = A_L - A_R \qquad \text{Eq. 3.2}$$

The signal is collected as a function of wavelength in terms of ellipticity (θ, Eq. 3.3) and is observed only when the chromophore is chiral (Kelly, Jess, and Price 2005).

$$\theta = 32.98\ \Delta A \qquad \text{Eq. 3.3}$$

In proteins, the peptide bonds absorb circularly polarized light in the 190-250 nm region and are extremely sensitive to the secondary structure of the polypeptide (Figure 3.1). For example, CD spectrum of an α-helical polypeptide chain is characterized by negative signals at 222 and 208 nm, and a positive signal at 190 nm (Holde, Johnson, and Ho 1998). In contrast, β-sheet exhibits spectrum minima and maxima at 215 and 198 nm, respectively (Holde, Johnson, and Ho 1998). Lastly, CD spectrum of a random coil is

characterized by a negative peak at about 195 nm (Holde, Johnson, and Ho 1998). Proteins consisting of all three motifs will exhibit a CD signal that is a combination of the three signature spectra. There are many algorithms and software currently available that predict secondary structural composition of a protein using their CD signals. However, the accuracy of these programs is under debate and such calculations/predictions should be taken into account with caution.

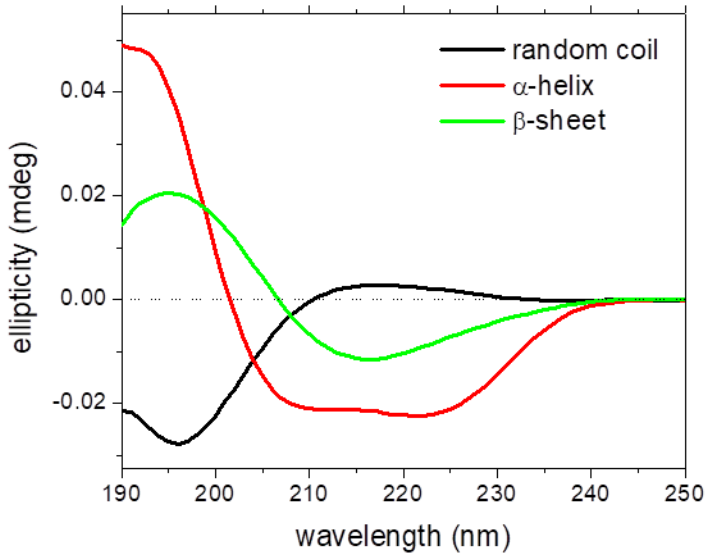

Figure 3.1. Sample electronic CD spectra of a peptide bond in α-helix, a β-sheet and a random coil, as simulated by Abriata algorithm (Abriata 2011).

Circular dichroism spectroscopy can be applied to observe changes in secondary structure upon ligand binding, sequence deletion or residue mutation. Furthermore, a spectropolarimeter equipped with a temperature-controlled cell holder can be employed to perform thermal denaturation of biomolecules in order to determine the enthalpy of

melting (ΔH_m) and melting temperature (T_m). Data analysis for the CD-monitored protein melting experiments was published before (Greenfield 2006).

3.2.4. Transient Absorption Spectroscopy

3.2.4.1. Introduction

Kinetics of ligand association and dissociation from a protein obtained by time-resolved techniques can be used to construct kinetic models and provide insight into the protein-ligand interaction mechanism. Stopped-flow was the first time-resolved absorption-coupled technique used to observe formation of hemoglobin and oxygen complex (Hartridge and Roughton 1923). The method is based on rapid mixing of the ligand and receptor while complex formation is monitored as a change in absorbance at a single-wavelength. The major drawback of stopped-flow was, and still is, the instrumental dead time in the millisecond range, which prevents determination of kinetics for reactions that occur on faster timescales (refer to Figure 3.11).

Transient absorption spectroscopy (TA), or flash photolysis, is a pump-probe method that monitors changes in absorbance of a photo-induced chemical reaction. In a seminal work by Gibson in 1956, the flash photolysis method was used for the first time to observe recombination of CO to myoglobin following the photo-cleavage of the iron-CO bond (Gibson 1956). Gibson used a photographic flash (0.5 ms duration) to initiate the photodissociation reaction and observed rates of CO association that were analogous to the values obtained by stopped-flow, thus validating the new technique (Gibson 1956). However, in contrast to stopped-flow, the advantage of Gibson's apparatus was that the temporal resolution of the instrumentation components could be improved.

Advancements in photonics led to replacement of photographic flash tubes with lasers, and TA can now be used to probe events on femtosecond to millisecond timescales.

Although all ferrous heme ligands (CO, O_2 and NO) are photodissociable (Gibson and Ainsworth 1957), studies of carbon monoxide recombination with hemoproteins are the most abundant to date. This is primarily because of high quantum yield for bimolecular rebinding (Φ_{ph}) and moderate recombination kinetics. The transient absorption technique has proved to be an invaluable tool in hemoprotein research, and has been utilized to probe how single residue mutations and heme modifications impact ligand migration and protein dynamics in hemoproteins. Representative steady-state spectra of deoxy- and CO-bound globins are shown in Figure 3.2, along with sample trace obtained using TA spectroscopy.

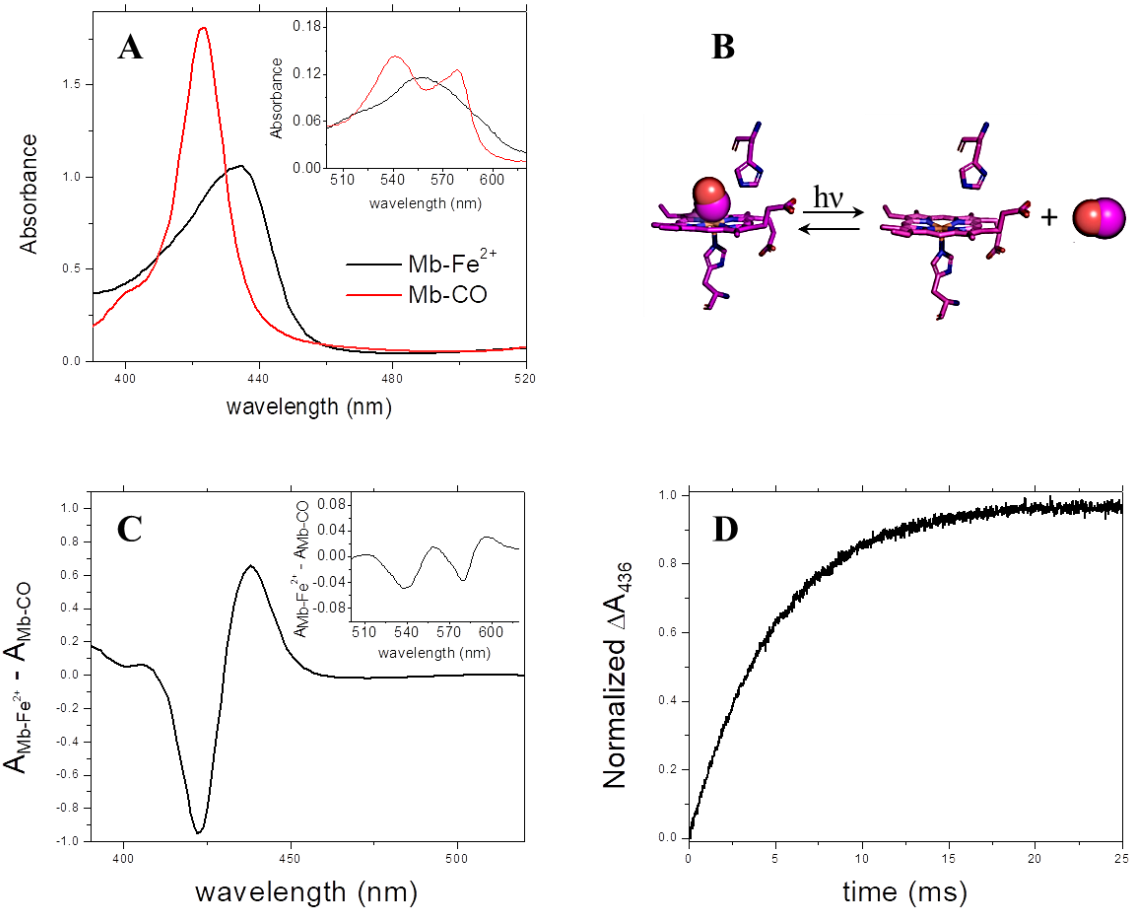

Figure 3.2. Transient absorption measures change in absorbance between ligand-bound and ligand-free forms, as ligand rebinds to the deoxy state of the heme. (A) Absorbance of deoxy- and CO-Mb in the UV and visible (inset) region. (B) Simplified reaction schematic of CO photodissociation and recombination to Mb. (C) Steady-state difference spectra. (D) Kinetics of CO recombination to myoglobin on microsecond to millisecond timescale.

3.2.4.2. Instrumental setup

3.2.4.2.1. Millisecond-to-microsecond transient absorption spectroscopy

The home-built transient absorption apparatus in Dr. Miksovska's research lab is illustrated in Figure 3.3. The samples were prepared in a 0.2 x 1 cm quartz cuvette and transferred into a temperature-controlled cuvette holder (Quantum Northwest).

Photoexcitation was achieved using a frequency-doubled, Q-switched Nd:YAG (7 ns, 1 Hz, Surelite I-10, Continuum) with 532 nm output. The pump beam was directed onto the center of the cuvette with the use of mirrors. Perpendicular to the pump was output from the continuous probe beam (200 W Xe arc lamp, Newport), which was focused on the center of the cuvette and monochromator (Jobin Yvon) using lenses (Newport). Single wavelength kinetics were detected by a photodiode (model 818-BB-22, Newport). The signal was amplified (C6438-01, Hamamatsu) and visualized by 400 MHz oscilloscope (Wave Surfer 42 Xs, LeCroy). Data acquisition was triggered by a laser Q switch.

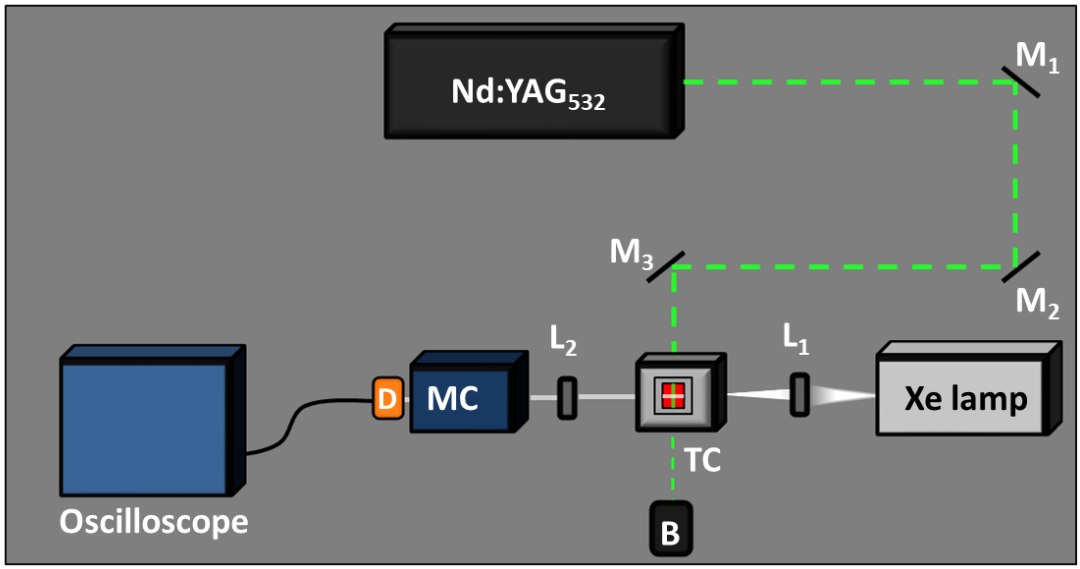

Figure 3.3. Top-view schematic of the transient absorption apparatus. TA components: the sample (red), temperature-controlled cuvette holder (TC), mirrors (M_1, M_2, M_3), pump beam ($Nd:YAG_{532}$), beam blocker (B), lenses (L_1, L_2), probe beam (Xe lamp), monochromator (MC), photodiode (D) and oscilloscope. Dashed line indicates pulsed light.

3.2.4.2.2. Ultrafast transient absorption spectroscopy

Ultrafast or femtosecond transient absorption (fsTA) experiments were carried out in the research lab of Dr. Amy M. Scott at the University of Miami. The fsTA measurements were performed with an instrument that used a commercial Ti:sapphire oscillator (MaiTai, Spectra Physics) and a mode-locked Ti:sapphire regenerative amplifier (Spitfire Ace, Spectra Physics) pumped by a 527 nm Nd:YLE laser (Empower, Spectra Physics). The power of the amplified pulse output was 5 W, with time duration of 35 fs (FWHM), which was centered at 800 nm at a repetition rate of 1 kHz. The output of the ultrafast laser system was divided into two beams for the pump and the probe. A 400 nm pump beam was generated from the 800 nm fundamental using a SHG crystal, with an instrument response time of ~70 fs (FWHM). The white light probe was generated from the split 800 nm beam by focusing either on a sapphire (440 nm– 800 nm) or CaF_2 (320 nm – 700 nm) window. The pump and probe beams were sent to a commercial FsTA setup (Helios, Ultrafast Systems) in which the probe was delayed relative to the pump using a mechanical delay track. The complementary metal-oxide semiconductor image sensor allows for construction of two dimensional plots of intensity as a function of time and wavelength, as shown in Figure 3.4.

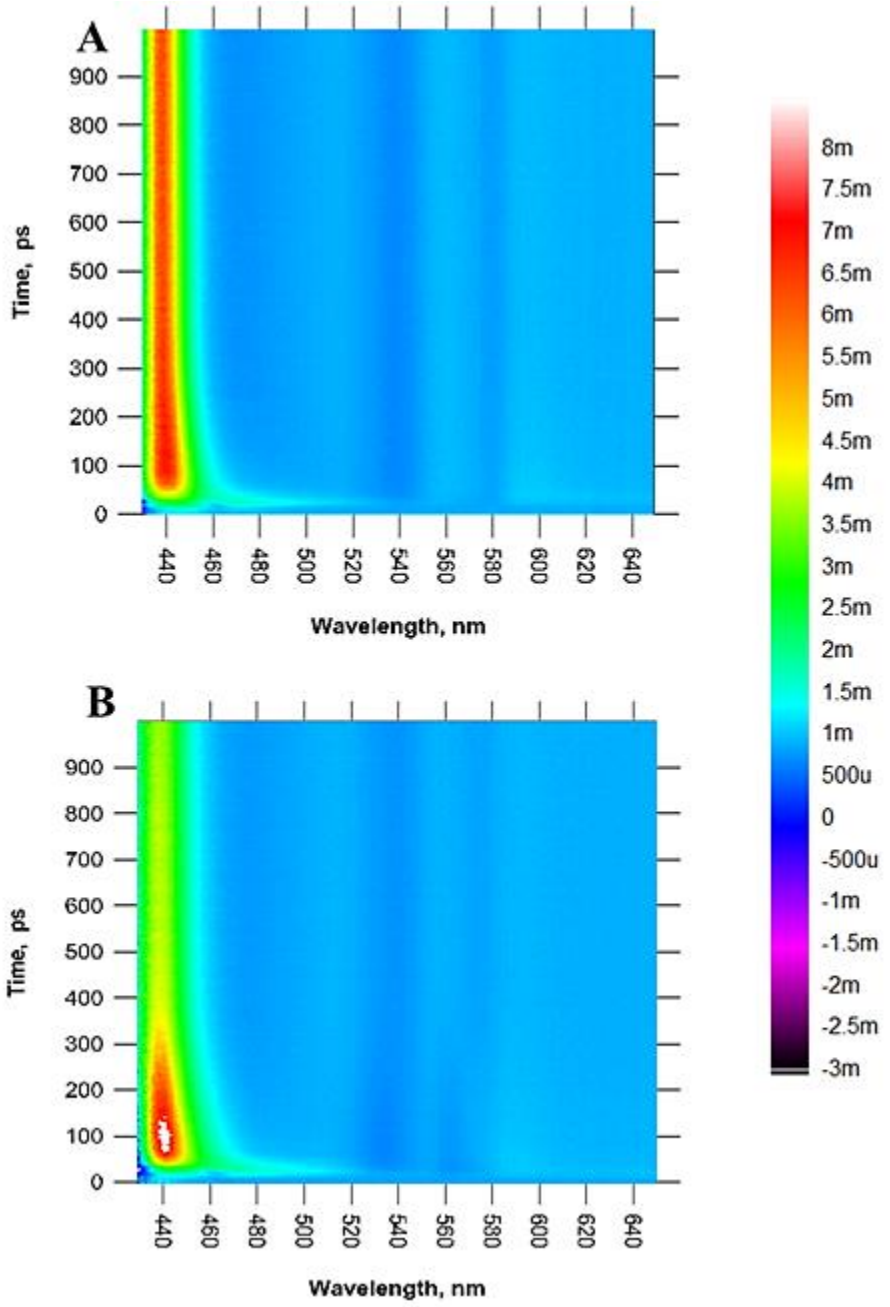

Figure 3.4. Two-dimensional surface representing time course of photodissociatied MbCO (A) and CygbWT-CO (B) complex, as a function of wavelength, measured by ultra-fast transient absorption. The legend indicates positive and negative changes in absorbance, where m represents milli-OD. Sharp positive signal at ~440 nm and negative signals at ~540 nm and ~570 nm are correlated to the steady-state difference spectra shown in Figure 3.2.C.

3.2.4.3. Data Analysis

Pseudo-first order reactions

Recombination experiments were performed in conditions of excess ligand concentrations, which generate pseudo-first order kinetics. For ligand binding to pentacoordinate proteins such as Mb, a reaction describing formation of Mb:CO complex can be written as

$$Mb + CO \xrightarrow{k_{CO}} Mb{:}CO \qquad \text{Eq 3.4}$$

where k_{CO} represents rate of ligand association. At a reaction time t, concentrations of reactants $[Mb]_t$ and $[CO]_t$ can be written in terms of their initial concentrations $[Mb]_0$ and $[CO]_0$, such that $[Mb]_t = [Mb]_0 - x$ and $[CO]_t = [CO]_0 - x$. Therefore, the rates of reaction can be defined as Eq 3.5:

$$\frac{dx}{dt} = k_{CO}\,([Mb]_0 - x)([CO]_0 - x) \qquad \text{Eq 3.5}$$

Rearrangement and integration of Equation 3.5 gives a logarithmic expression between the rate of association and reactant concentrations (Eq 3.8):

$$\frac{dx}{([Mb]_0 - x)([CO]_0 - x)} = k_{CO}\,dt \qquad \text{Eq 3.6}$$

$$\int_0^x \frac{1}{[Mb]_0 - [CO]_0}\left(\frac{1}{[Mb]_0 - x} - \frac{1}{[CO]_0 - x}\right) dx = k_{CO}\int_0^t dt \qquad \text{Eq 3.7}$$

$$\frac{1}{[Mb]_0 - [CO]_0} \ln \frac{[CO]_0[Mb]_t}{[Mb]_0[CO]_t} = k_{CO}t \qquad \text{Eq 3.8}$$

However, since $[Mb]_0 \ll [CO]_0$, it is reasonable to approximate that $[CO]_0 \approx [CO]_t$, and Eq 3.8 is then reduced to

$$[Mb]_t = [Mb]_0 e^{-k_{CO}[CO]_0 t} \quad \text{Eq 3.9}$$

Therefore, the observed rate constant corresponds to $k_{obs} = k_{CO}[CO]$.

However, in the case of hexacoordinate hemoproteins, reversible coordination of distal histidine introduces additional kinetic step, and Eq 3.4. is therefore modified to:

$$H \underset{k_H}{\overset{k_{-H}}{\rightleftharpoons}} P \xrightarrow{k_{CO}[CO]} P{:}CO \quad \text{Eq 3.10}$$

where H represents hexacoordinate species, k_{-H} and k_H rates of histidine dissociation and association, and $k_{CO}[CO]$ is the rate of pseudo-first order kinetics of CO association. Capellos and Bielski classify this reaction scheme as "parallel reversible and irreversible reactions of first-order" (Capellos and Bielski 1972) and solve it using Laplace transforms. First, decomposition rates of P, H and P:CO are defined as

$$\frac{d[P]}{dt} = k_{-H}[H] - [P](k_H + k_{co}[CO]) \quad \text{Eq 3.11}$$

$$\frac{d[H]}{dt} = k_H[P] - k_{-H}[H] \quad \text{Eq 3.12}$$

$$\frac{d[P{:}CO]}{dt} = k_{CO}[CO][P] \quad \text{Eq 3.13}$$

For reaction kinetics observed by TA, we can assume that at t= 0, [P]= $[P]_0$, therefore operator $\frac{dx}{dt} = Sx - Sx_0$ is used. However, because at time-zero $[H]_0$= $[P{:}CO]_0$= 0, the proper operator is $\frac{d}{dt} = S$. Therefore, the rate expressions can then be rewritten as:

$$S[P] - S[P]_0 = k_{-H}[H] - [P](k_H + k_{CO}[CO]) \quad \text{Eq 3.14}$$

$$S[H] = k_H[P] - k_{-H}[H] \quad \text{Eq 3.15}$$

$$S[P{:}CO] = k_{CO}[CO][P] \quad \text{Eq 3.16}$$

Substituting the expression for [H] in [P] yields:

$$[H] = \frac{k_H[P]}{S+k_{-H}} \quad \text{Eq 3.17}$$

$$[P] = \frac{S[P]_0(S+k_{-H})}{S^2+S(k_H+k_{-H}+k_{CO}[CO])+ k_{-H}k_{CO}[CO]} \quad \text{Eq 3.18}$$

If the quadratic equation (denominator, Eq 3.18) is rewritten as shown in Eq. 3.20, then solution to the equation γ_1 and γ_2 can also be determined:

$$S^2 + S(k_H + k_{-H} + k_{CO}[CO]) + k_{-H}k_{CO}[CO] = 0 \quad \text{Eq 3.19}$$

$$(S + \gamma_1)(S + \gamma_2) = 0 \quad \text{Eq 3.20}$$

$$\gamma_{1,2} = \frac{(k_H - k_{-H} + k_{CO}[CO]) \pm \sqrt{(k_H - k_{-H} + k_{CO}[CO])^2 - 4k_{-H}k_{CO}[CO]}}{2} \quad \text{Eq 3.21}$$

Equations for [P], [H] and [P:CO] (Eq 3.22-24),

$$[P] = \frac{S[P]_0(S+k_{-H})}{(S+\gamma_1)(S+\gamma_2)} \quad \text{Eq 3.22}$$

$$[H] = \frac{k_H S[P]_0}{(S+\gamma_1)(S+\gamma_2)} \quad \text{Eq 3.23}$$

$$[P{:}CO] = \frac{k_{CO}[CO][P]_0(S+k_{-H})}{(S+\gamma_1)(S+\gamma_2)} \quad \text{Eq 3.24}$$

are solved using Laplace transforms (Eq 3.25-27):

$$\frac{S\,(S+b)}{(S+a_1)(S+a_2)} = \frac{b-a_1}{a_2-a_1}e^{-a_1 t} + \frac{b-a_2}{a_1-a_2}e^{-a_2 t} \quad \text{Eq 3.25}$$

$$\frac{S}{(S+a_1)(S+a_2)} = \frac{1}{a_2-a_1}e^{-a_1 t} - \frac{1}{a_1-a_2}e^{-a_2 t} \quad \text{Eq 3.26}$$

$$\frac{S+b}{(S+a_1)(S+a_2)} = \frac{b}{a_1 a_2} - \frac{b-a_1}{a_1(a_2-a_1)}e^{-a_1 t} - \frac{b-a_2}{a_2(a_1-a_2)}e^{-a_2 t} \quad \text{Eq 3.27}$$

Finally, the solutions to [P], [H] and [P:CO] are as follows:

$$[P] = [P]_0\left[\frac{k_{-H}-\gamma_1}{\gamma_2-\gamma_1}e^{-\gamma_1 t} + \frac{k_{-H}-\gamma_2}{\gamma_1-\gamma_2}e^{-\gamma_2 t}\right] \quad \text{Eq 3.28}$$

$$[H] = \frac{k_H[P]_0}{\gamma_2-\gamma_1}\left[\frac{e^{-\gamma_1 t}}{\gamma_2-\gamma_1} + \frac{e^{-\gamma_2 t}}{\gamma_1-\gamma_2}\right] \quad \text{Eq 3.29}$$

$$[P{:}CO] = [P]_0\left[\frac{k_{-H}k_{CO}[CO]}{\gamma_1\gamma_2} - \frac{k_{CO}[CO](k_{-H}-\gamma_1)}{\gamma_1(\gamma_2-\gamma_1)}e^{-\gamma_1 t} - \frac{k_{CO}[CO](k_{-H}-\gamma_2)}{\gamma_2(\gamma_1-\gamma_2)}e^{-\gamma_2 t}\right]$$

Eq 3.30

Hargrove applied solutions to these equations to analyze two-exponential decay observed for CO recombination to hexacoordinate rice hemoglobin (rHb1) (Hargrove 2000). In order to extract the k_{CO}, k_H and k_{-H}, $\gamma_1+\gamma_2$ and $\gamma_1\gamma_2$ were plotted as a function of CO concentration, as shown in equations 3.31-32 (Hargrove 2000). The validity of extracted microscopic rates was demonstrated by elucidation of CO rebinding rate in rHb1 distal histidine mutant.

$$\gamma_1 + \gamma_2 = k_{-H} + k_H + k_{CO}[CO] \quad \text{Eq 3.31}$$

$$\gamma_1\gamma_2 = k_{-H}k_{CO}[CO] \quad \text{Eq 3.32}$$

Steady-state thermodynamics

Time-resolved experiments performed as a function of temperature can be analyzed using Arrhenius (Eq 3.35) and Eyring (Eq 3.36) equations to obtain thermodynamic parameters associated with the reaction observed. Using the Arrhenius equation, activation energy (E_a) and pre-exponential factor (A) are obtained from the slope ($-E_a/R$) and y-intercept (ln A).

$$\ln k = \ln A - \frac{E_a}{RT} \quad \text{Eq 3.33}$$

On the other hand, the Eyring equation provides activation parameters associated with a chemical reaction:

$$\ln \frac{k}{T} = -\frac{\Delta^{\ddagger}H}{R} \cdot \frac{1}{T} + \ln \frac{k_B}{h} + \frac{\Delta^{\ddagger}S}{R} \quad \text{Eq 3.34}$$

It should be noted that E_a and $\Delta^{\ddagger}H$ are related quantities (Figure 3.4), and for reactions in solution, $E_a = \Delta^{\ddagger}H + RT$ (Atkins and de Paula 2006).

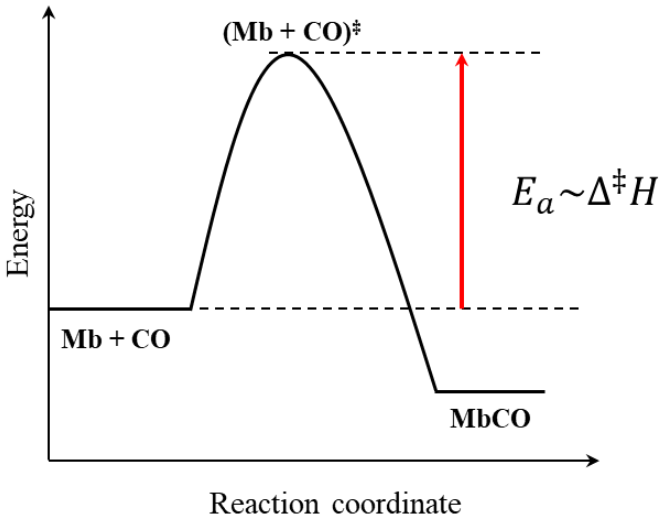

Figure 3.4. An illustration of reaction coordinate for processes observed with TA experiments.

3.2.5. Fluorescence Spectroscopy

Photon absorption excites a molecule from its ground state (S_0) to any vibrational level of a higher energy state (S_1 or S_2). Subsequently, the molecule relaxes rapidly to the lowest vibrational level of the first excited state (S_1), which occurs through a non-radiative process called internal conversion. After reaching the lowest vibrational level of S_1, the molecule can return to the ground state through non-radiative (heat release) or radiative (fluorescence or phosphorescence) processes. The transition pathways between ground and excited electronic states are often depicted by a Jablonski diagram (Figure 3.5). It should be noted that the energy of the absorbed photon is always larger than the energy of the emitted photon, as a portion of the absorbed energy is released or transferred as a result of internal conversion, solvent effects and energy transfer (Holde, Johnson, and Ho 1998; Lakowicz 2006). Therefore, fluorescence and phosphorescence

spectra are always shifted to the longer wavelengths relative to the absorption/excitation spectra.

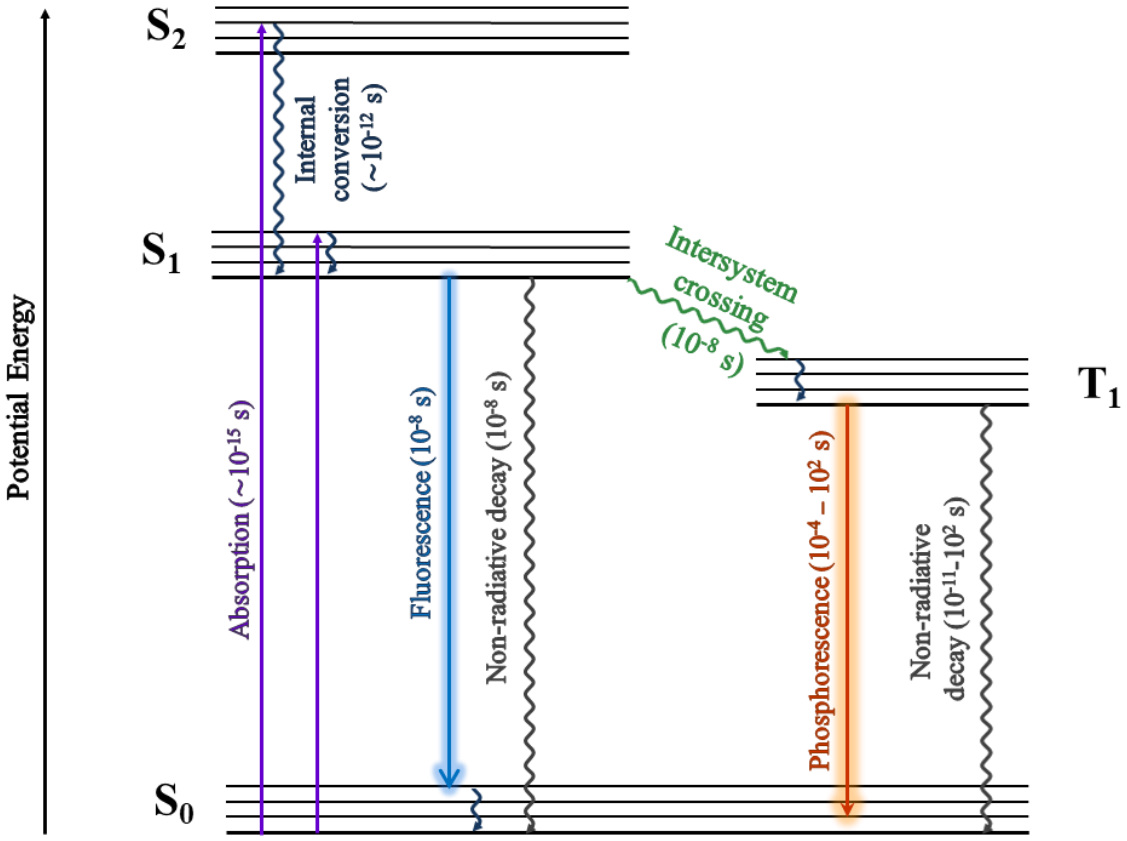

Figure 3.5. Simplified Jablonski diagram illustrates electronic transitions between different electronic states, including their lifetimes (shown in parentheses). Nonradiative and radiative processes are conventionally shown in wavy and straight lines, respectively.

Fluorescence is defined as a molecular transition from the lowest vibrational level of S_1 to any vibrational level of S_0 accompanied by a photon emission. Molecules capable of fluorescence are called fluorophores and are characterized in terms of their emission spectra maxima (λ_{max}), lifetime of the $S_1 \rightarrow S_0$ transition (τ_f) and fluorescence quantum yield (Φ_F). Fluorescence spectroscopy is a useful tool in protein science, as it offers qualitative and quantitative insight of a fluorophore or a fluorophore-bound complex.

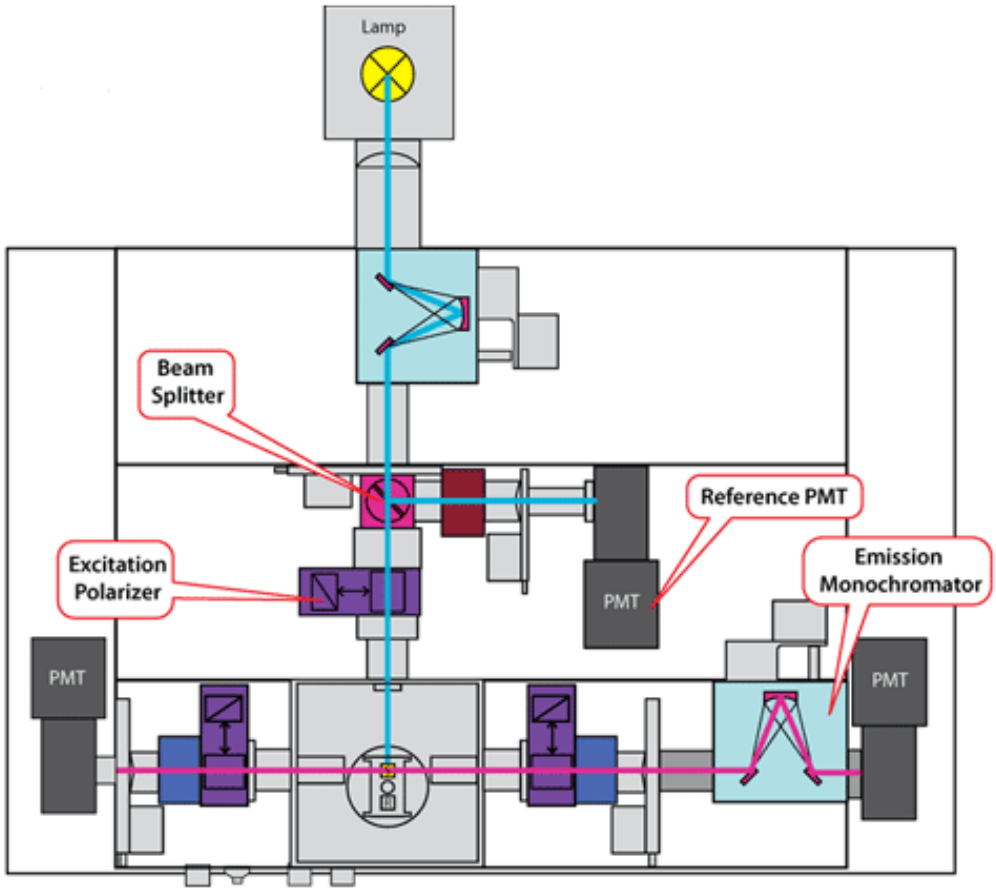

Figure 3.6. Schematic of the PC1 spectrofluorimeter (ISS, Champaign, IL) used for fluorescence-based characterizations in this work. ("ISS. Technical Diagrams. Schematic Diagram for PC1." n.d.)

3.2.5.1. Steady-state fluorescence emission

Application of fluorescence spectroscopy to protein characterization is dependent on the presence of intrinsic and/or extrinsic fluorophores. Sidechains of aromatic amino acids (Trp, Tyr, Phe) and some cofactors (i.e., NADH, FAD) are intrinsic fluorophores, whereas in the case of non-fluorescent proteins, extrinsic fluorophores are covalently or non-covalently attached to assist in fluorescence-based characterizations. Depending on the type of interaction, formation of a fluorescent complex can generate changes in

emission intensity, λ_{max}, fluorescence lifetime (τ_f), polarization or quantum yield of the fluorophore. Monitoring of one or more parameters can provide both qualitative and quantitative information about protein structure and dynamics. For example, Trp fluorescence is extremely sensitive to the polarity of the indole environment, which is exhibited as a shift in λ_{max} from shorter (~305 nm) to longer (~355 nm) wavelengths with an increase in polarity of Trp surroundings. Red-shift in the λ_{max} of the fluorescence emission is accompanied by shorter τ_f, as solvent-exposed Trp transition faster to the ground state compared to buried Trp sidechains.

Hemoprotein fluorescence requires special consideration as fluorescence signals of intrinsic and extrinsic fluorophores are efficiently quenched by FePPIX, which absorbs across UV-visible region. Weber and Teale report that Trp fluorescence efficiency (Φ_F) is 100-fold higher in heme-free (apo) then in heme-bound (holo) globins (Weber and Teale 1959). To circumvent this experimental obstacle, globins are commonly reconstituted with free-base or metal-substituted protoporphyrins, as demonstrated in Chapter 5.

3.2.5.2. Fluorescence quantum yield

Fluorescence efficiency (Φ_F) is defined as the ratio of the number of photons emitted ($S_1 \rightarrow S_0$) relative to the number of total photons absorbed. Experimental determination of Φ_F requires use of a reference fluorophore that emits in a similar range as the sample. Fluorescence emission spectra of sample and reference solutions with identical optical densities (OD) are collected. To prevent inner-filter effect, OD should be kept under 0.1 in 1 cm path length. Integrated emission spectra are plotted as a function of OD and analyzed using the following equation:

$$\Phi_{F,sample} = \Phi_{F,reference} \frac{m_{sample}}{m_{reference}} \frac{\eta^2_{sample}}{\eta^2_{reference}} \quad \text{Eq 3.37}$$

where m is the slope of the linear plot, and η is the refractive index of the solvent. A detailed protocol for fluorescence quantum yield determination and troubleshooting of the experimental design was published before (Würth et al. 2013).

3.2.5.3. Steady-state frequency-domain fluorescence lifetime

Fluorescence lifetime is defined as amount of time a fluorophore spends in the excited state before undergoing $S_1 \rightarrow S_0$ transition (Lakowicz 2006). Decay of the fluorophore from the excited to the ground state is a first order process that can be determined using frequency-domain (FD) or phase-modulation measurements (Holde, Johnson, and Ho 1998). In FD measurements, a short pulse of light is sinusoidaly modulated to excite a fluorophore. The modulation frequency of excitation ($\omega = 2\pi \cdot frequency$) governs the time-delay of the fluorescence emission, which is observed as a shift in phase (ϕ_ω) to the lower frequencies (Figure 3.7). The example of the plot of modulation ratio and phase delay as a function of modulation frequency is shown in Figure 3.8.

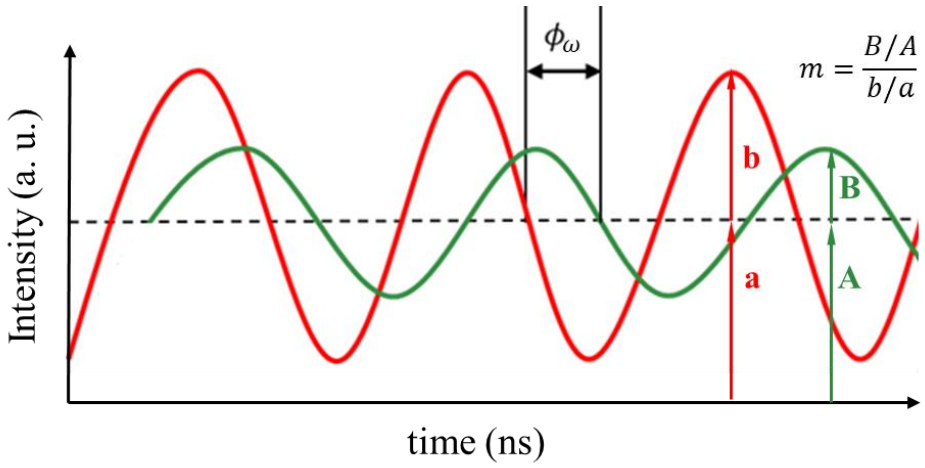

Figure 3.7. Modulation of excitation light intensity (red) decreases the modulation of emission (green) and induces the phase shift. The average intensity for both waves is indicated by a dashed line. The amplitude of the average intensity (a, A) and the offset from the average intensity (b, B) of emission and excitation, respectively, determines the modulation ratio (m).

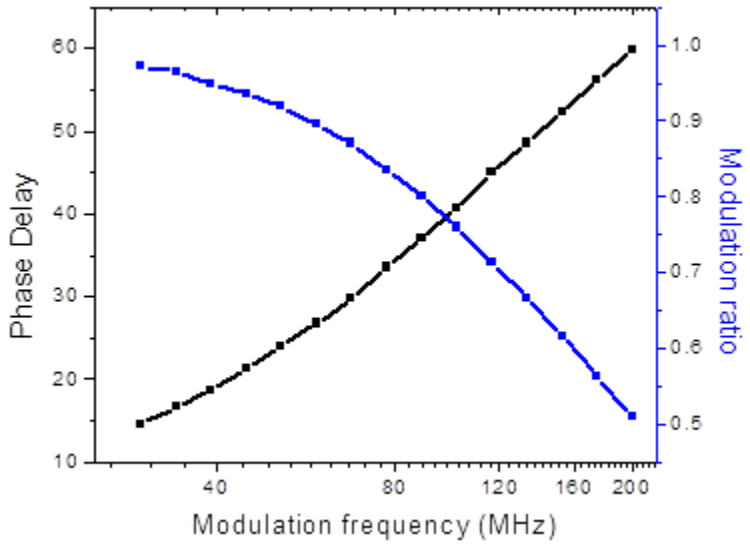

Figure 3.8. Modulation ratio (m) and phase delay (ϕ_ω) are plotted against modulation frequency (ω) to determine fluorophore lifetime.

In the case of a single-exponential decay, phase (τ_{ϕ_ω}) and modulation (τ_{m_ω}) lifetimes can be obtained if the modulation frequency (ω) is known:

$$\tau_{\phi_\omega} = \omega^{-1} \tan \phi \qquad \text{Eq 3.38}$$

$$\tau_{m_\omega} = \frac{1}{\omega}\left[\frac{1}{m^2} - 1\right]^{1/2} \qquad \text{Eq 3.39}$$

However, depopulation of the excited state of fluorophore is often a heterogeneous process, which requires the use of multi-exponential model. Total intensity observed I(t) is defined as a sum of first-order processes

$$I(t) = \sum \alpha_i e^{-t/\tau_i} \qquad \text{Eq 3.40}$$

where τ_i and α_i represent fluorescence lifetimes and pre-exponential factors associated with each fluorescence decay process. Pre-exponential factors (α_i) are a valuable parameter if a decay of a single fluorophore is monitored. Specifically, if the same fluorophore is found in different environments, the α_i values are proportional to the fractional population of fluorophore in each environment (Lakowicz 2006). Furthermore, the fraction of fluorescence intensity associated with each component contributing to the multi-exponential decay can be calculated using Eq 3.41 (Lakowicz et al. 1984).

$$f_i = \frac{\alpha_i \tau_i}{\sum_j \alpha_j \tau_j} \qquad \text{Eq 3.41}$$

Phase and modulation lifetimes for multi-exponential decays are extracted using transforms N_ω and D_ω, which are defined as

$$N_\omega = \frac{\sum_i \frac{\alpha_i \omega \tau_i^2}{(1+\omega^2 \tau_i^2)}}{\sum_i \alpha_i \tau_i} \qquad \text{Eq 3.42}$$

$$D_{\omega} = \frac{\sum_i \frac{\alpha_i \tau_i}{(1+\omega^2 \tau_i^2)}}{\sum_i \alpha_i \tau_i} \quad \text{Eq 3.43}$$

The phase angle and modulation ratio are then calculated using equations 3.44 and 3.45.

$$\tan \phi_{\omega,calc} = \frac{N_{\omega}}{D_{\omega}} \quad \text{Eq 3.44}$$

$$m_{\omega,calc} = (N_{\omega}^2 + D_{\omega}^2)^{1/2} \quad \text{Eq 3.45}$$

3.2.6. Phosphorescence

Another possible fate of fluorophores in the lowest vibrational level of S_1 is intersystem crossing to the excited triplet state (T_1). This nonradiative transition is caused by spin conversion which results in electrons of ground (S_0) and excited state (T_1) with the same spin (↑↑) (Lakowicz 2006). Since $T_1 \rightarrow S_0$ transition is spin-forbidden and requires change in multiplicity, decay to ground state is observed on substantially longer (millisecond-to-seconds) timescales. Phosphorescence spectra are red-shifted compared to fluorescence, as T_1 is lower in energy than S_1. Determination of phosphorescence properties require experimentation on concentrated samples and low temperatures as the quantum yield is generally very low ($\Phi_P \sim 10^{-6}$) (Lakowicz 2002). In addition, the amplitude of the phosphorescence intensity is efficiently quenched by O_2, therefore great care must be taken to deoxygenate samples before the experiment.

3.3. Computational Techniques

3.3.1. Molecular Dynamics Simulations

Advancement of computer technology, availability of high-resolution three-dimensional biomolecular structures and development of force fields for biomolecular systems propelled computational techniques such as molecular dynamics (MD) simulations to the frontline of biophysics research in the recent decades.

While experimental observations from spectroscopic techniques detailed in previous sections represent a sample average, MD probes dynamics of a single biomolecule per simulation. Therefore, to reliably correlate MD simulations to experimental data, sufficient sampling of protein conformations has to be performed. It has to be considered that a native protein exists in an ensemble of closely related substates. Interconversion between these substates is thermally accessible and can be observed with classical MD simulations. To probe energetically isolated conformations and/or to observe large domain motions, enhanced sampling techniques, such as accelerated or steered MD, should be employed.

3.3.2. Molecular Dynamics: Overview

Molecular dynamics (MD) methods simulate movement of atoms as a function of time using Newton's equations of motion. Because electron distributions are neglected, each atom type is treated as a single-point mass with an experimentally or theoretically determined partial charge. Atomic interactions are governed by a potential energy function (V), also known as force field. In this work CHARMM force field was used for

all MD simulations and is defined by functions presented in equations Eqs 3.46-3.48 (Mackerell et al. 1998).

$$V_{CHARMM} = V_{bonded} + V_{nonbonded} \quad \text{Eq. 3.46}$$

$$V_{bonded} = \sum_{bonds} k_b(b - b_0)^2 + \sum_{angles} k_\theta(\theta - \theta_0)^2 + \sum_{dihedrals} k_\phi[1 + \cos(n\phi - \delta)] + \sum_{impropers} k_\omega(\omega - \omega_0)^2 + \sum_{Urey-Bradley} k_u(u - u_0)^2 \quad \text{Eq.3.47}$$

$$V_{nonbonded} = \sum_{nonbonded} \epsilon \left[\left(\frac{R_{min_{ij}}}{r_{ij}} \right)^{12} - \left(\frac{R_{min_{ij}}}{r_{ij}} \right)^{6} \right] + \frac{q_i q_j}{\varepsilon r_{ij}} \quad \text{Eq. 3.48}$$

The potential function for bonding interactions (V_{bonded}) contains energy terms for bond stretching, angle bending, dihedral torsions, improper out-of-plane bending and Urey-Bradley 1-3 interactions (Mackerell et al. 1998), which are illustrated in Figure 3.9. Bond length (b) and angle (θ) between two and three consecutive atoms, respectively, are defined as harmonic oscillators with corresponding force constants, k_b and k_θ. Urey-Bradley component in CHARMM force field is energy cross term that couples fluctuations of angle between three sequential atoms (k_u) to the distance between the first and third atoms (u). Dihedral energy of four consecutive atoms accounts for periodicity (n) of the dihedral angle (ϕ), phase shift (δ) and dihedral force constant (k_ϕ) (Jensen 2007). It should be noted that k_ϕ is correlated to the size of barrier for rotation around the central bond (Jensen 2007). Furthermore, V_{CHARMM} contains a correction term that prevents formation of pyramidal geometry between three atoms bonded to a central sp^2-hybridized atom. This improper torsion energy term is defined by out-of-plane angle ω and a corresponding force constant k_ω. All force constants and equilibrium values (b_0, θ_0,

ω_0, u_0) are fixed parameters found in the CHARMM parameter files (Mackerell et al. 1998; Mackerell, Feig, and Brooks 2004).

Nonbonding interactions ($V_{nonbonded}$) between atoms i and j separated by at least three covalent bonds are determined by Leonard-Jones (L-J) and Coulomb potentials, which correspond to the first and second term in Eq. 3.48, respectively. The L-J potential accounts for attractive and repulsive van der Waals forces of two atoms separated by distance r_{ij}, where $R_{min_{ij}}$ and ϵ correspond to interatomic distance and well depth at the energy minimum (Mackerell et al. 1998). On the other hand, Coulomb potential relies on partial charges of atoms i and j (q_i, q_j), their distance (r_{ij}) and dielectric constant (ε) (Mackerell et al. 1998).

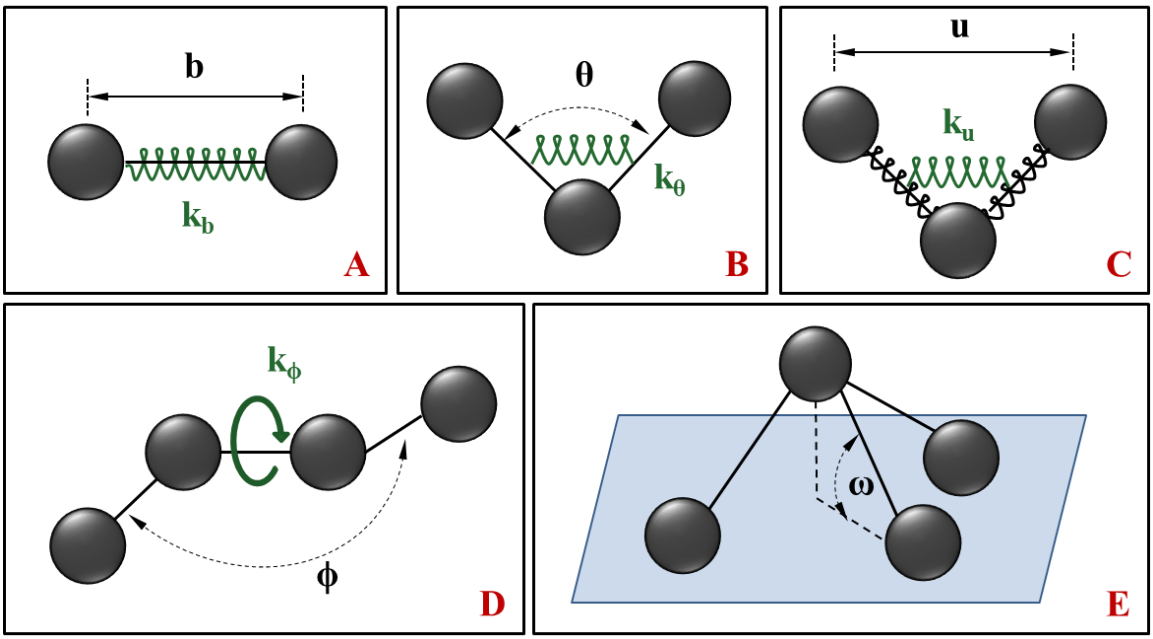

Figure 3.9. Diagrams of bonding variables: (A) bond energy, (B) angle energy, (C) Urey-Bradley energy term, (D) dihedral energy term, and (E) improper angle energy term.

Newton's second law is proportional to the partial derivative of the total interaction potential as a function of the position vector (r) of an atom, as shown in Eq. 3.49:

$$-\frac{\partial V}{\partial r} = F = ma = m\frac{dv}{dt} = m\frac{\partial^2 r}{\partial t} \qquad \text{Eq. 3.49}$$

At the start of the simulation, velocities are randomly assigned to all atoms in the system according to the Bolzmann distribution at the given temperature. The velocities of the subsequent steps ($v_{i+1/2\cdot\Delta t}, v_{i+\Delta t}$) in NAMD simulation package are determined by velocity-Verlet algorithm (Phillips et al. 2005). First, the position of the atom at the next time step ($r_{i+\Delta t}$) is calculated, which is followed by evaluation of the atom velocity at the half-step ($v_{i+1/2\cdot\Delta t}$). The forces ($F_{i+\Delta t}$) are computed next, followed by determination of

velocity at "full-step" ($v_{i+\Delta t}$) (Allen and Tildesley 1987; Phillips et al. 2005). The sequence of calculations in velocity-Verlet algorithm is shown in Eqs. 3.50-3.53.

$$v_{i+1/2\cdot\Delta t} = v_i + m^{-1}F_i \cdot \frac{\Delta t}{2} \quad \text{Eq. 3.50}$$

$$r_{i+\Delta t} = r_i + v_{i+1/2\cdot\Delta t} \cdot \Delta t \quad \text{Eq. 3.51}$$

$$F_{i+\Delta t} = F(r_{i+\Delta t}) \quad \text{Eq. 3.52}$$

$$v_{i+1/2\Delta t} = v_{i+1/2\cdot\Delta t} + m^{-1}F_{i+\Delta t} \cdot \frac{\Delta t}{2} \quad \text{Eq. 3.53}$$

It should be noted that the length of the timestep (Δt) is usually set to 10^{-15} s, in order to exceed carbon-hydrogen vibrational frequency (3300 cm^{-1} $\sim$ 10^{-14} s), the fastest process in a classically-treated system.

In this work, proteins were placed in a box surrounded by at least 8-10 Å buffer region filled with explicit waters molecules (Figure 3.10), resulting in a system containing approximately 20000 atoms.

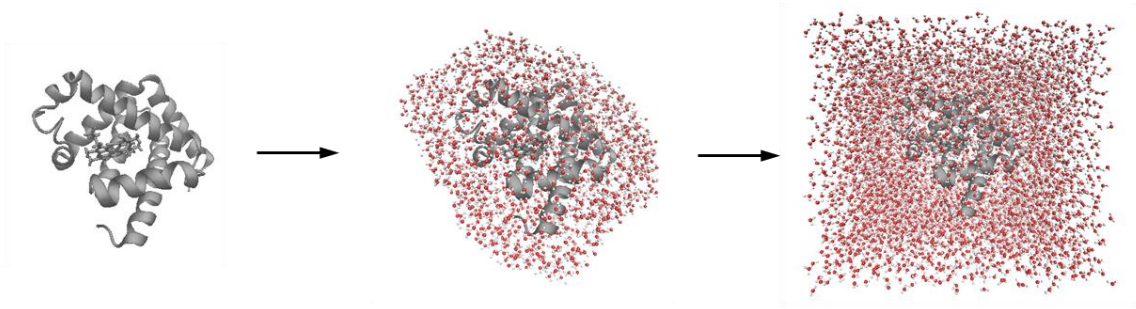

Figure 3.10. Preparation of solvated protein for MD simulations. A layer of water molecules is added to solvate the protein from all sides. Then, additional waters are added to create a water-filled box, necessary for PBC computations.

To overcome finite size effects, periodic boundary conditions (PBC) were employed. In PBC, the box containing the protein is virtually duplicated in all directions to infinity, as shown in Figure 3.11. Therefore, when a solvent molecule migrates into the neighboring box, it is replaced by another water molecule which enters from the neighboring box on the opposite side of the central box (Figure 3.11.B). Periodic boundary conditions also enable computation of electrostatic interactions beyond the boundary of the box. Here, nonbonding interactions were cutoff at 12 Å (R_2), with switching distance set at 10 Å (R_1). The switching approach allows gradient reduction of nonbonding interactions in R_1-R_2 range, as shown in Figure 3.12.

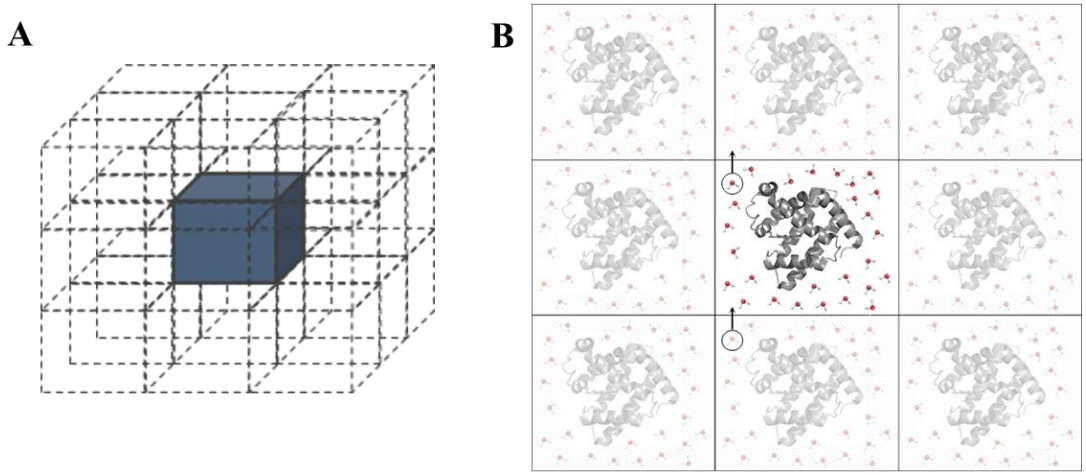

Figure 3.11. Illustration of periodic boundary conditions. (A) Three-dimensional view of PBC ensemble, where central box (blue) represents the image of the simulated system. (B) Simplified view of a PBC cross section demonstrating replacement of solvent molecules as they migrate across periodic boundaries.

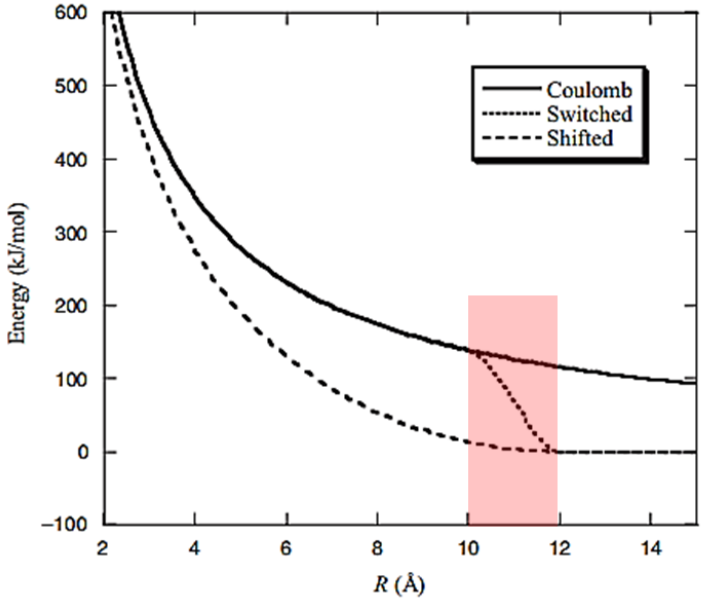

Figure 3.12. Illustration of theoretical Coulomb interactions between two interacting atoms. The highlighted portion shows the switching region. The figure is adapted from "Introduction to Computational Chemistry" book (Jensen 2007).

Starting structure considerations

Molecular dynamics simulations of proteins require thorough inspection of the PDB file in order to identify: (1) poorly resolved amino acids, and (2) protonation states of His residues. Determination of native protein structure can be impeded by flexible protein segments, as observed for CD region and terminal extensions in human Ngb (Pesce et al. 2003a) and Cygb (Sugimoto et al. 2004), respectively. If only partially resolved structures of the protein of interest are available, homology modeling algorithms (Sali et al. 1995; Song et al. 2013) may be employed to predict the conformation of the flexible region based on evolutionarily similar proteins with known three-dimensional structures. Furthermore, because X-ray diffraction is the predominant experimental technique in protein structure elucidation, locations of hydrogen atoms are unknown, although their coordinates can be generally predicted. However, because histidine residues have pKa close to neutral ($pKa \sim 6.5$), three His protonation states have to be considered: doubly-protonated positively charged sidechain, as well as N_{δ}- or N_{ε}-protonated neutral tautomers, as shown in Figure 3.13. When NMR data are not available, His protonation states have to be guessed based on the sidechain orientation with respect to surrounding residues, in order to elucidate if hydrogen bonding geometry is satisfied. Several algorithms such as PROPKA (Rostkowski et al. 2011) predicts charge states of titratable residues based on solvent accessibility of the sidechain and its interaction with the immediate environment.

In addition to protein structure refinement, location of crystal water molecules should be evaluated as well. Apart from playing crucial role in protein folding, protein-

water interactions have been shown to have an important structural (Likić et al. 2000; Rhodes et al. 2006) and catalytic function (Knight et al. 2009). Depending on the tertiary structure of the protein, location of these "static" water molecules may not be evident from the crystal structure; therefore crystal waters should be included in the simulation starting structure as well.

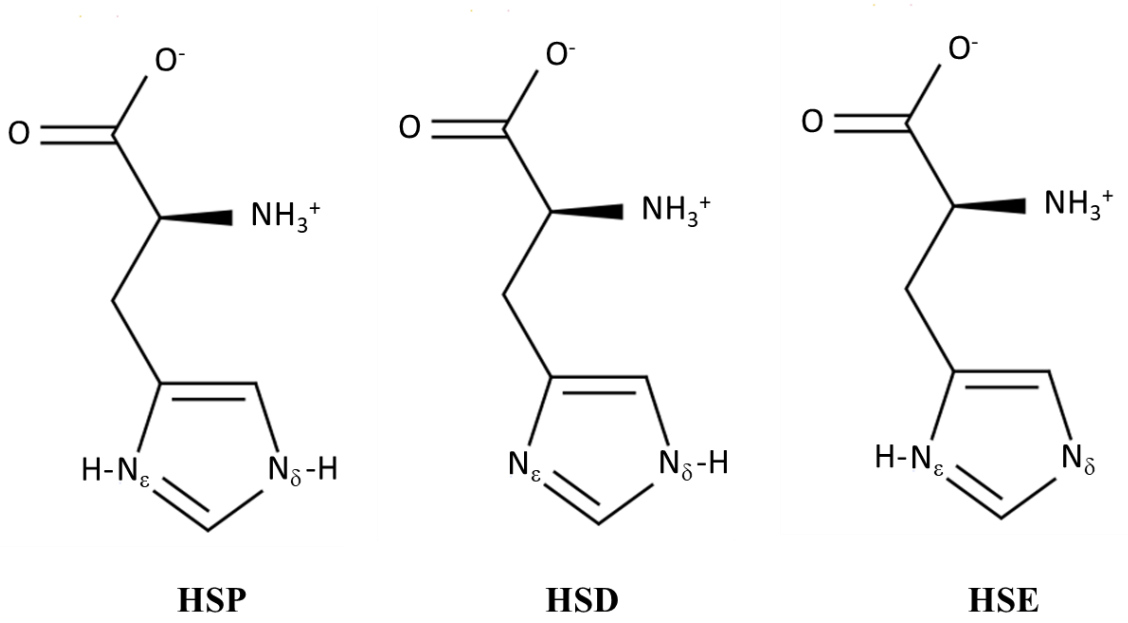

Figure 3.13. CHARMM nomenclature for possible protonation states of histidine side chain close to neutral pH.

Root-Mean-Square Analyses

Molecular dynamics simulations are generally validated by comparing the displacement of backbone or α-carbon atoms against the reference/starting structure ($r_{\alpha,ref}$). The plot of root-mean-square-deviation (RMSD) versus time (Eq. 3.54) is commonly used to evaluate if the simulated ensemble reached a stable, equilibrated conformation.

$$RMSD(t) = \sqrt{\frac{\sum[r_{\alpha}(t) - r_{\alpha,ref}]^2}{N}} \qquad \text{Eq. 3.54}$$

In addition, per-residue RMSD (Eq. 3.55) and root-mean-square-fluctuation (RMSF; Eq. 3.56) plots can be obtained to gain insight into global and local protein motions, respectively. Figure 3.14., which was previously published by Kuzmanic and Zagrovic, illustrates that per-residue RMSD calculations is an all-against-all structural comparison, whereas RMSF measures deviations of all atoms against the reference structure (Kuzmanic and Zagrovic 2010). It should be noted that prior to performing RMS analyses, simulation frames in the trajectory need to be superimposed through least-squares fitting by rotation and translation of all snapshots with respect to the reference (starting) structure.

$$per - residue\ RMSD = \sqrt{\frac{\sum_{i=1}^{N_{atoms}}[r_i(1) - r_i(2)]^2}{N_{atoms}}} \qquad \text{Eq. 3.55}$$

$$per - residue\ RMSF = \sqrt{\frac{1}{T}\frac{\sum_{i=1}^{T}[r_i - r_{ref}]^2}{N_{atoms}}} \qquad \text{Eq. 3.56}$$

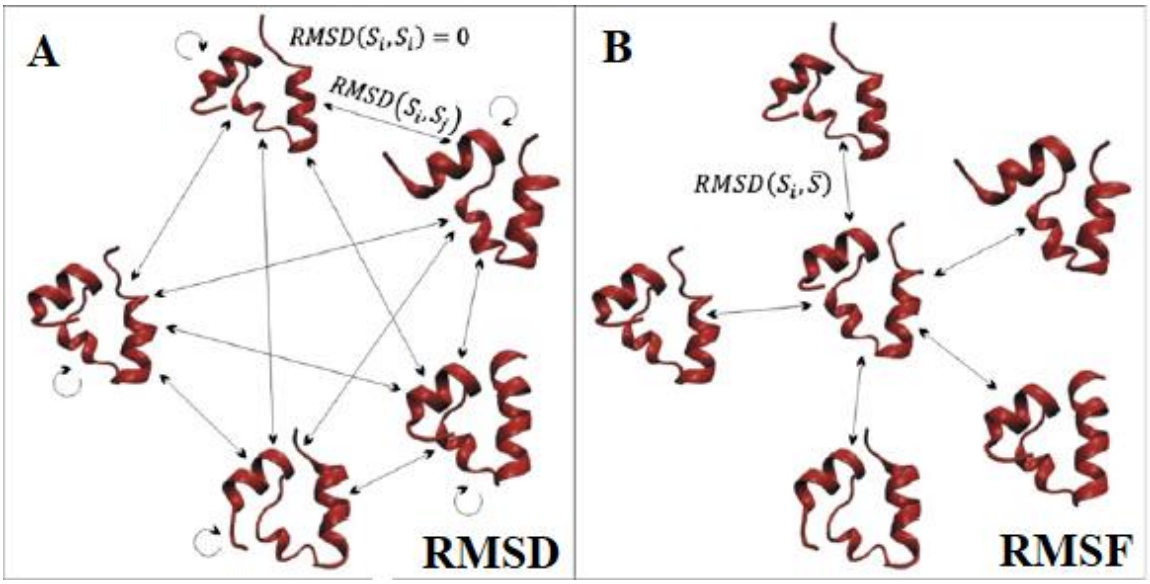

Figure 3.14. Illustration of differences between per-residue RMSD and RMSF calculations. The figure is adapted from "Determination of Ensemble-Average Pairwise Root Mean-Square Deviation from Experimental B-Factors" publication in Biophysical Journal. (Kuzmanic and Zagrovic 2010)

3.4. Summary

Biophysical characterizations of recombinant hexacoordinate globins were achieved using a variety of optical methods. Figure 3.15. summarizes some of the processes monitored in this work. Time scales of physical events, such as protein dynamics and ligand-protein interactions are compared to temporal resolution of methods used here. Combination of experimental and computational techniques has allowed development of structure-function models for hexacoordinate globins.

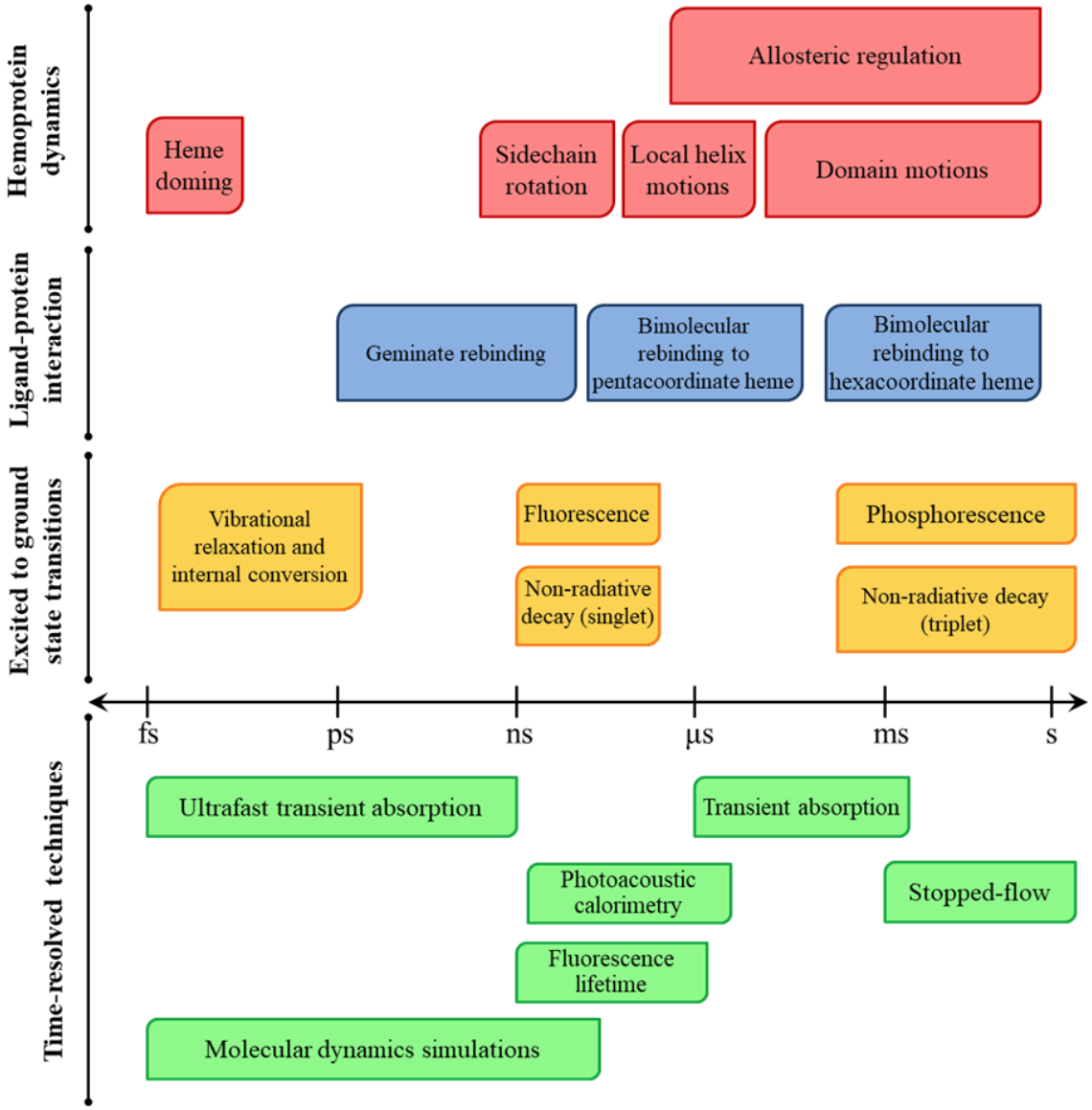

Figure 3.15. Timescales of protein dynamics (red), diatomic ligand-hemoprotein interactions (blue), excited-to-ground state transitions (orange) and temporal resolution of techniques (green) employed in this work.

3.5 Methods: Chapter 4

Sample preparation for ultra-fast TA

All CO-bound samples were prepared by diluting freshly thawed recombinant protein stock in 50 mM Tris HCl pH 7.0. For samples with reduced disulfide bond, proteins were dialyzed overnight (Spectra/Por dialysis membrane, 3500 Da cutoff, Spectrum Labs) in 50 mM Tris HCl 10 mM DTT pH 7.0. Samples were placed in a 1.0 x 0.2 cm quartz cuvette, sealed with septum cap (size 14, Kimble Chase) and parafilm, and then purged with argon for at least 15 minutes. Freshly obtained sodium dithionite was dissolved in Tris buffer and added to deoxygenated sample until $OD_{320} \sim 1.0$. Formation of the deoxy state was confirmed with UV-vis, before purging the cuvette with CO for 15 mins. Absorbance of all CO-bound samples was approximately 0.4 at 400 nm. The samples were kept on ice until arrival at University of Miami, where they were transferred into a 1.0 x 0.2 cm quartz cuvette that is suitable for ultra-fast measurement. All samples were excited at 400 nm, using a 1-8 μJ/laser pulse. Prior to each experiment, alignment of the instrument was confirmed by monitoring ligand rebinding kinetics of CO-bound horse heart Mb (Sigma).

3.6 Methods: Chapter 5

ZnPPIX incorporation into hexacoordinate globin fold

Heme extraction was performed according to the protocol introduced by Teale (Teale 1959). Purified recombinant protein was denatured by dropwise addition of HCl until pH reached ~2.0. The acidified solution containing unfolded protein was mixed with equal volume of ice-cold 2-butanone (Acros Organics, 99+% spectroscopic grade)

and vigorously shaken for a few seconds. The mixture was placed on ice until separation of the aqueous and organic phase was observed. The aqueous phase containing the unfolded apo-protein was extracted and dialyzed overnight at pH 2.4 to remove residual 2-butanone.

Following dialysis, the pH of dialyzed apo-protein was adjusted to 7.0 by addition of 2 M NaOH. A solution containing 8 M GuHCl and 10-fold excess of solid ZnPPIX (Frontier Scientific) was briefly sonicated to homogenize the mixture and added to the apo-protein. The final concentration of GuHCl was 6.0 M. Serial dialysis of the apo-protein/ZnPPIX/GuHCl mixture was performed in the dark at room temperature to remove excess GuHCl. The final solution was filtered using a 0.22 μm filter and stored at 4°C.

Steady-state fluorescence emission spectroscopy

The ZnPPIX-incorporated proteins were diluted in 50 mM Tris HCl pH 7.0 buffer and placed in a 0.2 x 1.0 cm quartz cuvette. Steady-state emission spectra were obtained with Cary Eclipse Fluorescence Spectrophotometer using λ_{exc}= 552 nm and 10 nm slits for excitation and emission path.

Solution of ferric Cyt *c* was prepared as described before (Tiwari et al. 2015), and was titrated into 7 μM ZnPPIX-incorporated hNgbWT (ε_{280}=28.545 mM^{-1} cm^{-1}) in 10 mM phosphate buffer pH 7.0. Complex formation was monitored by measuring emission spectra from 570-800 nm using λ_{exc}=552 nm and 10 nm slits. All data were corrected for inner filter effect, as described previously (Jameson 2014; Lakowicz 2006).

In addition, fluorescence quantum yields of reconstituted globins were determined using Rose Bengal (Aldrich Chem Co.) dissolved in spectroscopic grade methanol (Alfa Aesar) as a reference ($\Phi_F = 0.11$). Optical density of samples and reference at excitation wavelength and 10 mm path were less than 0.06. The data were analyzed according to the previously published protocol (Würth et al. 2013), and as described in Methods section 3.2.5.2.

Time-resolved fluorescence lifetime spectroscopy

Determination of excited-state fluorescence lifetime was performed on Chronos Spectrofluorometer (ISS) using 378 nm laser diode with 370 nm bandpass excitation filter (Andover Corp.) and a 400 nm long pass emission filter (Andover Corp.). The ZnPPIX reconstituted proteins (in 50mM Tris HCl, pH 7.0) and reference (POPOP in ethanol, τ_{ref}= 1.35) were placed in 0.2 x 1.0 cm quartz cuvette. Time-domain measurements were obtained on 15 modulation frequencies between 30-200 MHz and data were analyzed using Vinci Software (ISS).

Phosphorescence

Transient absorption spectroscopy was used to monitor phosphorescence decay of ZnPPIX-incorporated globins as described by Papp and coworkers (Papp et al. 1990). Samples were prepared in a 0.2 x 1.0 cm quartz cuvette, sealed with a septum cap and parafilm, and then deoxygenated in the dark with argon for one hour. The cuvette with the sample was then placed into a cell holder and excited with a Nd:YAG laser (Minilite, Continuum) with a 532 nm output (pump beam). The decay was monitored with 447 nm

diode-pumped solid state laser (MDL-III-447, Changehun New Industries Optoelectronics Tech Co. Ltd.). Optical density of all reconstituted proteins at 532 nm was 0.04.

3.7 Methods: Chapter 6

Circular dichroism: steady-state and denaturation studies

All Cygb constructs were expressed and purified as described in Methods section 3.2.1. For steady-state measurements, proteins were diluted in 50 mM TrisHCl pH 7.0 and concentration (ε_{280}=30.035 mM^{-1} cm^{-1}) was checked via UV-vis, prior to the start of the experiment. In thermal denaturation studies, 20 µM protein samples in 50 mM TrisHCl 200 mM GuHCl, pH 7.0 were placed in temperature-controlled cuvette holder. Protein unfolding was monitored at 222 nm in the temperature range of 25-100°C, using 1°C data pitch and rate of 1°C/min. Unfolding curves were analyzed according to the previously established protocol (Greenfield 2006). All CD spectra were recorded by J15 CD spetropolarimeter (Jasco, USA) using a quartz cuvette with a cell path of 0.1 cm.

Acid-induced unfolding

Steady-state tryptophan fluorescence emission measurements were carried out on a Cary Eclipse Fluorescence Spectrophotometer (Agilent Technologies). Samples contained 5-15 µM Cygb constructs in 5 mM citrate phosphate buffer, with pH ranging from 2.3 to 7.2. Excitation wavelength was 280 nm, and the emission spectra were collected from 290-500 nm.

1,8-ANS binding

Steady-state fluorescence emission spectra were collected for vertebrate globins (hhMb, hNgbWT, hHb, human Cygb with (hCygbWT^{ox}) and without (hCygbWT^{red}) the disulfide bond), as well as Cygb constructs (hCygbΔN^{red}, hCygbΔC^{red}, hCygbΔNΔC^{red}) in the presence of 2-fold excess of 1-analinonapthalene-8-sulfonic acid (1,8-ANS, Aldrich). All samples were excited at 350 nm and data was collected by Cary Eclipse Fluorescence Spectrophotometer (Agilent Technologies).

Full-length human cytoglobin model

A full length model of human Cygb wild type (residues 2-186) was prepared with Modeller 9.14 software (Sali et al. 1995) by fusing both chains of PDB entry 2DC3 into a single monomer containing N- and C- terminal extensions, using chain A as a template. Using the model evaluation by DOPE algorithm, highest scoring structure was used as a starting point for all simulations in chapter 6. The root mean square deviation of backbone atoms of the full-length model compared to 2DC3 chains A and B were 0.46 and 0.51 Å. In comparison, RMSD of the backbone atoms between chain A and chain B is 0.38 Å. The final structure did not contain disulfide bond or any crystal waters.

Cygb simulations

Molecular dynamics simulations were performed for bis-histidyl/hexacoordinate Cygb in the presence and absence of the disulfide bond. For all simulations, the starting structure was full-length Cygb model described above. Neutral histidine tautomers were estimated using distance and geometry with neighboring residues, and were as follows:

HSE 65, HSD 81, HSD 97, HSD 113, HSE 117 and HSD 161. For Cygb simulations with oxidized Cys-Cys bond, the disulfide patch was manually added. Trajectories were computed using all-atom molecular dynamics, CHARMM27 force field and NAMD 2.10 software package (Mackerell, Banavali, and Foloppe 2001; Phillips et al. 2005). Each structure was placed in a periodic TIP3P water box with 10 Å margins. Particle-mesh Ewald algorithm was used for long-range electrostatics with resolution of 1 Å, and all non-bonded interactions were calculated using a 12 Å cutoff. All systems were first minimized for 10000 steps, heated gradually to 300 K at a rate of 0.005 K/step, and equilibrated for 200 ps. Simulations were carried out for 100 ns, at 300 K with 1 fs timestep, using Langevin dynamics for temperature and pressure control. Hydrogens were constrained only on water molecules. The average root mean square deviation (RMSD) of the backbone atoms of the globin core (residues 21-169) was checked to confirm that a stable conformation was achieved. The first 20 and 55 ns were discarded for simulations of the hexacoordinate Cygb with ($hCygbWY^{ox}$) and without ($hCygbWT^{red}$) the disulfide bond. Hydrogen bonds were evaluated using VMD software (Humphrey, Dalke, and Schulten 1996) using 3.0 Å and 30° as distance and angle cutoff, respectively.

Docking studies

Equilibrated structure of $hCygbWT^{red}$ was extracted from the 100 ns MD simulation and was used as a target conformation for the receptor, whereas the structure of 1,8-ANS was retrieved from ZINC database (http://zinc.docking.org/). Screening and refinement of docking complexes was performed by YASARA software (Yet Another Scientific

Artificial Reality Application, www.yasara.org). The highest scoring complex with 1,8-ANS bound to hCygbWT^{red} N terminus was used for further analysis.

3.8 Methods: Chapter 7

Molecular dynamics protocol and parameters

Molecular dynamics trajectories were obtained for hexa- and penta-coordinated hNgbWT^{ox}, hNgbWT^{red}, hNgb Y44F^{ox} and hNgb Y44F^{red}. The starting structure for all simulations was adopted from PDB entry 4MPM, chain B, in which Tyr44 is oriented towards the heme-7-propionate (Guimarães et al. 2014). To simulate reduced and pentacoordinated Ngb, the disulfide patch and His64-Fe bond were manually deleted, respectively. *In silico* mutations of residue 44 were performed with the PyMOL Molecular Graphics System, Version 1.8 Schrödinger, LLC. Trajectories were computed using all-atom molecular dynamics, CHARMM27 force field and NAMD 2.10 software package (Mackerell, Banavali, and Foloppe 2001; Phillips et al. 2005). Each structure, including crystal waters, was placed in a periodic TIP3P water box with 8 Å margins. Particle-mesh Ewald algorithm was used for long-range electrostatics with resolution of 1 Å, and all non-bonded interactions were calculated using a 12 Å cutoff. All systems were first minimized for 10000 steps, heated gradually to 300 K at a rate of 0.005 K/step, and equilibrated for 200 ps. Simulations were carried out for at least 50 ns, at 300 K with 1 fs timestep, using Langevin dynamics for temperature and pressure control. Hydrogens were constrained only on water molecules. VMD Plugins were utilized in analysis of MD trajectories.

4. REACTIVITY OF HEXACOORDINATED HEME PROTEINS ON ULTRAFAST TIMESCALES

4.1. Introduction

Heme proteins have been traditionally used as model systems to study the role of fast protein dynamics (picosecond to nanosecond timescale) as the photo-labile iron-ligand bond can be photolyzed within 60 femtoseconds with a quantum yield close to unity (Liebl et al. 1999; Zhu, Sage, and Champion 1994). Subsequently, the alteration of the heme group as well as migration of the photolyzed ligand through the protein matrix can be readily monitored using various spectroscopic techniques including infrared, Raman, and absorption spectroscopy as well as time resolved X-ray spectroscopy. Based on the results from numerous studies of native proteins as well as protein with modified amino acid residues within the heme binding pocket, a general model for ligand photo-dissociation and migration between the heme binding pocket and surrounding solvent has been proposed (Maurizio Brunori and Gibson 2001; Olson, Soman, and Phillips 2007; Scott, Gibson, and Olson 2001; Šrajer et al. 2001) and is shown in Figure 4.1. Upon photo-cleavage of the iron – gaseous ligand bond, the ligand initially resides within the heme binding pocket above the heme plane, forming a so-called geminate pair (state B in Figure 4.1). Subsequently, the ligand molecule migrates into the permanent or transient hydrophobic cavities within the protein matrix (state C). On the longer timescale, the photo-dissociated ligand may rebind back to the heme iron through so-called geminate rebinding process, or may migrate to the surrounding solvent (state D) and rebind back to

the heme iron on microsecond or millisecond timescales through so-called bimolecular rebinding step.

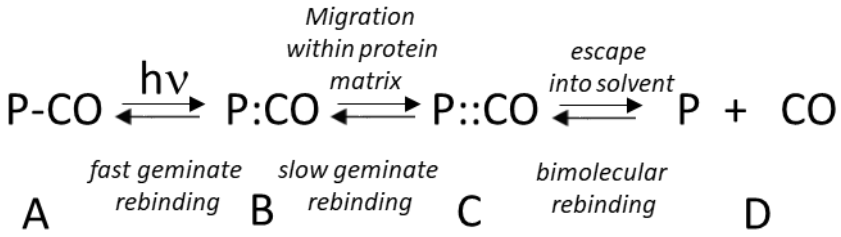

Figure 4.1. Globin-ligand interactions following photodissociation of CO from heme iron.

The migration pathways, rates and quantum yields for each step strongly depend on the heme protein, as well as properties of gaseous ligands. In case of the penta-coordinated globins, such as myoglobin, the quantum yield for the CO geminate rebinding is low (Φ_{gem}= 0.04) and occurs on a relatively slow timescale with a time constant of 180 ns (Henry et al. 1983; Huang and Boxer 1994). Despite the fact that numerous pathways have been proposed for CO migration in myoglobin (Mb) and hemoglobin (Hb) based on experimental and computational studies, it has been established that the photo-dissociated CO molecule samples hydrophobic cavities in the vicinity of the heme pocket and then escapes through the so-called distal histidine gate when the distal histidine side chain swings towards the solvent, opening a transient pathway for CO migration (Scott, Gibson, and Olson 2001; Šrajer et al. 2001). On the other hand, other gaseous ligands, such as O_2 and NO, show significantly larger geminate quantum yield and rate constants for geminate and bimolecular rebinding (Gibson et al. 1992). For example, the quantum yield for geminate nitric oxide rebinding to Mb is 0.9 and the time constants for geminate rebinding are 19 ps and 126 ps (Kholodenko et al.

1999). The slow CO binding to heme iron was associated with the high enthalpy barrier, as CO can only bind to the heme iron situated within the heme plane whereas NO can associate to the iron out of the heme plane (Andrew et al. 2016).

Characterization of the rate constant for gaseous ligand binding and escape from heme proteins provides crucial information about the reactivity of the heme iron, the mechanism of the fine tuning of the heme iron affinity for diatomic molecules, as well as the role of protein dynamics in controlling ligand migration rates. Here we have used femtosecond transient absorption spectroscopy to monitor CO association to hexa-coordinate globins on the picosecond timescale. In addition, the impact of distal histidine residue on picosecond CO rebinding was probed by measuring ligand rebinding kinetics to hNgb and hCygb with distal histidine mutated to glutamine. We selected glutamine residue to replace histidine because its sidechain does not coordinate to heme iron and has a van der Waals volume similar to that of native histidine residue (Astudillo et al., 2012). In addition, the picosecond CO rebinding was also studied in vertebrate globins with the reduced disulfide bond, hNgbWT^{red} and hCygbWT^{red} as well as in hCygb with mutated disulfide-forming Cys residue (hCygbC38S).

4.2. Results

The protein samples were prepared as described in Methods section 3.2.5. and the formation of CO-bound protein was verified based on UV-vis spectra (Figure 4.2) as shown for hhMb, hCygbWT and hNgbWT. The deoxy spectra are in agreement with the presence of the penta-coordinate heme iron in hhMb as evident from a broad Soret band at 435 nm and a visible band at 556 nm, whereas hexa-coordinate heme iron in hCygbWT

and hNgbWT exhibits two absorption peaks centered at 531 nm and 561 nm and a narrow Soret band at 428 nm (Astudillo et al., 2012; Astudillo et al., 2013). Absorption spectra for hHb, hNgbH64Q and hCygbH81Q were characteristic of penta-coordinate species, whereas hNgbWT^{red}, hCygbWT^{red} and hCygbC38S have spectra comparable to WT proteins (data not shown).

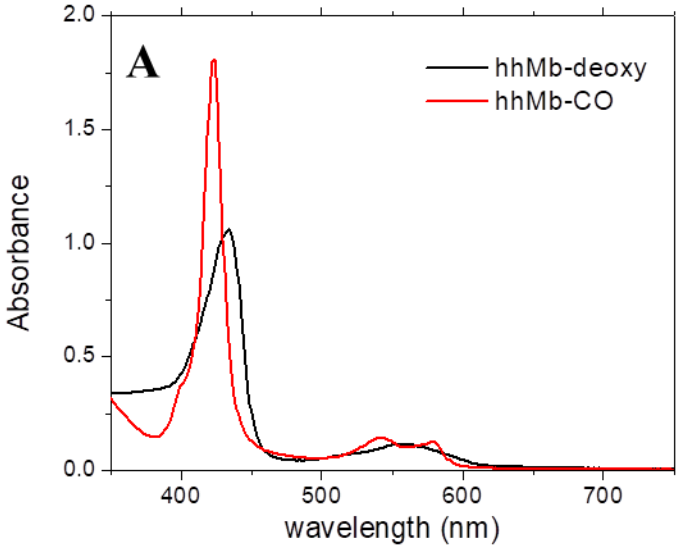

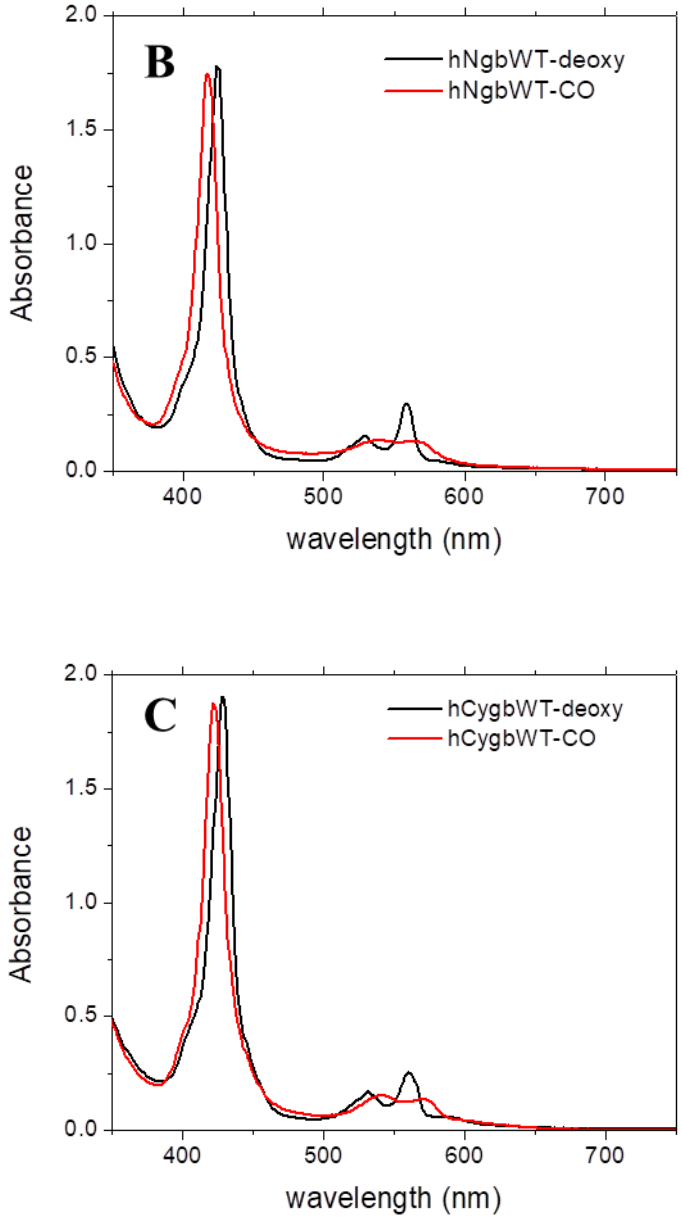

Figure. 4.2. Steady state absorption spectra of hhMb (panel A), hNgbWT (panel B) and hCygbWT (panel C) in the deoxy and CO-bound form.

The transient absorption traces obtained for CO-bound hHb, hhMb, hNgbWT and hCygbWT up to 150 ps are shown in Figure 4.3. The absorption signal in the range between 400 nm and 450 nm corresponds to the changes in the axial ligation as well as

the optical density change associated with the relaxation of the photo-excited heme group to the thermal equilibrium (X. Ye et al. 2003; Z. Zhang et al. 2009). In the case of hexa-coordinate globins, the initial amplitude rapidly decreases up to ~50 ps, whereas for penta-coordinate globins, the initial decrease in the amplitude is minimal. The data were analyzed using a multi-exponential decay function and the fitting parameters are summarized in Table 4.1. For both penta- and hexa-coordinate globin, the initial decay in the amplitude occurs with time constant of 5 to 10 ps. No additional kinetics were resolved on the timescale up to 1 ns for penta-coordinate globins and hNgbWT, whereas a kinetic process with a time constant of 218 ps was observed for hCygbWT, which we attribute to CO rebinding.

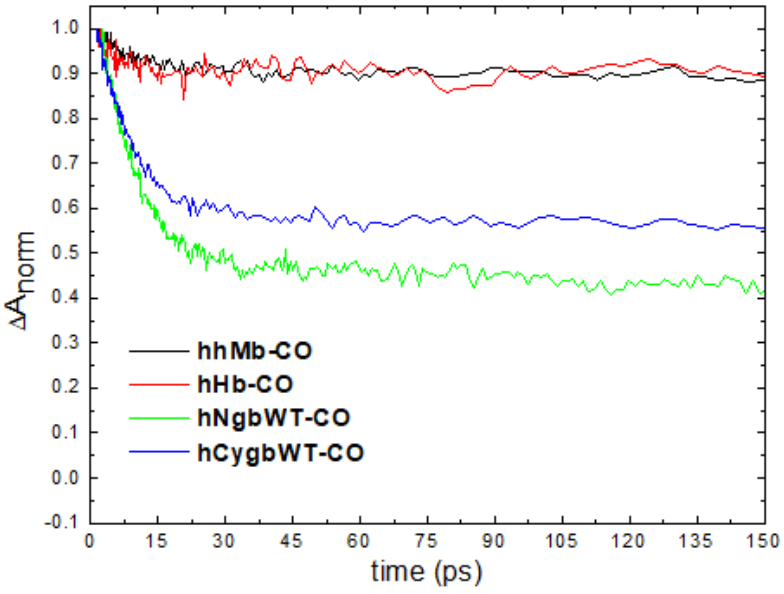

Figure 4.3. Kinetics for CO rebinding to hhMb, hHb, hNgbWT and hCygbWT on the picosecond timescale (up to 150 ps) measured in the peak of the increase of the decay associated spectrum. Experimental conditions: 40 µM protein in 50 mM Tris buffer pH 7.0, 35 fs pump beam of 400 nm, temperature 20 °C.

To determine the impact of distal histidine on the fast ligand rebinding in vertebrate globins, we monitored the picosecond kinetics for CO rebinding to hNgbH64Q and hCygbH81Q. The kinetic traces are presented in Figure 4.5, and the rate constants are summarized in the Table 4.1. Interestingly, the replacement of the distal histidine leads to a substantial decrease in the initial amplitude and the traces recorded for CO rebinding to hCygbH81Q are nearly superimposable to that recorded for the ligand binding to hhMb (Figure 4.4, Inset). The 218 ps kinetic phase that is observed for CO rebinding to hCygbWT is missing in the H81Q mutant suggesting that the replacement of the His residue prevents fast CO geminate rebinding to the heme iron. On the other hand, the replacement of the distal histidine by Gln in Ngb leads to a new 457 ps kinetic phase that has not been observed in the hNgbWT, suggesting that the substitution of the distal histidine by Gln alters the organization of the residues in the distal heme cavity, therefore promoting the fast CO geminate rebinding.

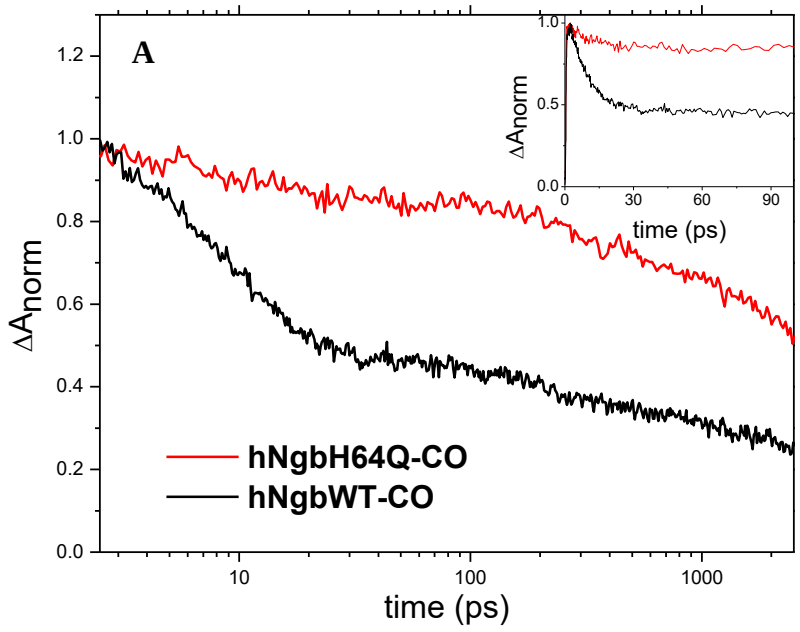

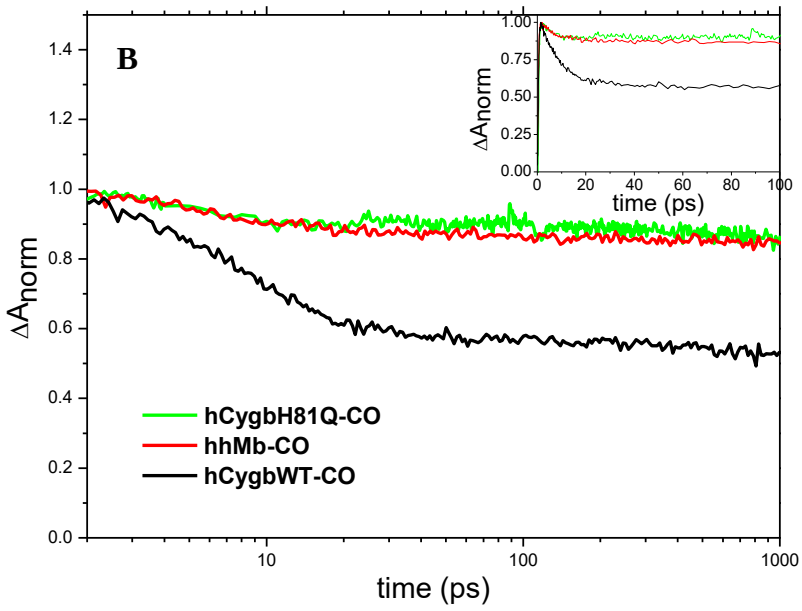

Figure 4.4. Semilogarithmic plot for CO rebinding kinetics to hNgbH64Q (A) and hCygbH81Q (B) measured in the positive peak of the decay associated spectrum. Inset show the kinetics (up to 100 ps) with linear scale for x-axis. Experimental conditions: 40-70 µM protein ($OD_{400} \approx$ 0.4) in 50 mM Tris buffer pH 7.0, 35 fs pump beam pulse with excitation wavelength at 400 nm, temperature 20 °C.

Unlike penta-coordinate vertebrate globins, the structural and functional studies of hNgbWT and hCygbWT revealed the presence of an intramolecular disulfide bridge between Cys46 and Cys55 in hNgbWT, and Cys38 and Cys83 in hCygbWT. Although the location of the disulfide bridge in hNgbWT and hCygbWT are distinct (Figure 4.5), as the disulfide bond in hNgbWT is located in the CD region, whereas the disulfide bond in hCygbWT connects helices B and E, the formation of the disulfide bond in both proteins modulates heme affinity for O_2 through alteration of the heme iron affinity for distal histidine (Hamdane et al. 2003). The disulfide bonds were reduced by incubating of hNgbWT or hCygbWT with 10 mM DTT overnight. In addition, we have investigated the picosecond CO rebinding to hCygb strain with Cys38 replaced by Ser.

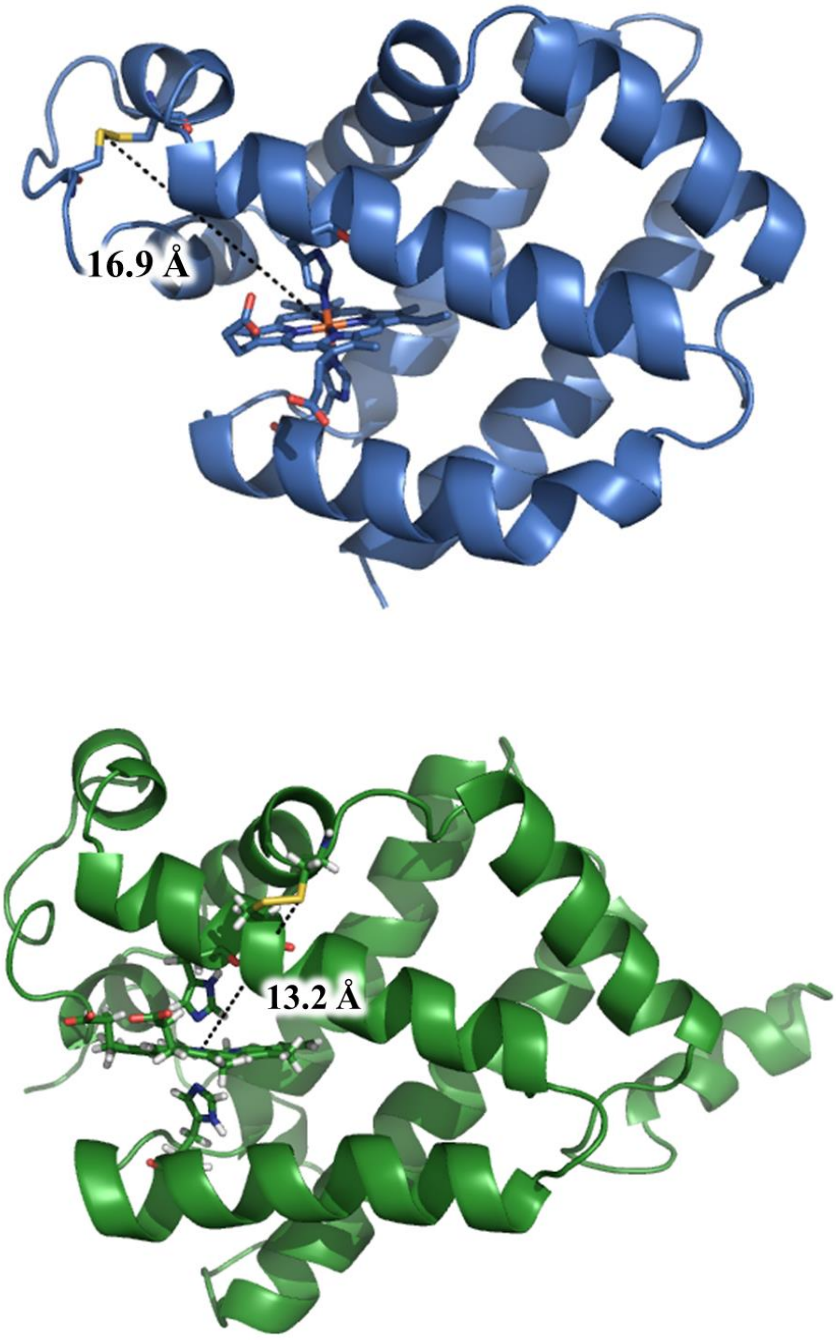

Figure 4.5. The position of the intramolecular disulfide bond between Cys46 and Cys55 in hNgbWT (top, PDB: 4MPM) (Guimarães et al. 2014); and Cys 38 and Cys 83 in hCygbWT (bottom). The model of the full-length hCygbWT with intra-protein disulfide bond was prepared as described in Chapter 3.7.

	λ_{probe} (nm)	τ_1 (ps)	A_1 (%)	τ_2 (ps)	A_1 (%)	τ_3 (ps)	A_3 (%)
hhMb	440	10.0 ± 0.7	11	> 5000	89	n. a.	n. a.
hHb	437	5.5 ± 1.1	14	> 1000	86	n. a.	n. a.
hNgbWT	437	8.4 ± 0.1	47	> 2000	53	n. a.	n. a.
hCygbWT	441	7.7 ± 0.1	59	218±20	10	> 2000	31
hNgbH64Q	437	9.0 ± 1.2	12	457±115	15	> 1 ns	73
hCygbH81Q	441	2.4 ± 0.4	4	> 5000	96	n. a.	n. a.
hNgbWT^{red}	437	7.0 ± 0.1	77	22 ± 1.3	16	> 2000	7
hCygbWT^{red}	441	8.0 ± 0.2	77	77 ± 7.2	11	> 5000	12%
hCygbC38S	441	7.2 ± 0.1	88	63 ± 6.7	5	> 2000	7%

Table 4.1: Kinetics for CO rebinding to hNgb and hCygb compared to penta-coordinate globins hHb and hhMb.

The transient absorption traces for CO rebinding to hNgbWT^{red} and hCygbWT^{red} are shown in Figure 4.6 and are clearly distinct from those recorded for the proteins with the intra-protein disulfide bond. Remarkably, the amplitude associated with the first time constant is 77% for hNgbWT^{red} and hCygbWT^{red}, and 88% for hCygbC38S. This 18-30% decrease in A_1 points towards strong coupling between the disulfide bond and the heme environment, even on picosecond timescale. Furthermore, τ_2 values suggest that an additional kinetic process occurs faster than 100 ps only in the absence of disulfide bond, which we attribute to CO rebinding based on comparison of transient traces associated with the first two time constants (data not shown).

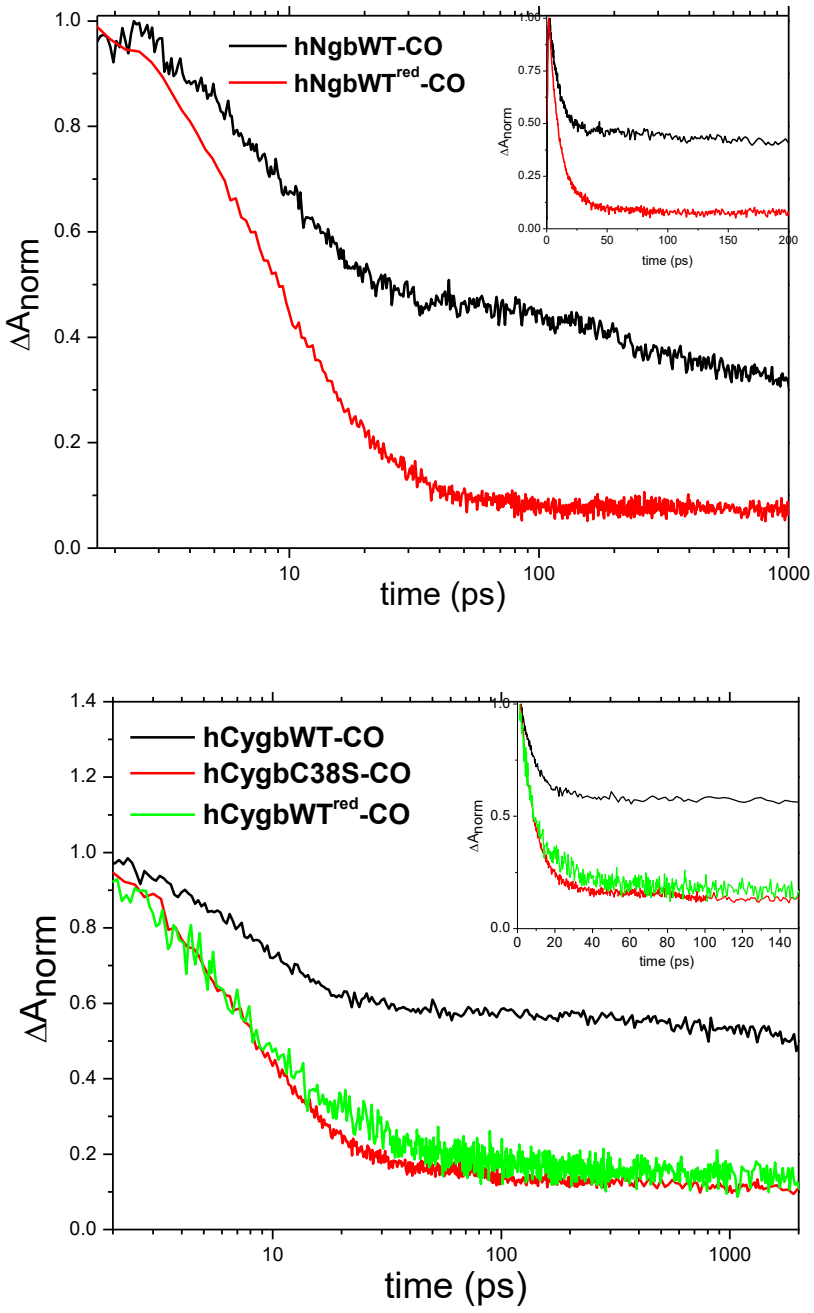

Figure 4.6: Kinetics for CO rebinding to hNgb and hNgbWT^{red} (top) and hCygb, hCygbWT^{red} and hCygbC38S (bottom) on the picosecond timescale (up to 150 ps) measured in the peak of the increase of the decay associated spectrum. Experimental conditions: 40 µM protein in 50 mM Tris buffer pH 7.0, 35 fs pump beam of 400 nm, temperature 20 ^{o}C.

4.3. Discussion

The picosecond transient absorption determined in the Soret band region indicates that the presence of the distal histidine as well as the internal disulfide bond strongly impact the initial 5-10 ps decay. The initial phase occurring with the time constant of 5 to 10 ps can be attributed to the cooling of the electronically excited heme. Using time resolved absorption spectroscopy, Martin *et al*. have shown that the excess energy from the photo-excited heme is transferred to the protein with a time constant of 5 ps (Petrich, Poyart, and Martin 1988). Kitagawa *et al*. have reported a biphasic heme relaxation with time constants of 3 ps and 25 ps using time resolved Raman spectroscopy (Mizutani and Kitagawa 1997). The molecular mechanism of heme cooling in CO bound myoglobin was addressed previously by the Straub group using a computational approach (Y. Zhang, Fujisaki, and Straub 2007). The authors proposed that the heme cooling occurs through three possible mechanisms: i) energy transfer through hydrogen bonds between the heme group and surrounding protein/solvent, which represents the main deactivation path, ii) vibration–vibration energy transfer via resonant interactions, and iii) thermal collision processes. The time-constant observed for the initial decay of the signal amplitude (5-10 ps) is in agreement with contribution of the thermal heme relaxation contributed to the observed signal.

On the other hand, significantly larger amplitude for the heme de-excitation observed for hexa-coordinate globins (A_1 ~ 50%) compared to the A_1 ~ 12 % measured for penta-coordinate hhMb and hHb, points towards additional process(es) that contribute to the initial amplitude in the hexa-coordinate globins. In the transient absorption study of

several hexa-coordinate heme proteins, Vos *et al.* have associated the fast picosecond kinetic to the ultrafast formation of the bond between the ferric heme and the axial ligand (Vos 2008). Based on the data presented here, I propose that in case of hNgbWT and hCygbWT, the initial 5- 10 ps phase reflects both processes, the fast thermal relaxation of the photo-excited heme as well as binding of the distal histidine residue on the picosecond timescale. This is supported by the fact that the amplitude of the initial phase decreases from 47% in hNgbWT to 11 % in hNgbH64Q and from 59% to hCygbWT to 8% hCygbH81Q, resulting in amplitude values that are comparable to those found in Hb and Mb. These results suggest that the closer distance between the distal histidine and heme iron in hexa-coordinate globins (Figure 4.7) facilitates the ultrafast distal histidine rebinding in hNgbWT and hCygbWT. Furthermore, I propose that distal histidine sidechain exists in two distinct conformations in CO-bound hNgbWT and hCygbWT, as shown in Figure 4.8. In Conformation 1, distal histidine sidechain is displaced far from heme iron, thus allowing CO rebinding on ps-ns timescales. On the other hand, distal histidine in Conformation 2 is positioned adjacent to the CO molecule, and upon photolysis of iron-CO bond, replaces CO as the sixth axial ligand within ~10 ps (Figure 4.9).

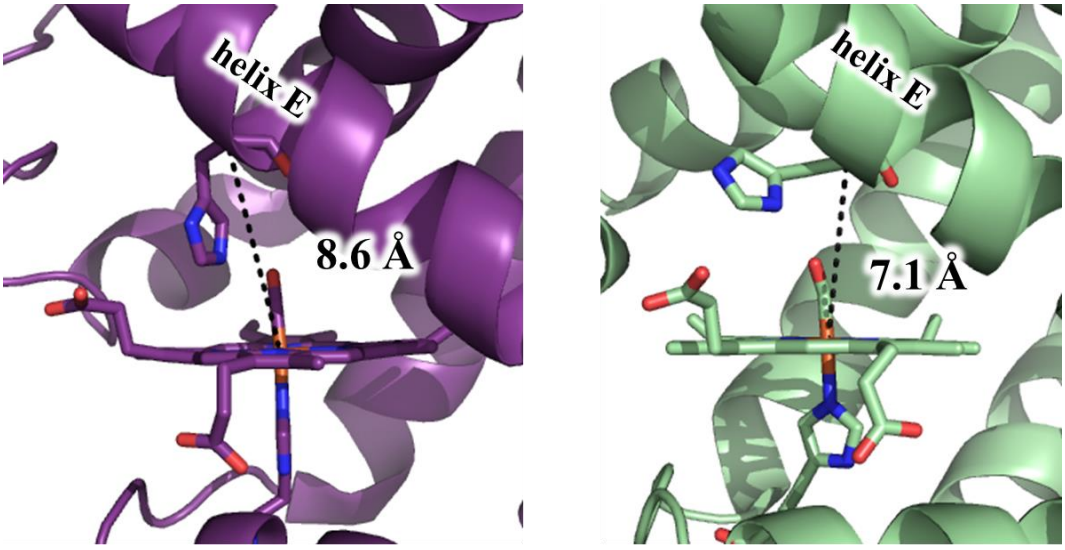

hhMb-CO
PDB: 1DWR

hCygbWT-CO
PDB: 3AG0

Figure 4.7. Crystal structures of CO-bound penta- and hexa-coordinate globins show that the Cα atom of the distal histidine residue is positioned 1.5 Å further from the heme iron in hhMb-CO (Chu et al. 2000) than in hCygbWT-CO (Makino et al. 2011).

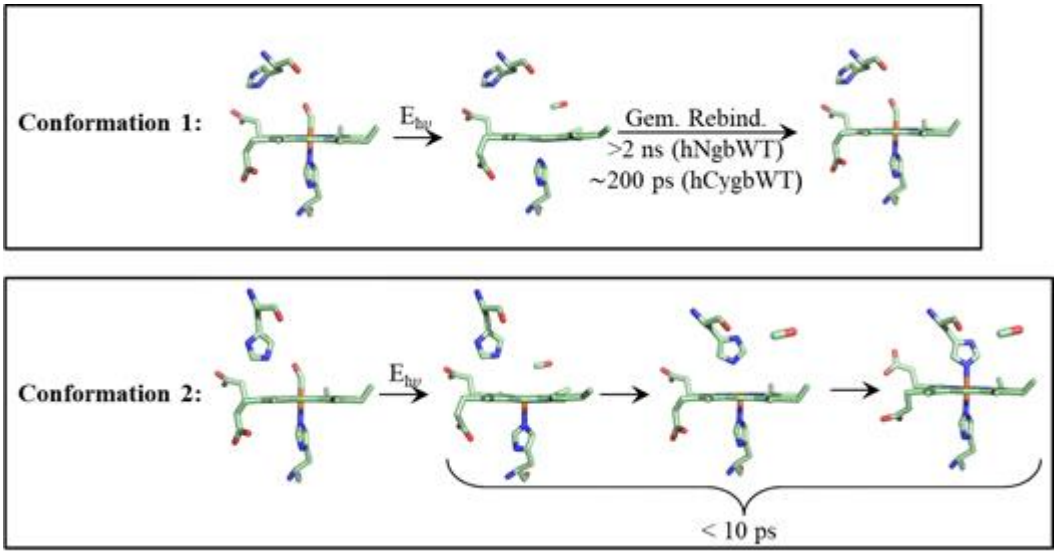

Figure 4.8. Schematic diagram showing proposed mechanism for CO and distal histidine rebinding following photo-cleavage of CO-iron bond in hNgbWT and hCygbWT.

The ultrafast axial ligand rebinding may also be caused by the presence of a highly reactive heme iron in Ngb and Cygb as the bimolecular CO rebinding to the

pentacoordinate heme is two orders of magnitude faster in hexa-coordinate globins compared to Mb or Hb (Astudillo et al., 2012). Interestingly, the time constant associated with the initial phase in the hCygbH81Q mutant is three times faster than in the WT protein, pointing towards a more efficient energy transfer mechanism in this construct. This likely occurs through the modification of the heme distal cavity by the replacement of distal histidine, which leads to stronger hydrogen bonding between the heme propionate groups and nearby residues and/or enhanced contacts between the heme group and surrounding residues.

An additional important aspect of this study is identification of the fast geminate CO rebinding to hCygbWT and hNgbH64Q occurring on the 100 ps timescale. Such fast CO geminate rebinding has not been observed previously for penta-coordinate globins. The fact that fast geminate rebinding is missing in hNgbWT and present in hNgbH64Q, while present in hCygbWT and absent in hCygbH81Q, indicates that the geminate rebinding is facilitated by conformational changes in the distal pocket that result in formation of a temporary binding site for the photo-dissociated CO molecule in close vicinity to heme iron. Such structural changes have to decrease the energy barrier for the photo-dissociated ligand geminate rebinding and/or prevent fast ligand migration further into the protein matrix. Comparable rate constants for geminate CO rebinding were reported previously for the CO sensing protein CooA (Kumazaki et al. 2000), with observed biphasic time constants of 78 ps and 386 ps. Interestingly, the 78 ps phase is similar to the time constant resolved for CO geminate rebinding in hexa-coordinate globins with a reduced disulfide bond. These results suggest that pronounced changes of

the distal pocket in the absence of the disulfide bond facilitates the geminate rebinding in the hexa-coordinate globins. Considering that the precise molecular mechanism of the physiological role of hNgbWT and hCygbWT remains unclear, the presence of the highly reactive heme iron and fast geminate rebinding kinetics analogous to those observed previously for CO-sensing protein CooA suggest that vertebrate hexa-coordinate globins may serve as sensors of diatomic gaseous molecules, under certain physiological conditions which prevent formation of the disulfide bond.

4.4 Summary

Ultrafast kinetics following CO photodissociation from hCygb and hNgb revealed these hexacoordinate globins have a highly reactive heme capable of rebinding internal (distal histidine) or external (CO) ligands on picosecond timescale. Surprisingly, in hCygbWT and hexacoordinate globins lacking the disulfide bond, CO rebinding is three to four orders of magnitude faster than in Mb. The lower barrier for CO rebinding point toward potential role of Ngb and Cygb in CO sensing and signaling.

5. PHOTOPHYSICAL CHARACTERIZATION OF ZINC PROTOPORHYRIN IX-INCORPORATED HEXACOORDINATE HEMOGLOBINS

5.1 Introduction

The discovery of methods for extraction of heme moiety from the globin fold (Fanelli, Antonini, and Caputo 1958; Teale 1959) represents an important milestone in hemoprotein research, as it provided an insight into the role of heme-globin contacts in preservation of protein structure and function. In the absence of the cofactor, apoMb was reported to have a compact tertiary structure similar to holoMb, lacking about 11% of α-helical content attributed to a partially unfolded F helix (Harrison and Blout 1965; Jennings and Wright 1993). Reconstitution of apoMb with the native heme group (FePPIX), yields identical spectral signatures as holoMb (Breslow, 1964; Harrison & Blout, 1965), thus confirming reversibility of the recombination reaction. In addition to FePPIX, other porphyrin-based molecules can embed into the central hydrophobic cavity of the apoMb. Modified protoporphyrins, lacking one or more substituent groups, served as structural probes that allowed pin-pointing contributions of each peripheral side chain to the structure-function coupling between heme and globin scaffold. For example, it was found that absence of heme-7-propionate does not significantly perturb ligand binding to myoglobin (Mb), but affects interaction between proximal histidine (HisF8) and heme iron (Hayashi et al. 2002), whereas heme-6-propionate was found to regulate autoxidation of the heme iron (Hayashi et al. 2002). On the other hand, in the absence of substituent groups, prosthetic macrocycle was observed to freely rotate around HisF8-Fe bond with no significant impact on protein secondary structure, suggesting that even a

loose association of porphyrin with apo-form is sufficient for preservation of the Mb tertiary structure (Neya et al. 2016).

In addition to modifications of heme side chains, globins can also be reconstituted with metal free or metal-substituted porphyrins such as free base porphyrin and Zn protoporphyrin IX (ZnPPIX), respectively. As a closed-shell metal, Zn cannot bind diatomic ligands such as oxygen, and therefore serves as deoxy state analog. (Miyazaki et al. 1999). Replacement of native heme with ZnPPIX also allows fluorescence- and phosphorescence- based protein characterizations, which are otherwise impeded by the quenching mechanism of FePPIX, which decreases the efficiency of intrinsic globin (tryptophan) fluorescence 100-fold (Weber and Teale 1959). Luminescence properties of ZnPPIX have allowed convenient determinations of binding affinity, interaction interface and rates of photoinitiated electron transfer between Hb/Mb and reductase cytochrome *b5* (Liang et al. 2002; Naito et al. 1998). In addition, the nanosecond-to-millisecond timescales of ZnPPIX excited states have been exploited to provide insight into the structural arrangement of electron transport chain components using reconstituted cytochrome *c* (Cyt *c*) (Dixit et al. 1982). Similar approaches can also be applied for characterization of intracellular interaction partners for recently discovered Ngb and Cygb (Fago et al. 2006; X. Li et al. 2016; Yu et al. 2012; J. Zhang et al. 2013). Here, we report photophysical properties of ZnPPIX-reconstituted neuroglobin (Ngb) and cytoglobin (Cygb) and demonstrate applications of reconstituted hexacoordinate globins for biophysical characterizations of protein-protein complexes.

5.2 Results

UV-vis absorption spectroscopy

Steady-state UV-vis absorption spectra of ZnPPIX- and FePPIX- bound hNgbWT and hCygbWT are compared to the control (hhMb) in Figure 5.1. The absorption spectrum of reconstituted hCygbWT shows a Soret band at 428 nm, β band at 553 nm and a heterogeneous α band at 587 nm with a shoulder at 595 nm. On the other hand, incorporation of ZnPPIX into hNgbWT results in an electronic absorption characterized by a Soret band at 425 nm, with β and α bands centered at 552 and 588 nm, respectively. Absorption spectra of the reconstituted protein differ from that of free ZnPPIX, and are comparable to that of hhMb-ZnPPIX (427, 552, 595 nm) and Hb-ZnPPIX (425, 552, 588 nm) (Albani & Alpert, 1987; Leonard, Yonetani, & Callis, 1974).

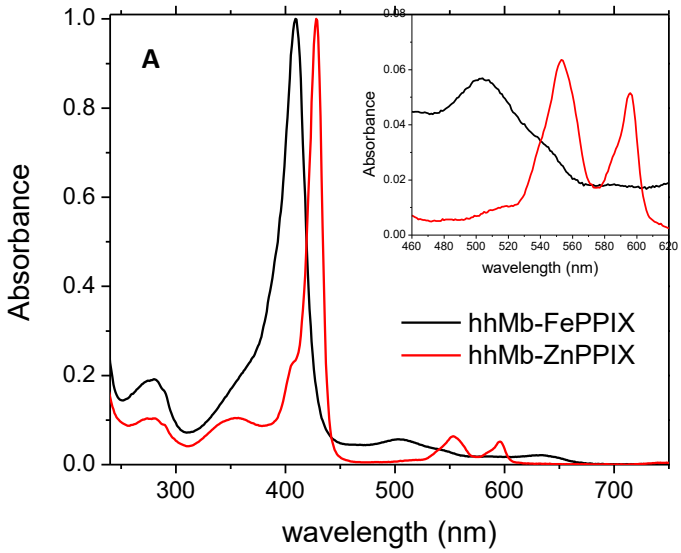

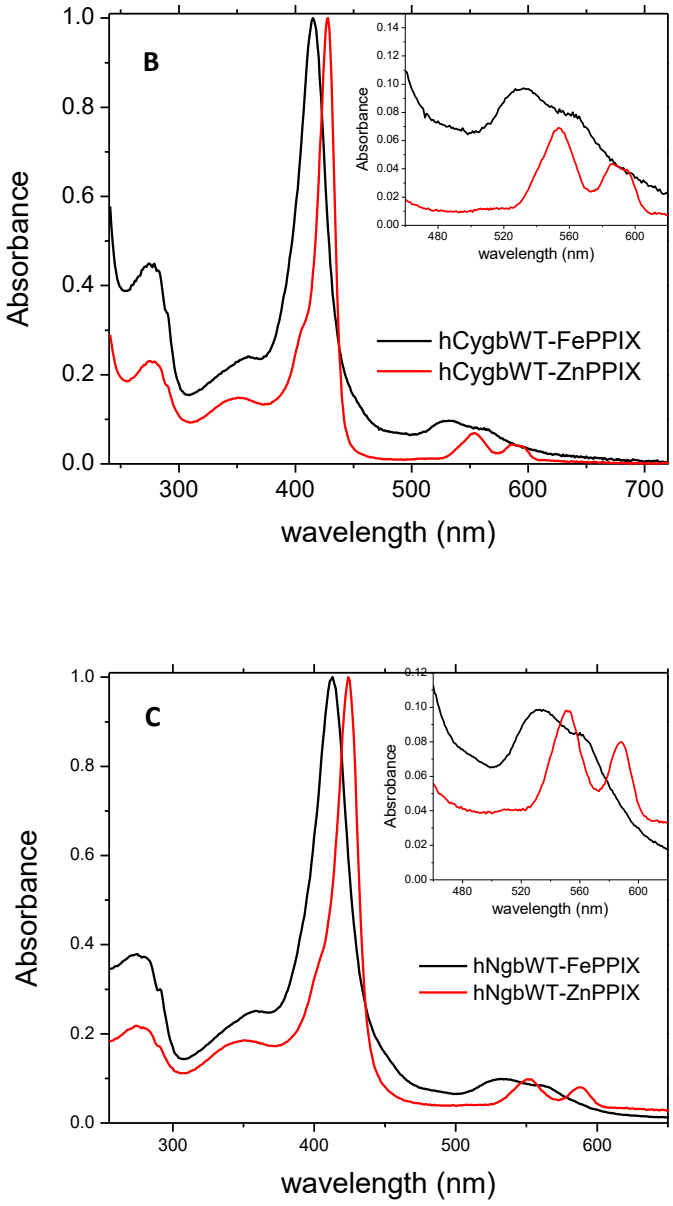

Figure 5.1. Normalized steady-state absorption spectra of (A) hhMb-ZnPPIX (B) hNgbWT-ZnPPIX and (C) hCygbWT-ZnPPIX in 50 mM TrisHCl pH 7.0.

	Soret (nm)	β (nm)	α (nm)
ZnPPIX	412	544	582
hNgbWT-FePPIX	413	532	562
hNgbWT-ZnPPIX	425	552	588
hCygbWT-FePPIX	416	532	562
hCygbWT-ZnPPIX	428	553	587/595
hhMb-FePPIX	408	502	540
hhMb-ZnPPIX	428	554	595

Table 5.1. Summary of UV-vis absorption maxima for hNgbWT, hCygbWT and hhMb with FePPIX and ZnPPIX cofactors. All protein samples were diluted in 50 mM TrisHCl pH 7.0 buffer. ZnPPIX shows monomeric form (A_{Soret}=412 nm) in concentrations below 20 μM.

Steady-state fluorescence emission

Fluorescent properties of the singlet state reveal that, upon excitation at 552 nm, steady-state emission of reconstituted hNgbWT exhibits a narrow peak at 595 nm and a broad band of weaker intensity at 648 nm. In comparison, emission spectrum of ZnPPIX-hCygbWT is slightly red-shifted with peaks at 598 and 650 nm, analogous to the maxima previously reported for hhMb-ZnPPIX (Lepeshkevich et al. 2014).

Fluorescence quantum yield (Φ_F) was not found to be significantly impacted by the hexacoordinate protein matrix (Table 5.2). The results show that Φ_F of reconstituted hCygbWT is 0.008, which is similar to the value reported for hhMb-ZnPPIX (Φ_F= 0.03) and for ZnPPIX in ethanol (Φ_F= 0.033) (J. Feitelson and Barboy 1986).

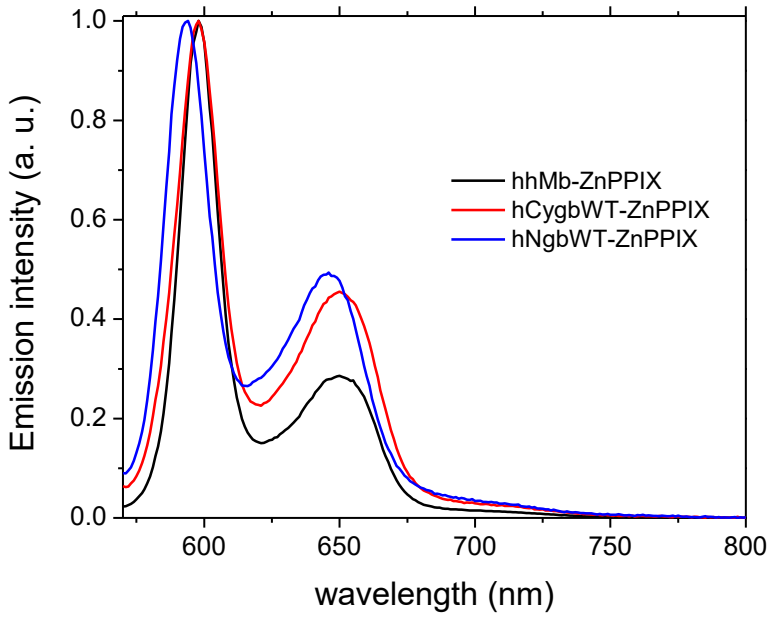

Figure 5.2. Normalized steady-state fluorescence emission spectra of ZnPPIX-reconstituted globins, using λ_{exc}= 552 nm.

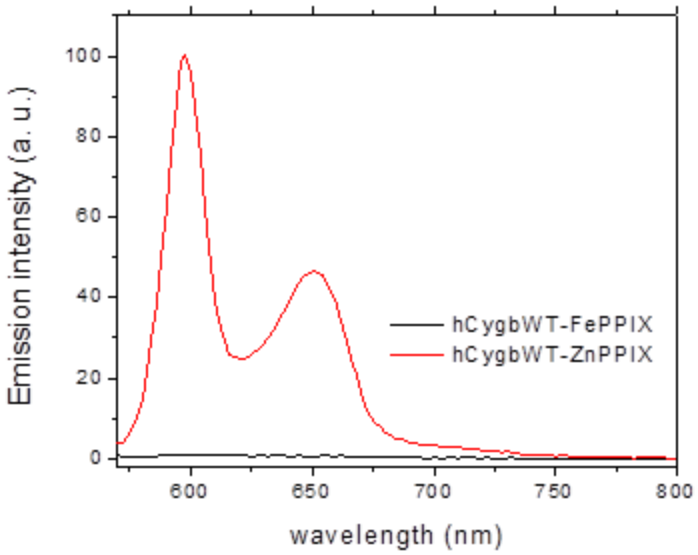

Figure 5.3. Comparison of steady-state fluorescence emission spectra between ZnPPIX- and FePPIX-bound hCygbWT

Fluorescence and phosphorescence lifetimes

Interestingly, the fluorescence lifetime of ZnPPIX within the hexacoordinate globin fold is significantly more heterogeneous then in reconstituted hhMb ($\tau = \sim$ 2.1 ns) (Albani and Alpert 1987), as shown in Table 5.2. Specifically, decay of the excited singlet state was determined to be biphasic ($\tau_1 = \sim$ 1 ns, $\tau_2 = \sim$ 2.5 ns) for both hCygbWT-ZnPPIX and hNgbWT-ZnPPIX. Pre-exponential factors (α_1, α_2) associated with the fluorescence lifetimes reveal that ZnPPIX is found in two distinct environments, with 61:39 and 71:29 fractional distribution of the fluorophore within the reconstituted hCygbWT and hNgbWT, respectively.

In addition, the decay lifetime of the excited triplet state (τ_P) was determined (Figure 5.4). Phosphorescence lifetimes obtained for hCygbWT-ZnPPIX (τ_P =8.7 ± 0.5 ms) and hNgbWT-ZnPPIX (τ_P =14.0 ± 0.2 ms) are similar to the decay lifetimes previously reported for ZnPPIX-hhMb ($\tau_P \sim$14 ms) (Zemel and Hoffman 1981).

	hNgbWT-ZnPPIX	hCygbWT-ZnPPIX
λmax (emi)	595	598
λmax (emi)	648	650
τ_1 (ns)	0.76	1.3
α_1	0.71	0.61
f_1	0.44	0.45
τ_2 (ns)	2.38	2.53
α_2	0.29	0.39
f_2	0.56	0.55
Φ_F	n. d.	0.008
τ_P (ms)	14.0 ± 0.2	8.7 ± 0.5

Table 5.2. Summary of fluorescence and phosphorescence parameters of ZnPPIX-reconstituted hexacoordinate globins

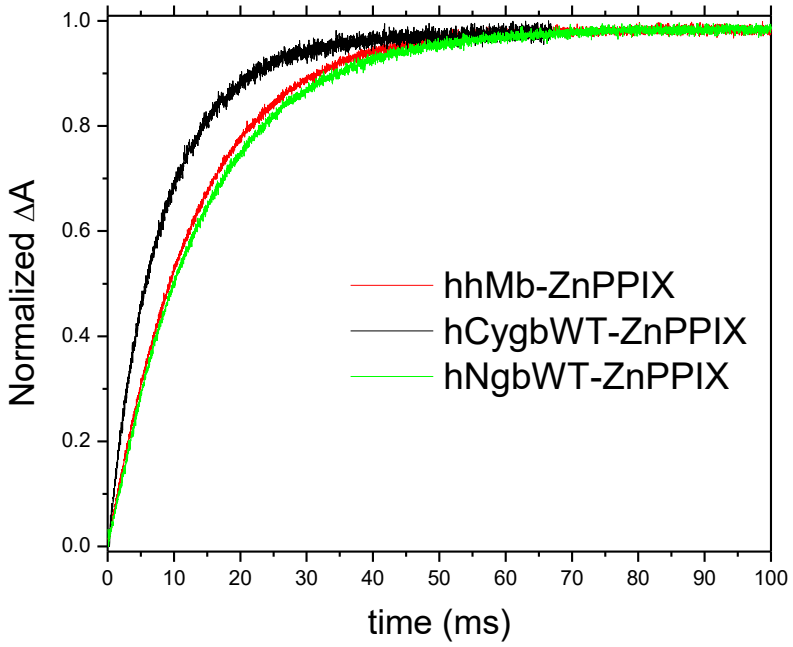

Figure 5.4. Phosphorescence decay determined for reconstituted hhMb, hCygbWT and hNgbWT. Optical density of all samples at excitation wavelength (λ_{exc}= 552 nm) was ~ 0.04. Phosphorescence decay was monitored at 447 nm.

Applications

Fago *et al*. were first to report that human Ngb forms a complex with Cyt *c* (Fago et al. 2006). Here, I demonstrate the application of ZnPPIX-reconstituted Ngb by utilizing its fluorescence properties in order to determine binding constants with the intracellular partner. Titration of ferric Cyt *c* into the solution containing hNgbWT-ZnPPIX induced a decrease in the fluorescence emission intensity. The loss of fluorescence signal can be attributed to quenching/energy transfer between ZnPPIX and *c*-type heme upon association of Cyt *c*. The fraction of hNgb with bound Cyt c was calculated based on hNgbWT-ZnPPIX inner-filter corrected steady-state fluorescence emission intensities in the presence of Cyt *c* and the titration curve is shown in Figure 5.5. The dissociation constant (K_d) was determined to be 6 ± 1 μM, which is in excellent agreement with the previously reported value (10 ± 1 μM) obtained by surface plasmon resonance (Tiwari et al. 2015).

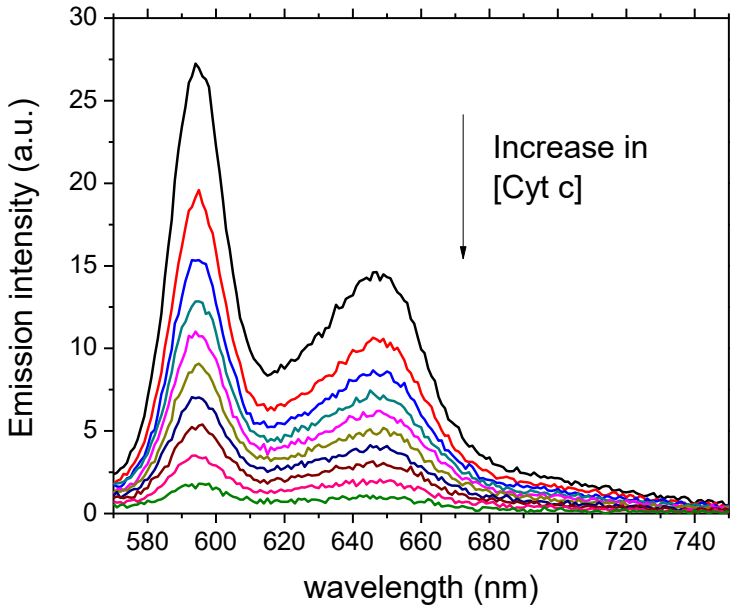

Figure 5.5. Steady-state fluorescence emission spectra (λ_{exc}= 552 nm) for the binding of Cyt c to ZnPPIX-hNgbWT. The emission intensity decreased with higher concentration of Cyt c. No shift in λ_{max} was observed.

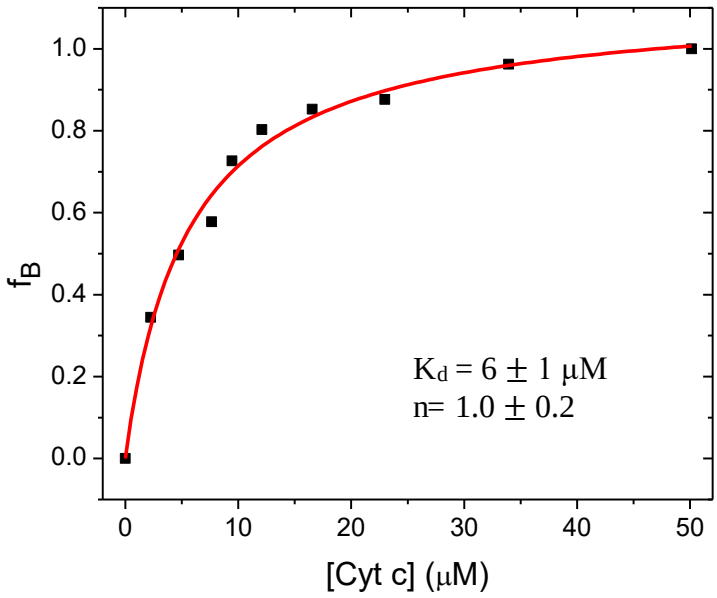

Figure 5.6. Titration curve for Cyt *c* binding to hNgbWT-ZnPPIX. Conditions: 7 μM hNgbWT-ZnPPIX in 10 mM phosphate buffer, pH 7.0.

5.3 Discussion

Incorporation of a metal-substituted protoporphyrin into the heme-binding protein matrix is an established practice that allows exploitation of fluorescence techniques in characterization of conformational changes upon ligand association (Miyazaki et al. 1999), as well as determination of ligand binding constants (Hui et al. 2004; Naito et al. 1998), protein-protein interfaces (Naito et al. 1998) and long-range electron transfer mechanisms (Gingrich et al. 1987).

In contrast to alternative approaches, including covalent attachment of fluorescent dyes to surface residues, ZnPPIX incorporation into the central globin cavity minimizes perturbation of the protein fold, as demonstrated by crystallographic data available on ZnPPIX- and FePPIX-bound Mb (Figure 5.7). It should be noted that fluorescent conjugation using Cys-reactive dyes such as IAEDANS should be avoided in Cygb and

Ngb, as cysteine residues have a structural (Morozov et al. 2014) and functional (Hamdane et al. 2003) role in these proteins.

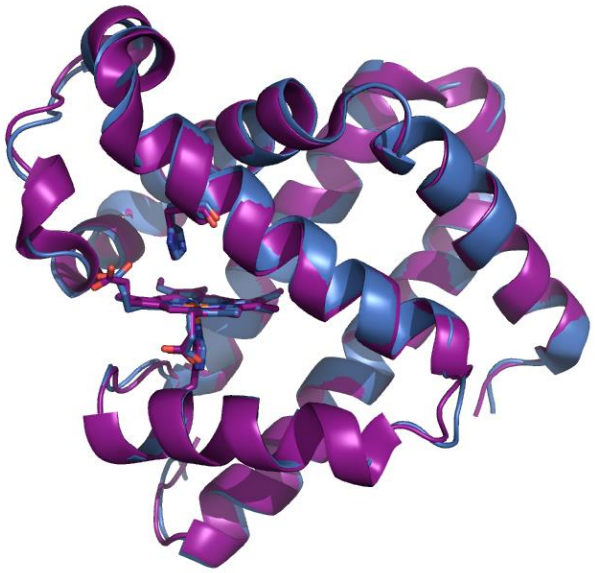

Figure 5.7. Overlay of crystal structures of sperm whale myoglobin with native prosthetic group (purple; PDB entry 1VXA) and ZnPPIX (blue; PDB entry 4MXL). RMSD of backbone atoms is 0.79 Å, indicating minimal perturbation of the tertiary structure upon reconstitution of Mb with ZnPPIX. Prosthetic group, distal and proximal histidine are shown in stick representation. (Chakraborty et al. 2014; Yang and Phillips 1996)

Steady-state absorption and fluorescence emission of the ZnPPIX-reconstituted proteins provide qualitative information about the heme binding site, as spectra undergo a hypsochromic shift with an increase in polarity (Leonard, Yonetani, and Callis 1974). Therefore, analogous absorption spectra of reconstituted Hb, previously reported by Leonard *et al.*, and hNgbWT, which are blue shifted compared to Mb and hCygbWT, indicate distinct modes of ZnPPIX solvation in these globins (Leonard, Yonetani, and Callis 1974). Analysis of aligned sequences (Figure 5.8) and crystal structures reveal a mismatch in heme-interacting amino acid located at the FG loop, which is hydrophobic in Ngb (Val100), Hb α (Leu91) and Hb β (Leu96) chains, but polar in Cygb (His117) and

Mb (His97). It is well established that His97 in Mb participates in heme- and protein-stabilizing hydrogen bonding network with heme-7-propionate and Ser92 (Lloyd et al. 1996; Shiro et al. 1994; Smerdon et al. 1993). Similar noncovalent interactions are found in the proximal side of Cygb as well, since His117 and Lys116 are located 2.4 Å and 2.6 Å from heme-7-propionate, as seen in PDB entry 1V5H (Figure 5.9) (Sugimoto et al. 2004). In contrast, there is only one potential heme-binding residue on the proximal side of hNgbWT located ~ 4.9 Å from the nearest propionate in the crystal structure, whereas Hb α and β chains lack a hydrogen donor for heme in the F helix/ FG loop region (Figure 5.9). Although hexacoordinate structures are not representative of reconstituted hexacoordinate globins, as ZnPPIX is proposed to be pentacoordinate (Jehuda Feitelson and Spiro 1986; S. Ye et al. 1997), it is not unreasonable to assume that heme contacts in the proximal side will be preserved, as ZnPPIX was observed to bind to proximal histidine residue in several X-ray structures of reconstituted Mb and Hb (Chakraborty et al. 2014; Kavanaugh, Rogers, and Arnone 2005; Koshiyama et al. 2011). Therefore, I postulate that extended non-covalent interactions between heme propionate and F helix and FG loop sidechains replace heme-water interactions, thus preventing solvation of heme and the proximal pocket, resulting in a shift in both absorption and fluorescence emission spectra.

Figure 5.8. Sequence alignment of vertebrate globins. Asterisk (*), colon (:) and period (.) denote conserved, strongly similar and weakly similar residues, respectively. Heme lining residues are highlighted in red, whereas propionate-binding residues mismatched in polarity are highlighted in green.

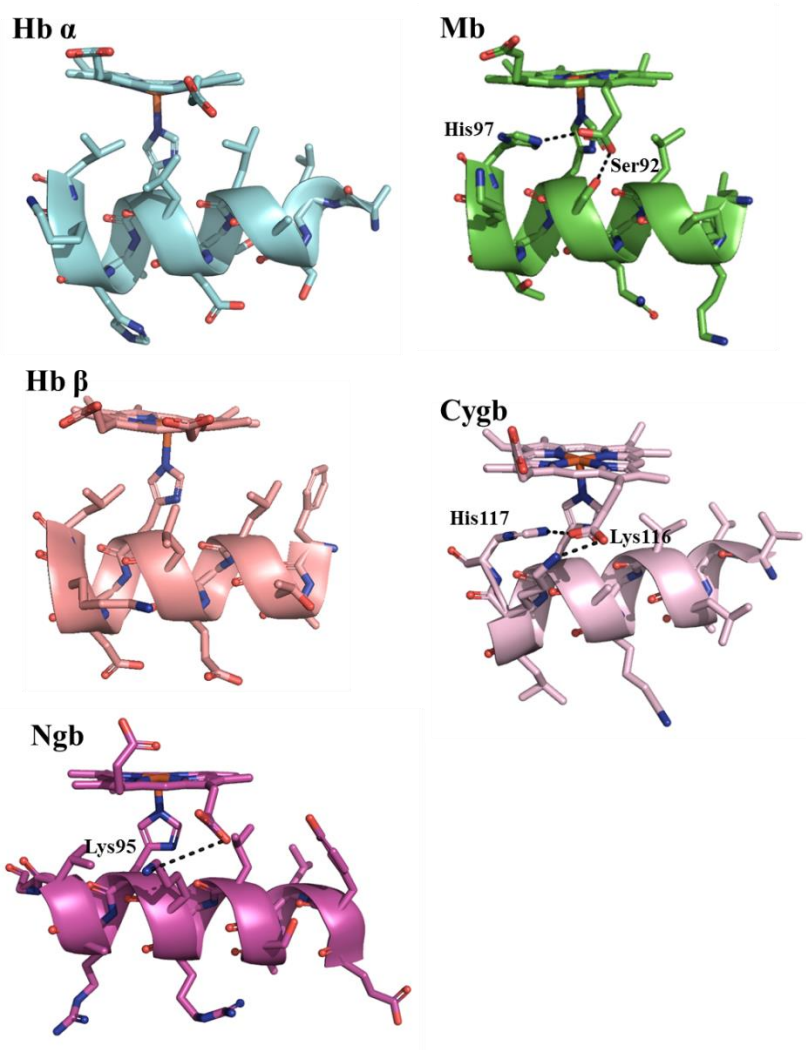

Figure 5.9. Interactions between heme and F helix residues in hhMb (PDB: 1YMB), human Cygb (PDB: 1V5H), human Hb α and β (PDB: 3KMF, chains A and G), Ngb (PDB: 4MPM, chain A) (Evans and Brayer 1990; Guimarães et al. 2014; Kovalevsky et al. 2010; Sugimoto et al. 2004)

Fluorescence lifetimes provide additional information about ZnPPIX incorporation into the hexacoordinate protein matrix. Biphasic decay of the singlet state, together with the pre-exponential values, reveals that ZnPPIX is found in two distinct environments in both Cygb and Ngb. Indeed, heme orientational disorder was observed in human and murine Ngb by NMR and crystallographic studies, in which FePPIX was found to rotate about α-γ-meso axis, shown in Figure 5.10 (Du et al. 2003; Pesce et al.

2003b; Xu, Yin, and Du 2011). In hexacoordinate Ngb, the reported ratio of heme isomers in solution is 2:1, which is comparable with pre-exponential values reported here (71% : 29%). However, there is no experimental evidence for heme orientational heterogeneity in Cygb, as crystal structures currently available show identical heme orientation in all PDB entries. Several explanations exist for interpretation of heterogeneous fluorescence decay in Cygb: (1) in pentacoordinate Cygb, residues lining the heme binding cavity reorganize and remove the kinetic/energetic barrier for ZnPPIX rotation found in hexacoordinate form; (2) Cygb refolds via two distinct pathways, trapping ZnPPIX in different conformations within the protein matrix; (3) ZnPPIX swings between two distinct positions inside the protein matrix, similarly to the heme swinging mechanism observed in CO-bound Ngb (Vallone, Nienhaus, Matthes, et al. 2004). The elucidation of the mechanism responsible for ZnPPIX disorder in Cygb requires additional NMR investigations; however, this is beyond the current scope of the project.

Interestingly, phosphorescence lifetimes and fluorescence quantum yield do not appear to be drastically affected by the hexacoordinate protein matrix, suggesting that the triplet-to-ground state transition is not sensitive to amino acid compositions in the heme-binding cavity. However, faster phosphorescence decay of hCygbWT-ZnPPIX indicates distinct polarity of the heme pocket in those proteins.

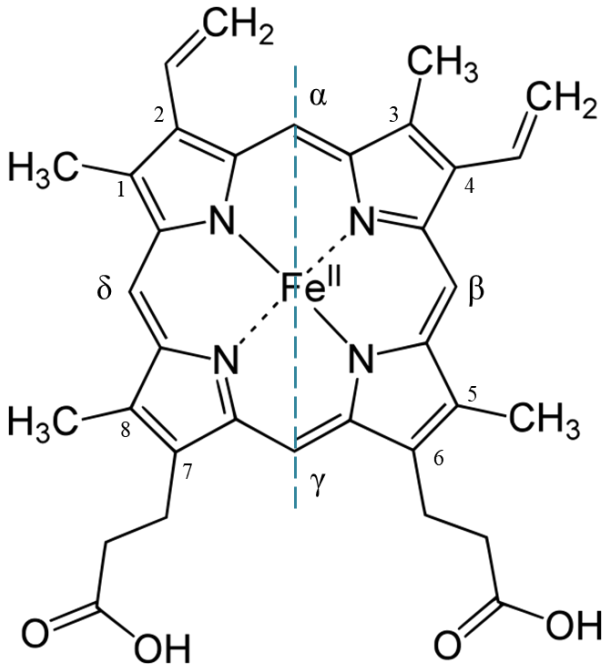

Figure 5.10. Iron protoporphyrin IX can undergo 180° rotation about α-γ meso axis within the globin fold.

Lastly, cytochrome *c*: Ngb anti-apoptotic complex was used to demonstrate how photophysical properties reported here allow facile determination of binding parameters for ZnPPIX-reconstituted globins in their interactions with intracellular partners. It should be noted that in the absence of a quencher in the intracellular partner, fluorescence anisotropy should be employed to elucidate the affinity of the protein-protein complex. Reconstitution approach is time- and cost-efficient, as much smaller concentrations of proteins are needed than in other techniques such as isothermal titration calorimetry, or surface plasmon resonance.

5.4 Summary

In summary, incorporation of zinc protoporphyrin IX (ZnPPIX) into the hexacoordinate globin fold of human Cygb and Ngb resulted in UV-vis absorbance analogous to reconstituted Mb and Hb, respectively. The red-shift of the Ngb absorption spectrum compared to Cygb revealed different solvent accessibility of the cofactor in the respective central hydrophobic cavities. Despite variable solvent exposure, steady-state fluorescent lifetime measurements indicate that ZnPPIX incorporates into the hexacoordinate globin matrix heterogeneously. However, decay of the triplet state is not biphasic, suggesting that phosphorescence properties are not sensitive to the differences in ZnPPIX environment. The data reported here provide a new tool for fluorescence-based characterization of hexacoordinate hemoglobins in the presence and absence of external ligands.

6. THE ROLE OF CYGB TERMINI ON PROTEIN STRUCTURE AND FUNCTION

6.1 Background and significance

Human cytoglobin is structurally distinctive from other vertebrate globins, as 3-over-3 globin core is flanked by ~20 amino acid long extensions on both N- and C- termini. Although full-length structure of a Cygb monomer is yet to be determined, the crystal structure of the disulfide-linked dimer revealed that N-terminal extension forms a short helix, whereas C-terminal fragment is a random coil (Makino et al. 2006). The physiological function of these fragments remains to be determined, however a role in intracellular interactions has been proposed.

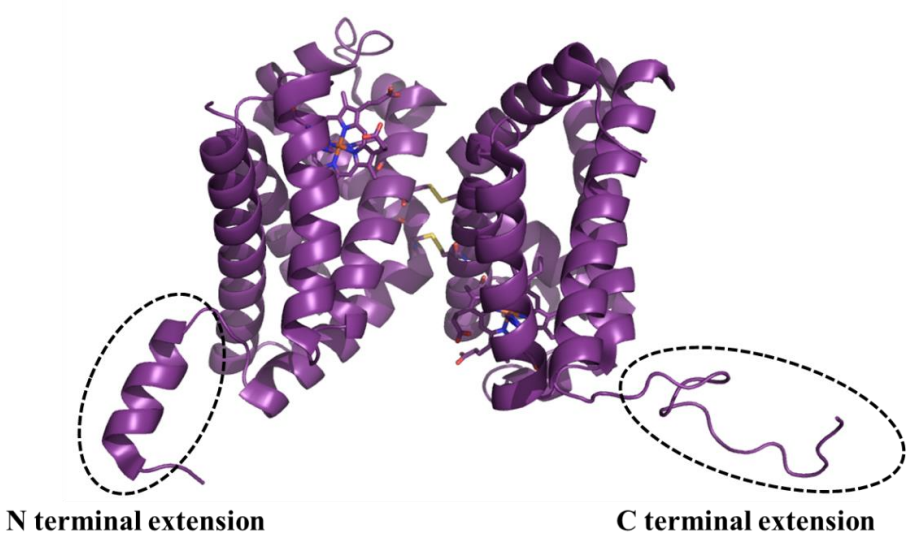

Figure 6.1. Three dimensional structure of disulfide-linked Cygb dimer (PDB entry 2DC3) (Makino et al. 2006). Cygb monomers are connected by two intermolecular bridges formed by Cys38 and Cys83 residues on the opposite polypeptides.

Although other vertebrate globins (Mb, Hb, Ngb) lack terminal extensions, similar appendages have been observed in several bacterial globins, including truncated

hemoglobins from *M. tuberculosis* (Savard et al. 2011), *A. thaliana* (Mukhi et al. 2016), and *M. infernorum* (Jamil et al. 2014), as well as in protoglobin from *M. acetivorans* (Ciaccio et al. 2013). Interestingly, crystal structure of truncated hemoglobin from *A. thaliana* (AHb3) exhibits identical secondary structure of terminal fragments as observed in Cygb (Mukhi et al. 2016; Reeder and Hough 2014). The impact of terminal extensions on structure and function of AHb3 was recently characterized and revealed that N terminal helix has a role in protein dimerization, regulation of internal cavities and NO detoxification, whereas disordered C terminal impacts ligand interactions (Mukhi et al., 2016). In comparison, structural/functional roles of Cygb termini remain largely unexplored. In this study, human Cygb constructs lacking one or both termini were expressed, purified and characterized in terms of impact of terminal extensions on protein structure and stability, as well as the role of termini on lipid and diatomic ligand binding. Furthermore, since interfaces between intracellular partners are often hydrophobic (Keskin et al. 2008; Young, Jernigan, and Covell 1994), contribution of terminal segments to surface hydrophobicity of human Cygb was probed by an extrinsic fluorophore 1,8-ANS,.

6.2 Results

Secondary structure and protein stability

The impact of terminal extensions on secondary structure and stability of human Cygb was investigated using recombinant human Cygb (hCygbWT) with truncated N-terminal (hCygbΔN), C-terminal (hCygbΔC) and N- and C- termini (hCygbΔNΔC). The recorded CD spectra show that deletion of N terminus in both hCygbΔNΔC and

hCygbΔN constructs reduces overall helical content, as evidenced by decrease in ellipticity at 222 and 208 nm (Figure 6.2). In addition, CD spectra also reveal slight loss of the α-helical content in hCygbΔC compared to hCygbWT. Thermal denaturation of Cygb constructs monitored by change in CD signal at 222 nm (Figure 6.4) revealed that deletion of N terminal results in decrease of melting temperature (T_m) and melting enthalpy (ΔH_m) by ~12 °C and ~16.9 kcal/mol, respectively (Table 6.1). The observed ΔH_m = 63 kcal/mol for hCygbWT is in excellent agreement with previously reported value of 60 kcal/mol (Hamdane et al. 2005). Furthermore, impact of termini extensions on protein stability was probed by acid-induced unfolding, which was monitored by steady-state fluorescence emission of Trp residues (λ_{exc}=280 nm) in pH range from 2.4-7.2. As seen in Figure 6.5, the unfolding curves are comparable among all four constructs studied and are not significantly impacted by terminal deletions.

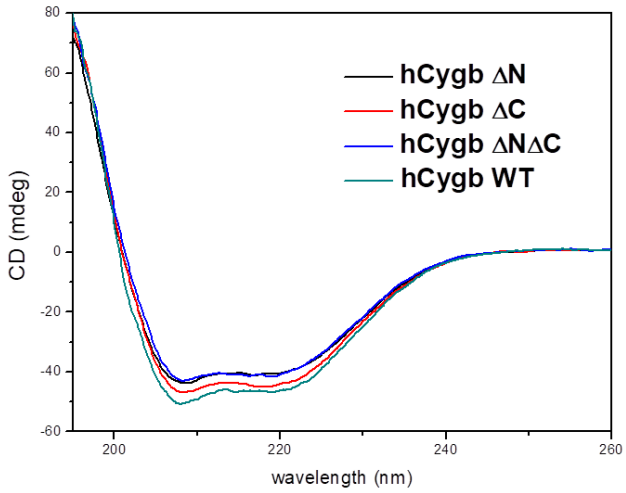

Figure 6.2. Far UV CD spectra of hCygb constructs. Spectra were recorded using 30 µM protein in 50mM TrisHCl pH 7.0 and a cell path of 1 mm.

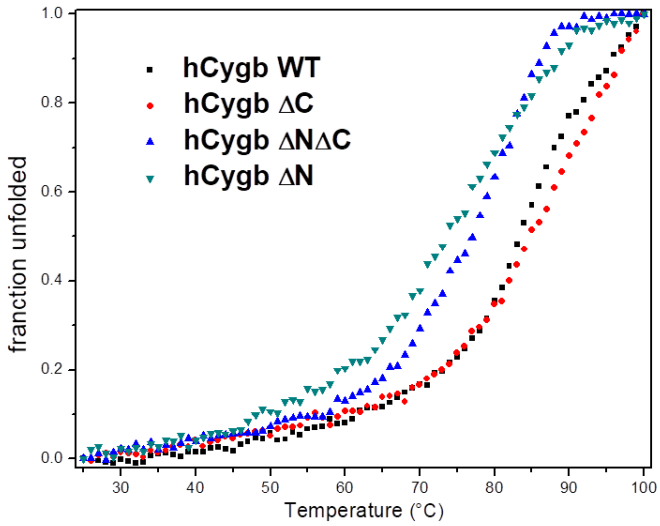

Figure 6.3. Far UV CD signal at 222 nm was used to monitor thermal unfolding using a cuvette with 1 mm path length placed in a thermostated cell holder with a heating rate of 1˚C/min. Conditions: 20 µM protein, 50 mM TrisHCl 200 mM GuHCl pH 7.0.

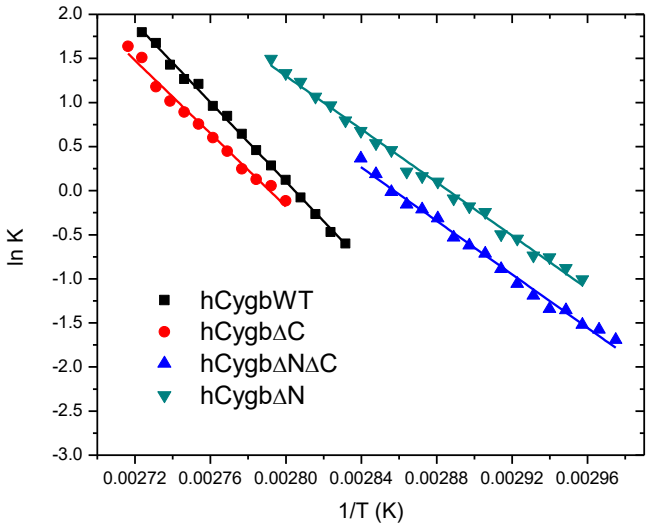

Figure 6.4. Van't Hoff plot for thermal denaturation studies of Cygb constructs. Data were analyzed following the previously published protocol (Greenfield 2006).

	T_m (°C)	ΔH_m (kcal/mol)
hCygb WT	83	63.0
hCygb ΔC	85	57.8
hCygb ΔN	71	43.3
hCygb ΔNΔC	74	43.6

Table 6.1. Thermodynamic parameters derived from thermally induced unfolding curves of hCygb constructs. Melting enthalpy (ΔH_m) was extracted from the slope of the Van't Hoff plots, whereas the first derivative of the denaturation curve was used to determine melting temperature (T_m).

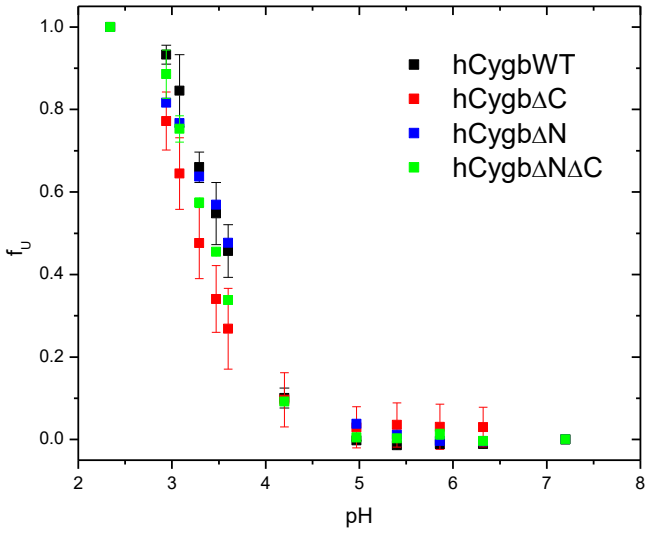

Figure 6.5. Acid-unfolding of Cygb constructs was monitored by steady-state fluorescence emission of Trp residues (λ_{exc}).

Diatomic ligand binding

The impact of terminal extensions on the rate of ligand binding to bis-histidyl heme was determined by rapid mixing of excess KCN to Cygb constructs. As shown in Table 6.2, kinetics for CN^- binding fit to three-exponential decay, which is consistent with the data reported for hCygbWT (Tsujino et al. 2014).

	τ_1 (s^{-1}) (A_1)	τ_2 (s^{-1}) (A_2)	τ_3 (s^{-1}) (A_3)
hCygbWT	1.0 ± 0.5 (28 ± 24%)	11.3 ± 2.2 (34 ± 1%)	55.9 ± 9.2 (38 ± 1%)
hCygbΔC	1.2 ± 0.1 (86 ± 33%)	8.1 ± 0.4 (8 ± 10%)	55.4 ± 5.7 (6 ± 3%)
hCygbΔN	1.6 ± 0.1 (63 ± 18%)	11.0 ± 0.8 (23 ± 3%)	72.4 ± 8.1 (14 ± 2%)
hCygbΔNΔC	1.8 ± 0.2 (44 ± 26%)	11.6 ± 1.3 (37 ± 16%)	63.2 ± 16.5 (19 ± 15%)

Table 6.2. Time constants (τ_1, τ_2, τ_3) extracted from exponential decay fits for Cygb-CN^- complex formation. The amplitudes (A_1, A_2, A_3) for the corresponding time constants are reported in parentheses as percentages. Conditions: 10 μM protein was mixed with 10 mM KCN using a stopped-flow apparatus. Buffer: 50 mM TrisHCl pH 7.0. Complex formation was monitored by changes in absorbance at 417 nm.

Lipid binding

Reeder *et al.* were the first to report that lipids such as oleic acid bind to hCygbWT, and raised a question about the potential role of terminal extensions in governing these interactions. The authors reported that lipid binding to full-length Cygb induces a shift in the Soret band absorption from 416 to 413 nm, as well as formation of a new peak at 630 nm (Reeder, Svistunenko, and Wilson 2011). Identical spectral changes in the absorption of lipid-bound Cygb constructs were observed in this study (Figure 6.6), suggesting that terminal extensions do not play a role in lipid association.

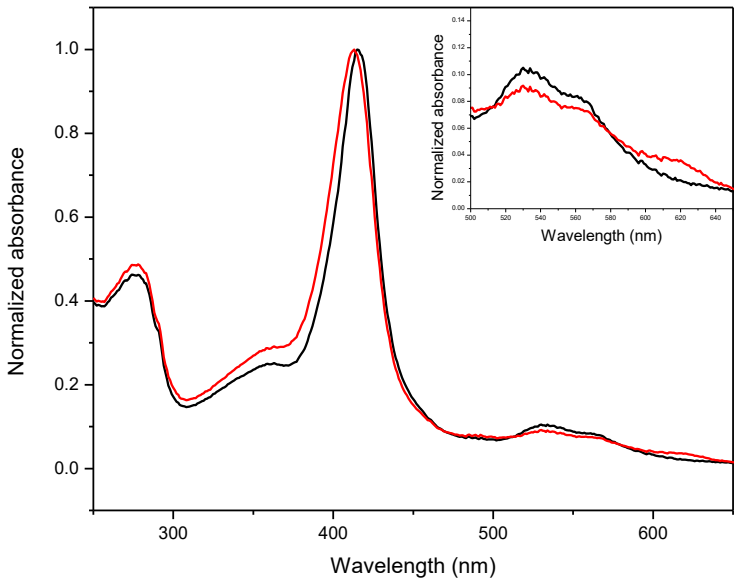

Figure 6.6. Representative UV-vis spectra for lipid biding to Cygb constructs for ferric Cygb (black) and Cygb:sodium oleate complex (red) are shown.

1,8-ANS interaction with Cygb

Surface hydrophobicity in Cygb was characterized by binding of extrinsic fluorophore 1,8-ANS, which upon docking to an apolar environment exhibits an increase in the intensity of fluorescence emission and a shift in λ_{max} to the shorter wavelengths. Figure 6.7. shows a modest, four-fold increase in emission intensity of 1,8-ANS: CygbWT complex compared to that of free fluorophore, accompanied by 49 nm blue-shift of the emission maximum (λ_{max}= 471 nm). Surprisingly, emission intensity further increases and shifts (λ_{max}= 467 nm) upon rupture of Cys38-Cys83 bridge (hCygbWT^{red}, Figure 6.7), indicating that disulfide bond regulates accessibility and hydrophobicity of the 1,8-ANS binding site. As evident from Figure 6.8, similar 1,8-ANS binding sites do not exist in other vertebrate globins such as horse heart Mb (hhMb), human Hb (hHb), and wild-type human Ngb (hNgbWT). Steady-state emission of Cygb constructs in the

absence of the disulfide bond suggest that N terminal contributes to the formation of 1,8-ANS binding site, as deletion of this fragment leads to a ~2-fold decrease in intensity of 1,8-ANS: hCygbΔN^{red} and 1,8-ANS: hCygbΔNΔC^{red} complexes (Figure 6.9).

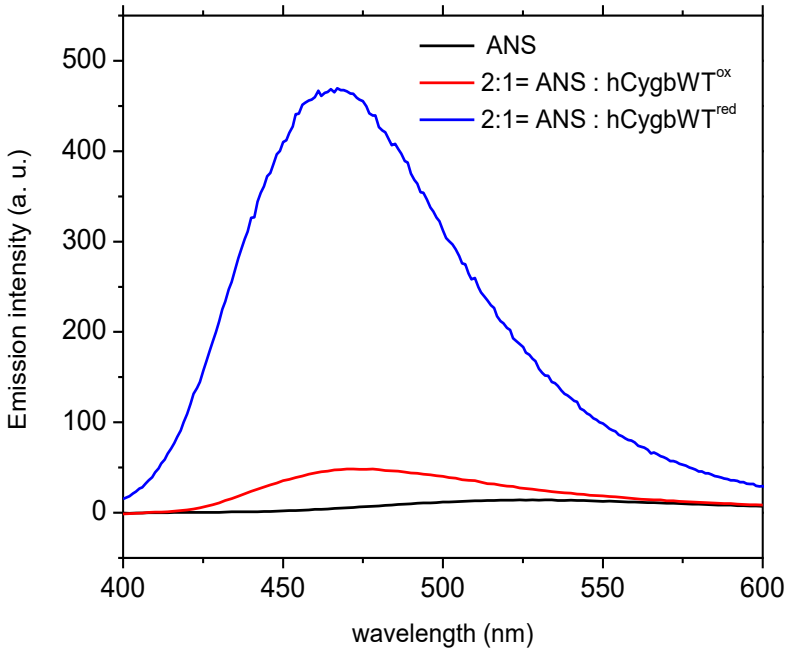

Figure 6.7. Steady-state fluorescence emission (λ_{exc}= 350 nm) of ANS in complex with Cygb in the presence (red) and absence (blue) of the disulfide bond shows approximately 4- and 36-fold increase in the emission intensity at the λ_{max}, respectively.

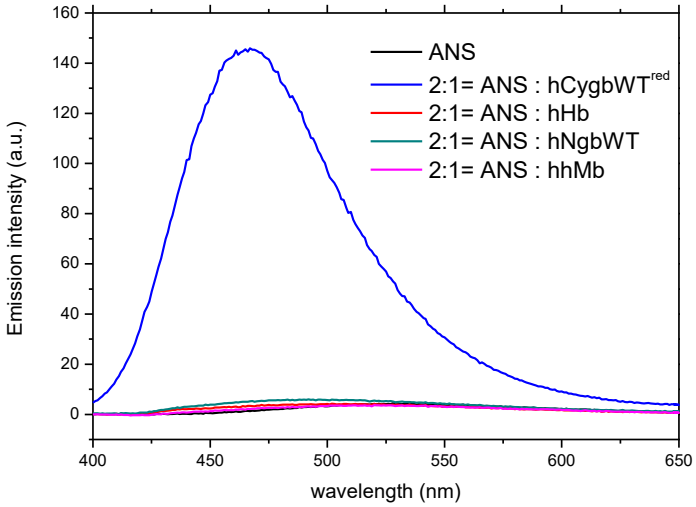

Figure 6.8. Steady-state fluorescence emission (λ_{exc}= 350 nm) of ANS in complex with Cygb without the disulfide bond (blue), human Hb (red), human Ngb (cyan) and horse heart Mb (pink). All samples were contained 5 µM of protein and 10 µM of 1,8-ANS. Buffer: 50 mM TrisHCl pH 7.0.

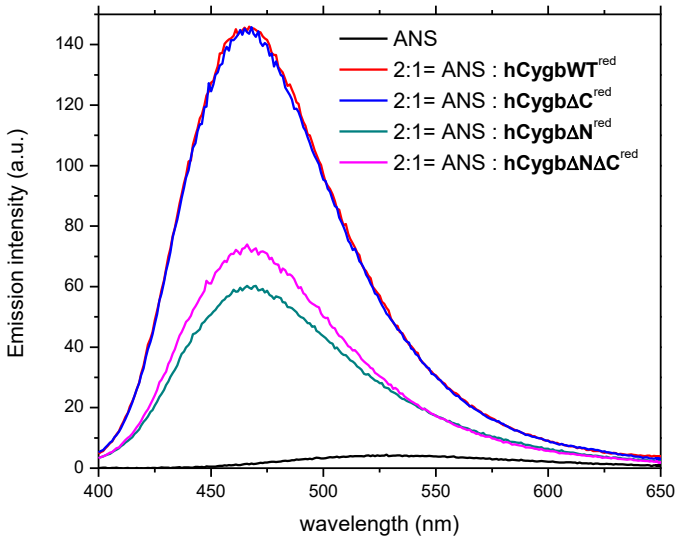

Figure 6.9. The impact of terminal extensions on steady-state fluorescence emission (λ_{exc}= 350 nm) of 1,8-ANS in complex with different Cygb constructs. All samples were prepared with 50 mM TrisHCl.

Molecular dynamics and docking

To pin-point the location of the 1,8-ANS binding site, as well as dynamics of terminal extensions and their interactions with the globin core, simulations of full length, hexacoordinated Cygb in the presence and absence of the disulfide bond were performed. As shown in the panel A in Figure 6.10., both simulations reached equilibrium in the 100 ns of simulation time. Comparison of per-residue root mean square deviations (RMSDs) of hCygbWT and hCygbWT^{red} simulations do not differ significantly, and only slight discrepancies were observed for the residues belonging to AB (residues 38-41), FG (residues 115-119) and GH (residues 141-146) loops (Figure 6.10.B). Such a minimal perturbation of the globin fold may be because of a relatively short distance between disulfide-forming residues, which are 5.0 and 7.8 Å apart (C_α distances) in the presence and absence of the disulfide bond. Since coordination bond between distal histidine and heme iron restricts the movement of helix E, the formation of the Cys38(B2)-Cys83(E9) link forces AB loop to move towards the "rigid" E helix, leading to a partial unfolding of the N-terminal of the B helix and slight tilting of helices A, G and H (Figure 6.11).

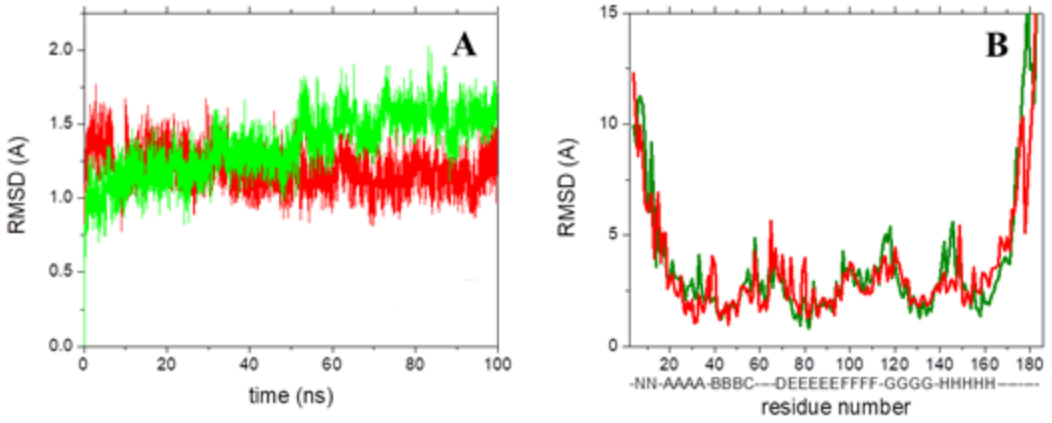

Figure 6.10. (A) Root mean square deviation (RMSD) as a function of time for Cα atoms of residues comprising the globin core (21-169) in hexacoordinate Cygb with (green) and without (red) the disulfide bond. (B) Average RMSD of amino acid residues.

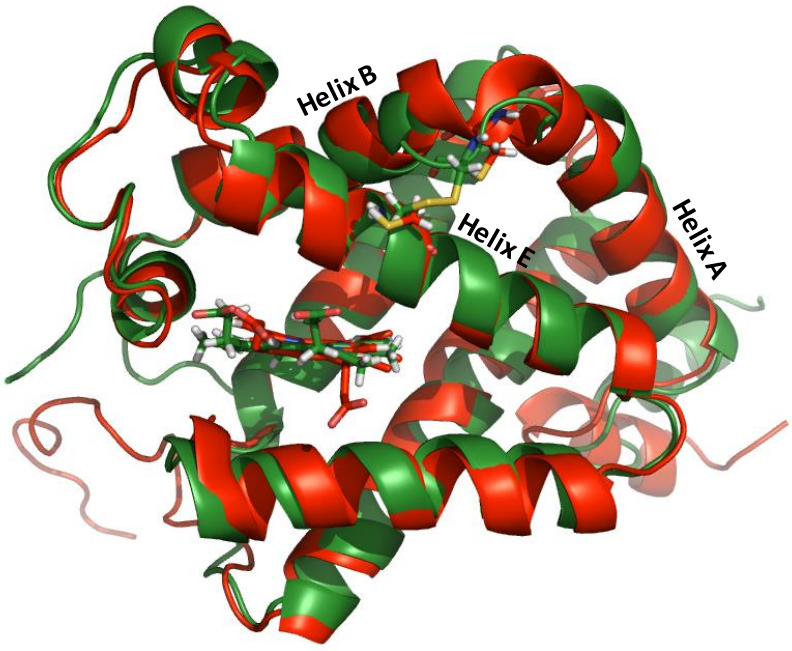

Figure 6.11. Overlay of the representative structures of hexacoordinate human Cygb in the presence (green) and absence (red) of the Cys38-Cys83 disulfide bond.

Terminal extensions dynamics and interaction with globin core

Over the course of both MD simulations, N terminal retained the helical structure, but interacted with globin core only in the presence of Cys38-Cys83 link via hydrogen bonds between Arg149-Glu14, Arg12-Glu146 and Arg13-Glu146. Surprisingly, disulfide bond was found to be coupled to the dynamics of N terminus, which becomes significantly more flexible upon the rupture of the disulfide bond (Figure 6.12). As expected, solvated C terminal extension is not linear and rigid as seen in the crystal structure, despite being a proline-rich fragment. The 20 amino acid segment folds onto itself and even forms a one-turn α-helix (residues 176-180) in hCygbWT. Furthermore, this highly flexible extension was observed to noncovalently interact with globin core in both Cygb simulations, by forming a hydrogen bond with C helix (Ser55-Ala183) and FG loop (Lys118-Ser183).

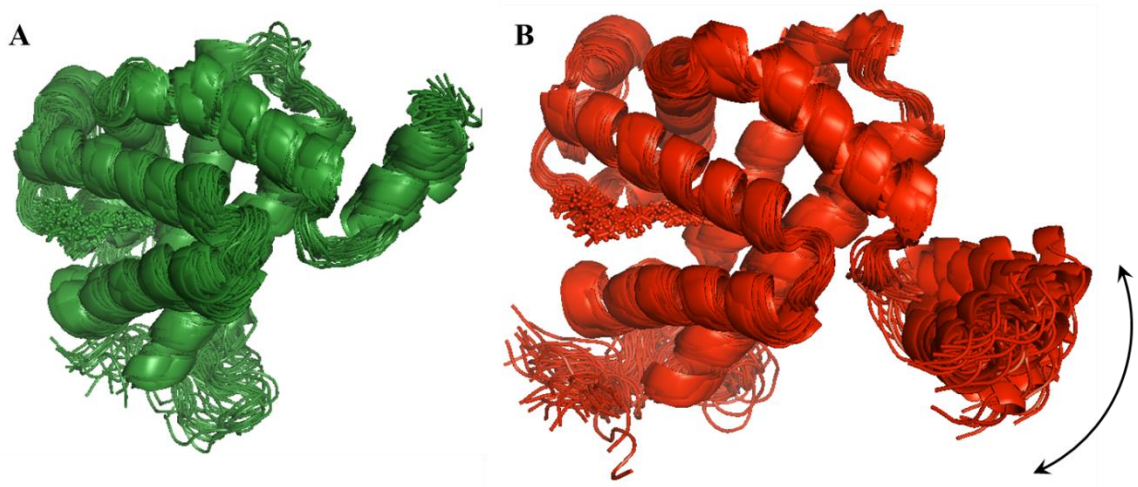

Figure 6.12. Overlay of the 45 snapshots corresponding to last 45 ns of MD simulations in (A) hCygbWT and (B) hCygbWT^{red}, showing enhanced flexibility of N terminal extension upon rupture of the disulfide bond.

hCygbWT^{red}:1,8-ANS complex

Fluorophore docking to hCygbWT^{red} revealed several possible binding sites. However, only the highest scoring complex in which a 1,8-ANS molecule was located near N terminal was selected for further refinement. The resulting docking complex shows 1,8-ANS binding site in the groove formed by N-A and E-F loops (Figure 6.13). Fluorophore binding pocket appears to be formed by extended hydrogen bonding network between Arg24-Glu21, Arg13-Glu18, and Glu18-Arg12 (Figure 6.14). Interestingly, despite the increased flexibility of N terminal in the absence of disulfide bond, the three hydrogen bonding pairs remain in contact over the course of hCygbWT^{red} simulation. Additionally, the fluorophore also interacts with the protein moiety via hydrogen bonding between sulfonic group and Arg12 and Arg13 sidechains, as well as via hydrophobic contact between the naphthalene ring and His97 and Pro99 sidechains (Figure 6.14). On the other hand, MD simulations show that the same binding pocket does not exist in hCygbWT, as formation of the disulfide bond disrupts hydrogen bonding network forming the 1,8-ANS docking site, which is consistent with our experimental data.

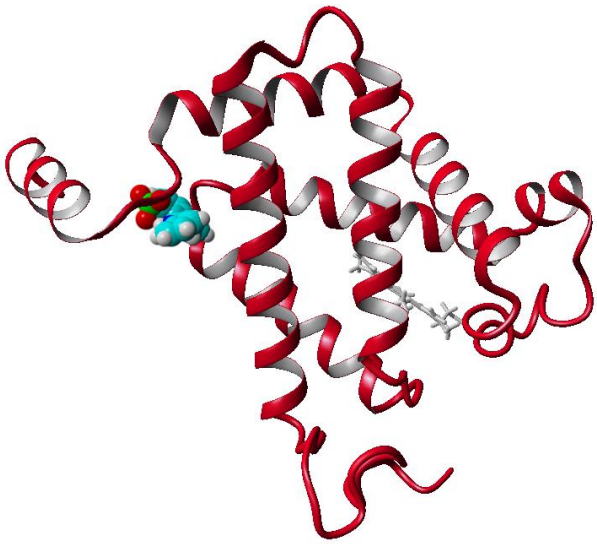

Figure 6.13. Highest scoring docking result of 1,8-ANS: hCygbWT^{red} complex, as generated by YASARA software. Fluorophore is visualized in "ball" representation, whereas heme is shown in stick representation (grey).

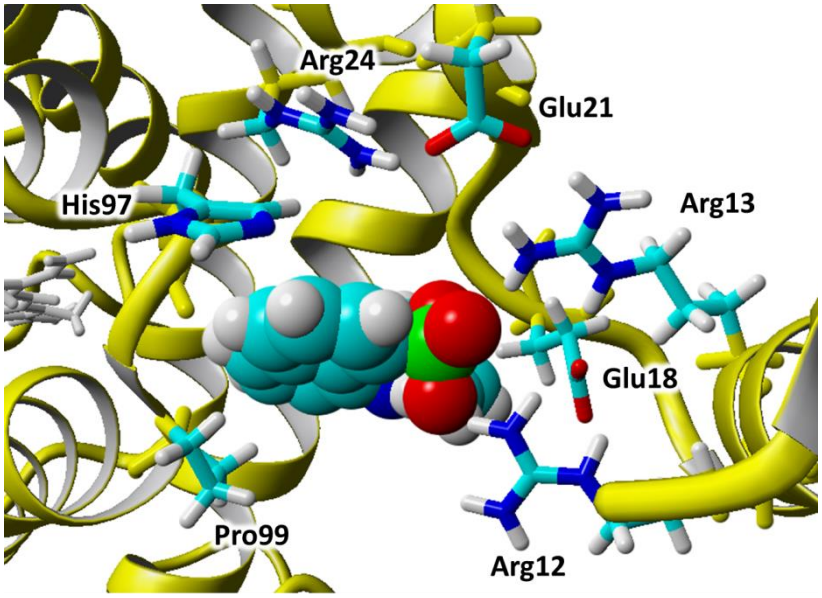

Figure 6.14. Close-up of 1,8-ANS: hCygbWT^{red} binding site. Noncovalent contacts between 1,8-ANS molecule and residues belonging to N terminal and EF loop.

6.3 Discussion

Secondary structure of Cygb termini was determined by steady-state CD spectroscopy, which revealed that N-terminal forms a helical structure in solution, which

is in agreement with the crystal structure (Makino et al. 2006). Experimental data further indicate that C terminal extension may form a short helix, as demonstrated by a small decrease in ellipticity in the CD signal of hCygbΔC compared to hCygbWT. Interestingly, this is consistent with the computational data reported here showing a formation of a one-turn helix in hCygbWT simulation (Figure 6.15). Furthermore, the stability of the Cygb constructs does not appear to be impacted by terminal deletion in acid unfolding studies. However, the constructs lacking N-terminal exhibit lower T_m and ΔH_m values compared to hCygbWT and hCygbΔC. The decrease in melting enthalpy in hCygbΔN and hCygbΔNΔC constructs can be explained by lower energy required to unfold the protein lacking the first 20 residues. Since the enthalpy of helix-to-coil transition was reported to be 1.1 ± 0.2 kcal/mol per residue (Scholtz et al. 1991), N terminal helix should be formed by 13-19 residues to match the experimentally observed difference in ΔH_m= 16.9 kcal/mol. Although only 11 residues form the N terminal helix in the PDB entry 2DC3 (Makino et al. 2006), the first three residues, which may contribute to the helical content, were not resolved.

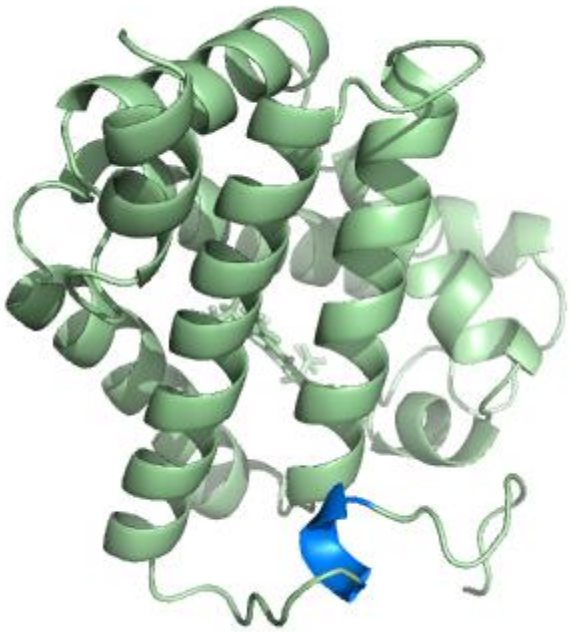

Figure 6.15. Formation of short helix in the C terminal fragment observed in the hCygbWT MD simulation.

Time constants for cyanide binding to hexacoordinate Cygbs are comparable in all four constructs, suggesting a low correlation between termini extensions and modulation of ligand migration pathways and/or the equilibrium of the distal histidine-iron bond. Furthermore, neither N- nor C- termini were found to impact lipid binding to Cygb. These observations are in agreement with several recent reports (Hanai et al. 2018; Tejero et al. 2016) confirming lack of ligand- or lipid-binding modulation by terminal extensions.

Surprisingly, disulfide-dependent 1,8-ANS binding unique to Cygb and absent in other vertebrate globins was observed. Experimental data suggest that N terminal contributes to the formation of the hydrophobic binding pocket, as determined by the decrease of the fluorescence emission intensity in Cygb constructs with reduced disulfide bond (Figure 6.9). These data are explained by docking studies, which predict that the

1,8-ANS binding site is located in the groove formed by loops connecting N-A and E-F helices. The docking complex indicates that fluorophore-protein interaction is stabilized by multiple noncovalent contacts with sulfonic group and naphthalene rings. Futhermore, the hydrophobic pocket was observed to be formed by several hydrogen bonding pairs only in the absence of disulfide bond. Molecular dynamics simulations of hCygbWT indicate that N terminal helix is much more rigid because of several noncovalent interactions with H helix, thus preventing the formation of the 1,8-ANS binding site analogous to the one observed in hCygbWT^{red} simulation. This is in agreement with experimental data (Figure 6.7), which exhibit distinct emission intensities, and therefore different binding sites, in 1,8-ANS:hCygbWT and 1,8-ANS:hCygbWT^{red} complexes. Overall, these data suggest that under reducing conditions, N terminal may mediate intracellular protein-protein interactions of human Cygb.

6.4. SUMMARY

In summary, Cygb termini were not found to regulate diatomic ligand or lipid binding, nor do they have a significant role in protein stabilization. Furthermore, secondary structure reported by X-ray diffraction method is in agreement with the solution data. Computational data suggest that the flexibility of the helical N terminus is regulated by the disulfide bond. In the absence of the Cys-Cys link, 1,8-ANS binding site is more accessible, suggesting that the opening of the hydrophobic pocket is redox-dependent.

7. TYR 44 IS A KEY RESIDUE IN TRANSMITTING STRUCTURAL INFORMATION FROM THE CD LOOP TO THE HEME IRON IN NEUROGLOBIN

7.1 Introduction

Neuroglobin (Ngb) is one of the latest additions to the vertebrate globin family, expressed predominantly in the tissues of brain and retina (Burmester et al. 2000). Since its discovery in early 2000s, numerous studies have shown that Ngb plays a major role in neuronal tissue protection, by reducing β- amyloid induced toxicity (Chen et al. 2012), and by preventing injuries imposed by hypoxic/ischemic conditions (Sun et al. 2001, 2003). Ngb was also proposed to act as an inhibitor in multiple apoptotic pathways, by reducing cytochrome c from ferric to ferrous state (Fago et al. 2006), as well as through inhibition of guanine nucleotide dissociation from α subunit of heterotrimeric G protein (Wakasugi, Nakano, and Morishima 2003). Additionally, Zhang et al. recently demonstrated that Ngb acts as a tumor suppressor in hepatocellular tumor tissues (J. Zhang et al. 2013). Despite the significant neuroprotective roles in physiological and pathological processes, the underlying molecular mechanism of Ngb's protective function remains to be determined.

The tertiary structure of human Ngb (hNgb) is nearly superimposable with myoglobin and exhibits a typical 3-over-3 α-helical globin fold. However, unlike myoglobin, Ngb displays hexa-coordination of the heme iron in its ferric and ferrous states with His96(F8) and His64(E7) serving as proximal and distal ligands, respectively. The distal His64 can be replaced by diatomic ligands including O_2, NO, and CO that

reversibly bind to the heme iron. Competition between the distal histidine and exogenous ligands leads to biphasic ligand binding kinetics with His64 dissociation being the rate-limiting step (Uzan et al. 2004). Overlay of the ligand-free and CO-bound mouse Ngb structures revealed that CO association to the heme iron triggers a structural reorganization characterized by sliding of the heme deeper into the distal cavity, reorientation of F-helix, and modulation of the CD and EF loop mobility (Anselmi et al. 2007; Vallone, Nienhaus, Matthes, et al. 2004). Although such conformational response to exogenous ligand binding is unique among vertebrate globins, it is unclear if the heme sliding mechanism is common among vertebrate Ngbs or unique for mouse Ngb, as an exogenous ligand-bound hNgb structure has not been reported yet.

Another distinct structural feature of human Ngb is the presence of an internal disulfide bond between the CD loop and a short D-helix formed by Cys46(CD5) and Cys55(D5). The contribution of the intramolecular disulfide bond to Ngb's neuroprotective function remains elusive as the bond is not fully conserved among vertebrate neuroglobins, as rodent Ngbs have Cys46(CD5) substituted by Gly. The presence of the disulfide bridge does not increase the protein stability, as hNgb with the reduced thiol groups is more stable than the oxidized protein (Hamdane et al. 2005). On the other hand, removal of the disulfide bond, either by reduction or Cys substitution, decreases the rate of His64 dissociation from heme iron by a factor of 10, resulting in a decrease of hNgb affinity for O_2 (Hamdane et al. 2003). Based on these results, Hamdane and coworkers proposed that the hNgb function may be coupled to the intracellular redox state through the rupture and/or formation of the internal disulfide bond (Hamdane et al. 2003).

Although the CD loop clearly plays an important role in regulating hNgb interactions with diatomic ligands, the molecular mechanism of how structural changes in the CD loop are transmitted to the heme distal pocket to modulate the affinity of the distal histidine is still unresolved. The phenylalanine residue in the B10 position (Phe28) has been proposed to link structural/dynamic changes in the CD loop to the heme distal pocket (Ezhevskaya et al. 2011) and to act as a gate for ligand migration (Lutz et al. 2009). Detailed information about the effect of the CD loop on the organization of the heme pocket was obtained from a crystal structure of wild-type hNgb (hNgb) with the Cys46-Cys55 intramolecular bridge (Guimarães et al. 2014). The X-ray structure shows that despite the presence of the disulfide bond, the CD loop remains flexible and adjacent helices are destabilized as evident from two distinct conformations of subunits A and B resolved in the crystal structure (Figure 7.1). Specifically, helix C is a 4-turn α helix in the subunit A, whereas it forms incomplete 2 helical turns in the subunit B. Furthermore, while residues 52-57 form a short D helix in the subunit B, a random coil conformation is observed instead in the subunit A. Additionally, the rearrangement of the CD loop is accompanied by a displacement of Phe 42 by ~2.8 Å and reorientation of Tyr44 (Figure 7.1), which is either solvent exposed as observed in the subunit A or adjacent to the heme-7-propionate in subunit B. In addition, in the structure of hNgb with absent disulfide bond (PDB: 1OJ6) (Pesce et al. 2003b), Tyr44(CD3) forms a hydrogen bond to the heme propionate groups (in two subunits) or the position of the sidechain is not resolved. Such dynamic property of Tyr44(CD3) suggests that this residue may participate in the transmission of the structural changes between the CD loop and the heme pocket.

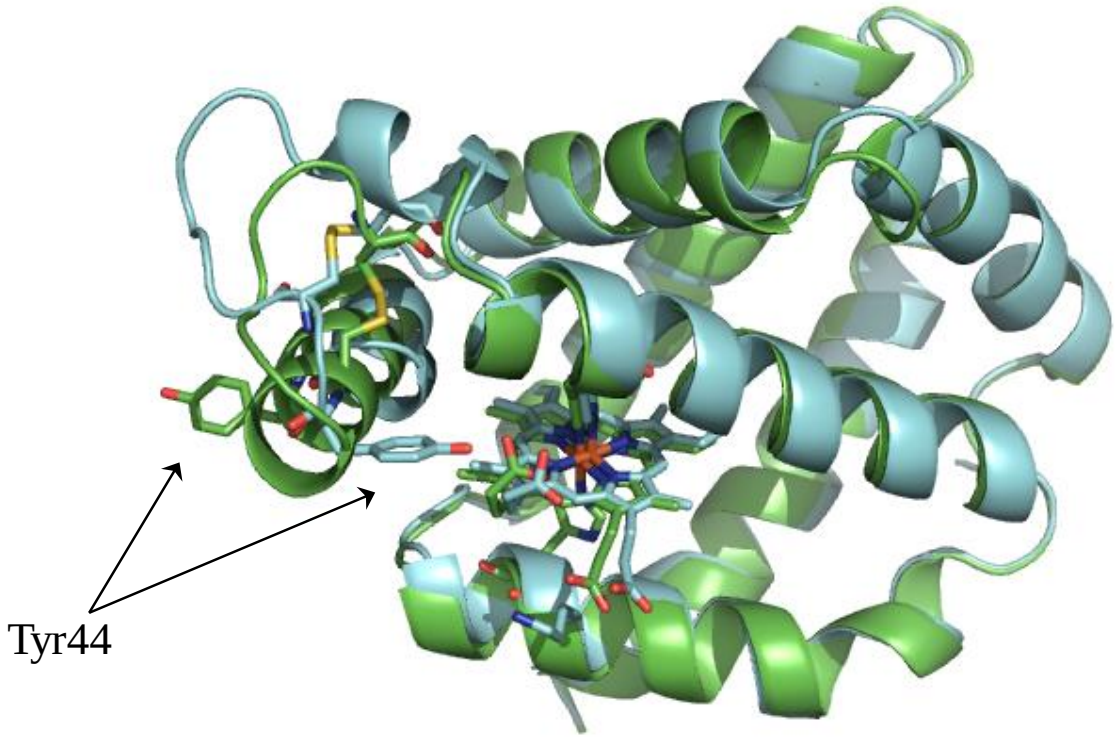

Figure 7.1: Superimposed subunits of human Ngb (PDB entry: 4MPM) showing Tyr44(CD3) in heme propionate adjacent ("in") and solvent exposed ("out") orientations

With this in mind, I investigated the role of Tyr44 in coupling dynamics of the CD loop to the functional properties of hNgb by characterizing hexa- and penta-coordinated hNgb wild-type (hNgbWT) and hNgbTyr44Phe (hNgbY44F) in the presence ($hNgbWT^{ox}$, $hNgbY44F^{ox}$) and absence ($hNgbWT^{red}$, $hNgbY44F^{red}$) of the disulfide bond. The molecular dynamics simulations were performed to complement and explain experimental results obtained in our lab before, published in Luisana Astudillo's PhD thesis (Astudillo 2014).

7.2. Results

Hexacoordinate Ngb- Kinetics

Ligand recombination to ferrous, hexacoordinate Ngb is modulated by the disulfide bond (Hamdane et al. 2003), the oxygen affinity for heme iron is lower by a factor of 10 in hNgbWT^{red} compared to that in hNgbWT^{ox} (Hamdane et al. 2003). Such a decrease in O_2 affinity is a result of slow distal histidine dissociation, which obstructs external ligand binding. Similar disulfide-dependent protein-ligand interaction was observed for cyanide binding to bis-histidyl Ngb in the ferric form (Bocahut et al. 2013). To investigate the role of Tyr44 on coupling CD loop dynamics with ligand kinetics, CN^- rebinding to hNgbY44F^{ox} and hNgbY44F^{red} were measured and compared to those for WT protein. It was found that, in the presence of the Cys46-Cys55 bond, the replacement of the Tyr44 by Phe preserves biphasic kinetics, and reduces the overall rate constant for CN^- association to bis-histidyl protein approximately 2 times. In contrast, cyanide binding was substantially hindered by the rupture of the disulfide bond, which further decreased the observed rates of ligand association by a factor of 10 and 35 in hNgbWT^{red} and hNgbY44F^{red}, respectively (Table 7.1).

	k_{obs1} (x 10^{-2} s^{-1})	A_1 (%)	k_{obs2} (x 10^{-3} s^{-1})	A_2 (%)
hNgb WT^{ox}	2.70	36	4.9	64
$hNgbWT^{red}$	0.90	30	0.61	70
hNgb $Y44F^{ox}$	1.85	26	2.23	74
hNgb $Y44F^{red}$	0.42	29	0.13	71

Table 7.1. Rate constants associated with cyanide binding to hexacoordinate Ngbs. 20 μM ferric protein and 10 mM KCN buffer were mixed using stopped flow, and data was analyzed using multi-exponential decay model. Change of absorbance was monitored at 413 nm.

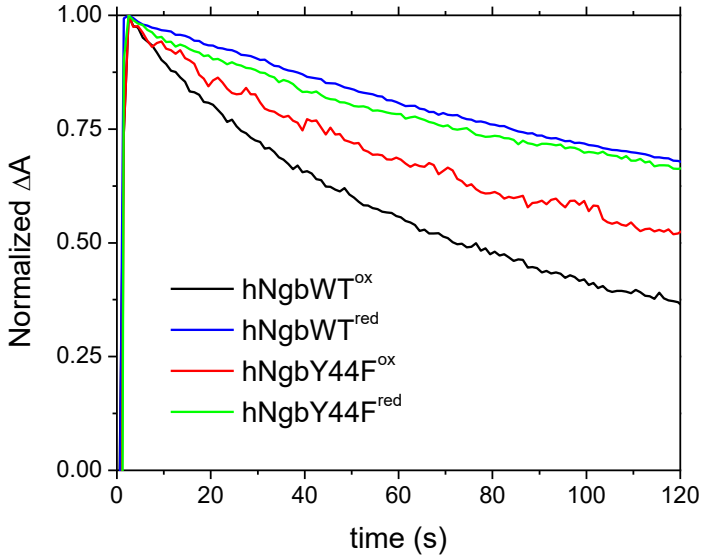

Figure 7.2. Kinetics for CN- binding to ferric, hexacoordinate Ngb constructs.

Molecular dynamics simulations of hexacoordinate Ngb

Tyr44 orientation. Analysis of 50 ns MD simulations reveals that in $hNgbWT^{ox}$, Tyr 44 exists in two orientations, similarly to the positions of Tyr44 sidechain in the crystal structure (PDB entry 4MPM, Figure 7.1). However, extended simulation of $hNgbWT^{ox}$ (200 ns) revealed that Tyr44 in the "out" orientation is the predominant conformation at 300 K. In contrast, residue 44 is almost exclusively solvent exposed in $hNgbWT^{red}$,

hNgbY44F^{ox} and hNgbY44F^{red} simulations, indicating that both the Cys46-Cys55 bond and the Tyr44 hydroxyl group are necessary to promote the "in" conformation.

Heme environment. Simulations of hexa-coordinate hNgbs with and without the disulfide bond revealed that the Cys46-Cys55 bridge impacts (i) orientation of the Phe42 sidechain, (ii) formation of Arg47-Glu60 hydrogen bond, and (iii) formation of a hydrogen bond between Tyr88 and the heme propionate group. Specifically, in the presence of the disulfide bond, the Phe42 sidechain is oriented orthogonal to the heme, whereas it assumes a parallel-to-heme orientation in the absence of the disulfide bond, as shown in Figure 7.3. Oxidation of Cys46 and Cys55 sidechains also promotes a hydrogen bond formation between Arg47 and Glu60, providing a direct link between the CD loop and the E helix, which was not observed in the NgbWT^{red} or NgbY44F^{red}. The Phe42 orthogonal position observed in MD simulations of hNgbWT^{ox} and hNgbY44F^{ox} results in an opening of a short tunnel which is lined with residues Cys46, Asp54, Cys55 and Ser58 (Figure 7.4) and connects the distal cavity with the surrounding solvent. Such increased accessibility of the distal pocket in hNgbWT^{ox} and hNgbY44F^{ox} is supported by a fact that a water molecule can migrate into the distal pocket three to five times more frequently in hNgbWT^{ox} and hNgbY44F^{ox} than in hNgbWT^{red} and hNgbY44F^{red}. Another intriguing impact of the disulfide bond on heme environment is a presence of a hydrogen bond between Tyr88 and heme-6-propionate, which is observed ~60% of simulation time in the protein structures with the disulfide bond, but is absent upon reduction of Cys46 and Cys55 sidechains. The role of the Tyr88 heme hydrogen bond is unclear, as it does not significantly impact flexibility of EF loop or conformational organization of the

proximal side. Also, presence of Tyr88- heme-6-propionate hydrogen bond is unique in Ngb as this residue is not conserved among vertebrate globins.

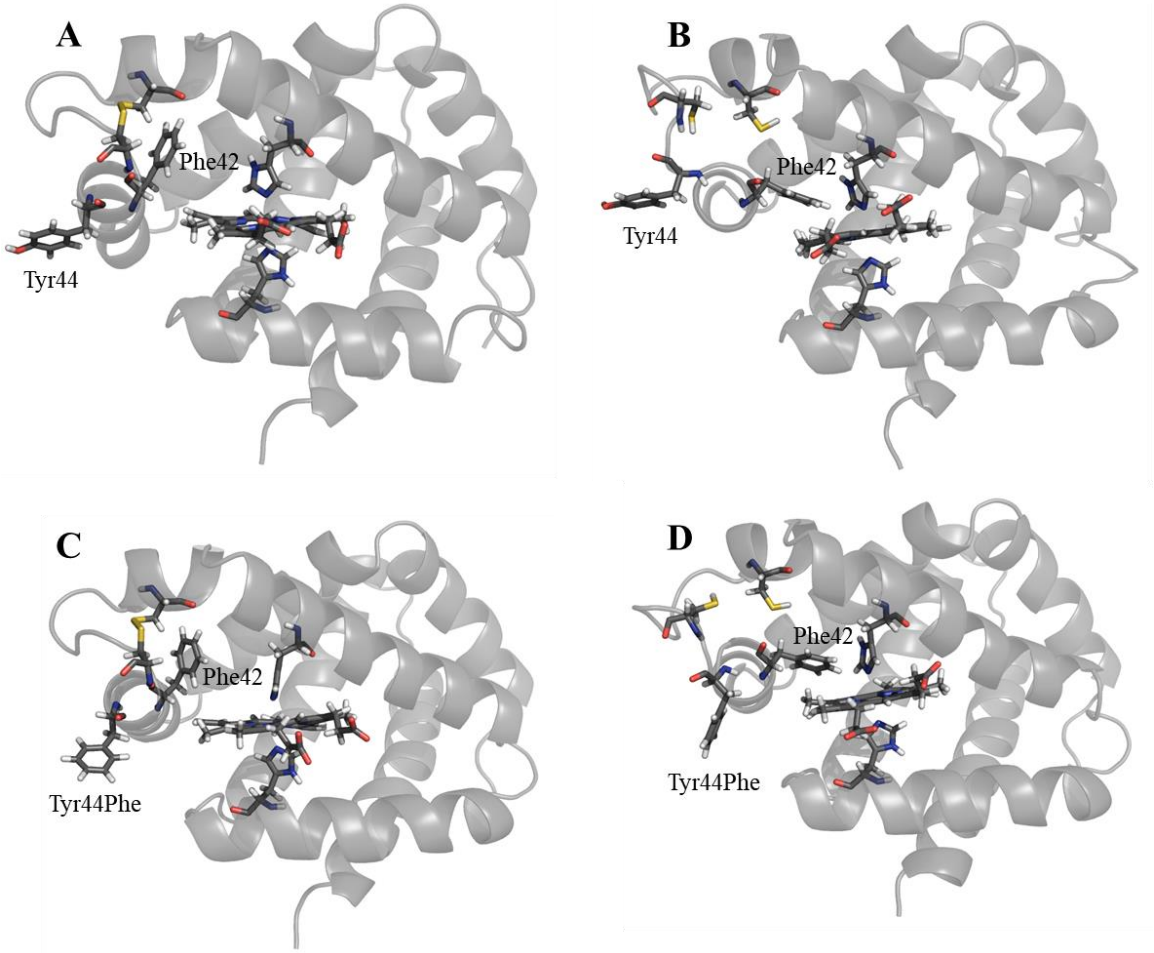

Figure 7.3. Impact of disulfide bond on orientation of Phe42 in hexacoordinate hNgbs. Panels A-D depict hNgbWTox, hNgbWTred, hNgbY44Fox, hNgbY44Fred, respectively.

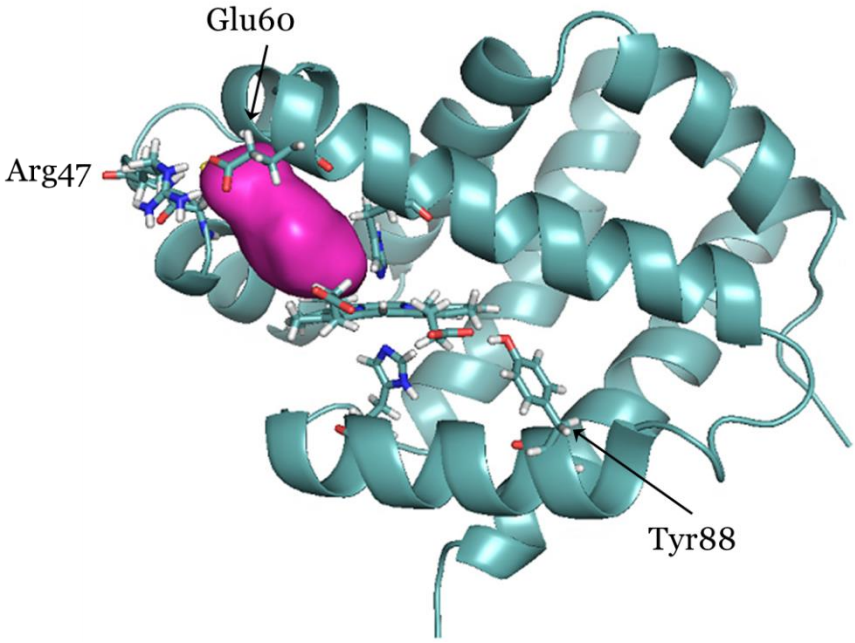

Figure 7.4. Tunnel (shown in magenta) between solvent and distal histidine in hexacoordinate hNgbWT^{ox}, propagated by Phe42 orientation and Arg47-Glu60 hydrogen bond formation. Identical tunnel is observed in hNgbY44F^{ox} hexacoordinate simulation (not shown).

Ligand rebinding to pentacoordinate Ngb

CO bimolecular rebinding to pentacoordinate hNgbWT^{red} is multiphasic with the rate constants for the fast and slow phases being 226 ± 7 μM^{-1} s^{-1} (~23%) and 43 ± 2 μM^{-1} s^{-1} (~77%), respectively. Analogous rate constants were observed for the hNgbY44F with the oxidized and reduced disulfide bond (Table 7.2). Both bimolecular rate constants are approximately four times faster compared to the rate constants determined for bimolecular CO association to the hNgbWT^{ox}, although the amplitude of the faster bimolecular rate constant is ~3 times larger in case of the ligand association to hNgbWT^{ox}.

Sample	k_{bim1} ($\mu M^{-1}s^{-1}$)	A_{bim1} (%)	k_{bim2} ($\mu M^{-1}s^{-1}$)	A_{bim2} (%)
hNgbWT^{ox}	61	66	9	34
hNgbWT^{red}	226	23	43	77
hNgbY44F^{ox}	241	30	30	70
hNgbY44F ^{red}	238	27	30	73

Table 7.2. Rate constants for the bimolecular CO rebinding to Ngbs and geminate quantum yield. (Astudillo 2014)

Pentacoordinate Ngb- MD

Tyr44 orientation. In the absence of the distal histidine in the position of the sixth axial ligand, orientation of Tyr44 sidechain is highly dynamic in all constructs studied. Dynamics of the CD region appear to be highly sensitive to the substitution of Tyr44 by Phe and/or reduction of the disulfide bond (Figure 7.5). The backbone of this region is relatively rigid in hNgbWT^{ox} and becomes highly dynamic in NgbY44F^{red} construct. Furthermore, the side chain of residue 44 is least flexible in hNgbWT^{ox} and appears to be stabilized in its position by a weak π-π stacking with Phe49 sidechain (centroid distance is ~7 Å). In addition to Cys46-Cys55 covalent bond and Tyr44-Phe49 hydrophobic interaction, CD region is further stabilized by backbone hydrogen bonds between Cys46-Phe42 and Asn45-Leu41 in hNgbWT^{ox}, resulting in formation of a 3-turn C helix. Interestingly, hNgbY44F^{ox}, hNgbWT^{red} and hNgbY44F^{red} lack interactions between Phe44-Phe49, Cys46-Phe42 and Asn45-Leu41, contributing to partial unfolding of C helix (1-2 turns) and higher RMSD of CD region residues compared to hNgbWT^{ox} (Figures 7.5 and 7.7).

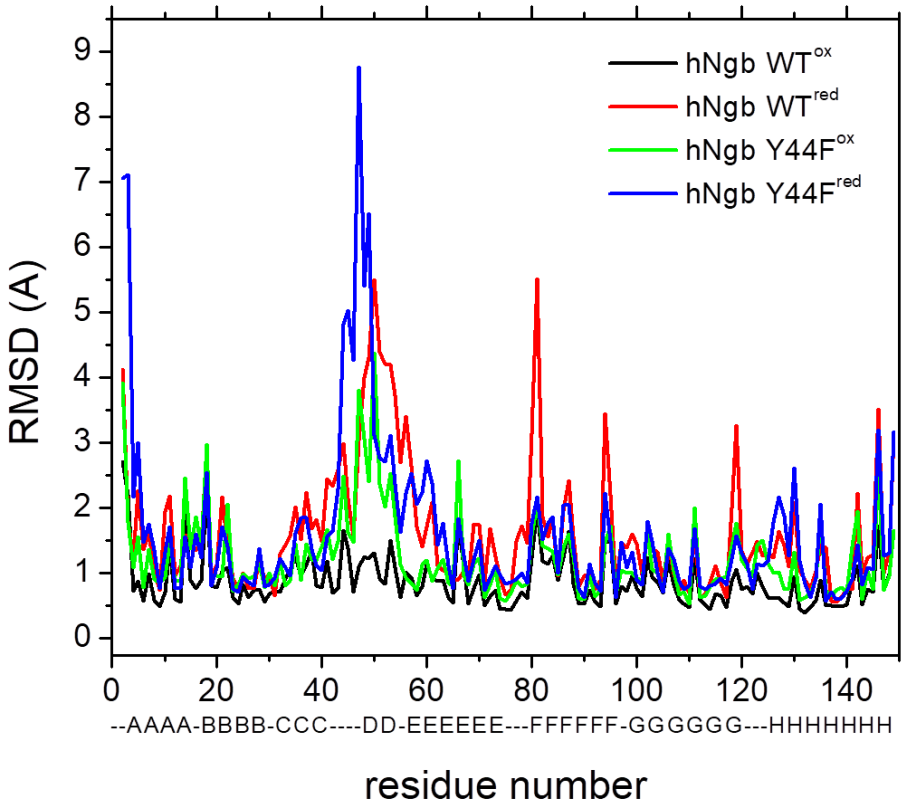

Figure 7.5. Root mean square deviation determined from MD trajectories of pentacoordinated hNgbWT^{ox}, hNgbWT^{red}, hNgbY44F^{ox} and hNgbY44F^{red}. Residues forming helices A-H are denoted below x-axis.

Heme environment. The most significant difference between the simulations of pentacoordinated hNgbs is the orientation of His64 sidechain (Figures 7.6 and 7.8). Analysis of the average structures shows that the distance between heme iron and His64-Nε is 4.4 Å in hNgbWT^{ox}, 7.2 Å in hNgbY44F^{ox}, 6.6 Å in hNgbWT^{red}, and 8.5 Å in hNgbY44F^{red}. Interestingly, average solvent accessible surface area of His64 does not differ significantly between these simulations (data not shown). The "swinging" motion of the distal histidine sidechain in hNgbWT^{ox} appears to be hindered by Asn45, which is positioned in the distal cavity as a result of an elongated C helix. In contrast, Asn45 is a part of flexible CD loop in hNgbWT^{red}, hNgbY44F^{ox} and hNgbY44F^{red}, which displaces

Asn45 further away from heme, thus allowing distal histidine reorientation towards heme-7-propionate.

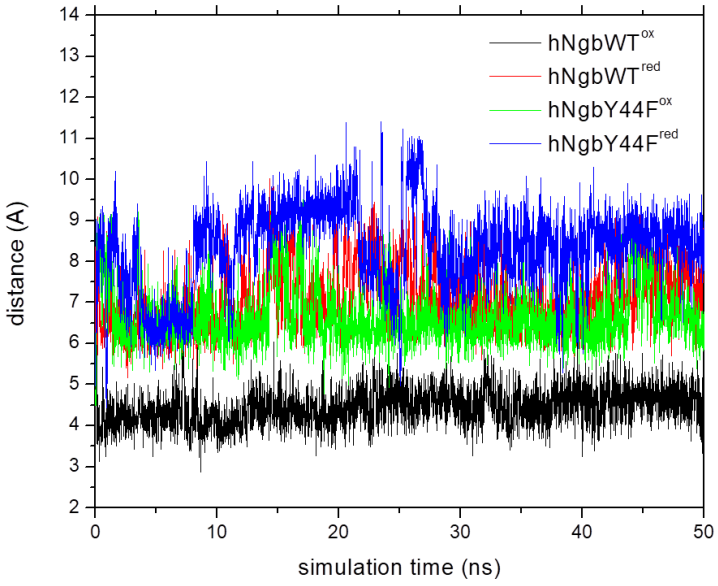

Figure 7.6. Distance between His64-Nε and heme iron during the course of pentacoordinate hNgbs simulation.

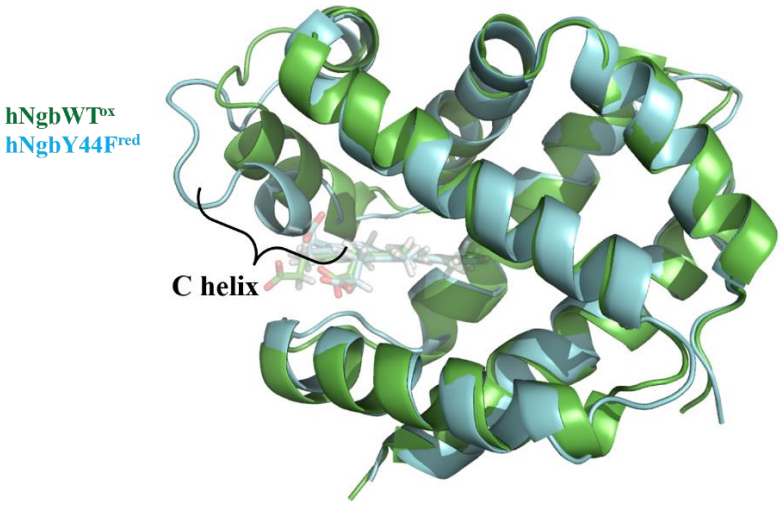

Figure 7.7. Representative structures of pentacoordinated hNgbWT^{ox} (green) and hNgbY44F^{red} (blue) demonstrating the destabilization of C helix upon Tyr44 mutation and/or disulfide bond reduction.

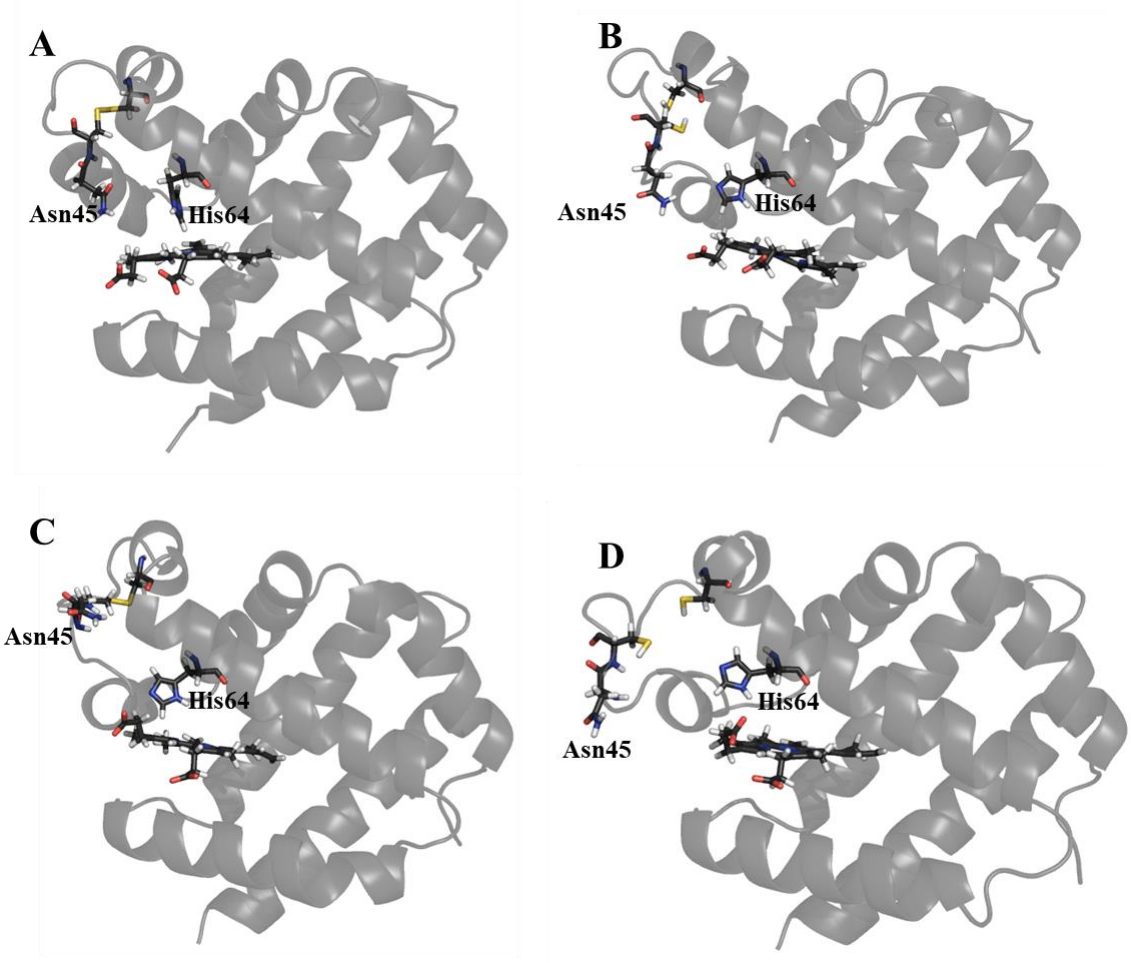

Figure 7.8. Last frames from the pentacoordinate Ngb MD simulations. Panels A-D depict hNgbWT^{ox}, hNgbWT^{red}, hNgbY44F^{ox}, hNgbY44F^{red}, respectively. Heme and several residues are shown in stick representation, including Asn45 and His64 (labeled), and disulfide-forming Cys residues (not labeled).

7.3. Discussion

Regulation of ligand kinetics by propionate-binding residue in position CD3 has been explored in other globins before. Based on NMR studies, Lecomte and La Mar suggested that Arg45(CD3) in sperm whale Mb (swMb) encloses the distal pocket by forming simultaneous hydrogen bonds with the heme propionate group and a residue on the E helix, thus shielding the heme from ligand entry (Lecomte and La Mar 1985). Despite participation in an extensive noncovalent network involving and surrounding the

heme cofactor, mutation of CD3 residue showed only modest impact on O_2 or CO binding, decreasing the rate of ligand association by a factor of ~2 in sperm whale and human Mb (Carver et al. 1991; Lambright et al. 1994). The opening of the CD3-heme interaction was observed computationally in high-temperature simulations, which resulted in the opening of the shortest path between binding site and solvent, the so-called histidine gate (Elbert and Karplus 1990).

In Ngb, position CD3 is occupied by a Tyr residue which is conserved in all Ngbs, but absent in other vertebrate globins (Figure 7.9), possibly indicating unique functional role.

```
Human Cygb   1   MEKVPGEMEIERRERSEELSEAERKAVQAMWARLYANCEDVGVAILVRFFVNFPSAKQYF   60
Human Ngb    1   ------------------MERPEPELIRQSWRAVSRSPLEHGTVLFARLFALEPDLLPLF   42
Human Hb α   1   ----------------MVLSPADKTNVKAAWGKVGAHAGEYGAEALERMFLSFPTTKTYF   44
Horse Mb     1   ----------------MGLSDGEWQQVLNVWGKVEADIAGHGQEVLIRLFTGHPETLEKF   44
Horse Hb β   1   ---------------MVHLTPEEKSAVTALWGKVNV--DEVGGEALGRLLVVYPWTQRFF   43
                                 :   :   :   *  :       *   : *::   *     *

Human Cygb  61   S-QFKHMEDPLEMERSPQLRKHACRVMGALNTVVENLHDPDKVSSVLALVGKAHALKHKV   119
Human Ngb   43   QYNCRQFSSPEDCLSSPEFLDHIRKVMLVIDAAVTNVEDLSSLEEYLASLGRKHRA-VGV   101
Human Hb α  45   P-HFD------LSHGSAQVKGHGKKVADALTNAVAHVD---DMPNALSALSDLHAHKLRV   94
Horse Mb    45   D-KFKHLKTEAEMKASEDLKKHGTVVLTALGGILKKKG---HHEAELKPLAQSHATKHKI   100
Horse Hb β  44   E-SFGDLSTPDAVMGNPKVKAHGKKVLGAFSDGLAHLD---NLKGTFATLSELHCDKLHV   99
                              . ..  *   *  .:   : :          :  :.  *     :

Human Cygb  120  EPVYFKILSGVILEVVAEEFASDFPPETQRAWAKLRGLIYSHVTAAYKEVGWVQQVPNAT   179
Human Ngb   102  KLSSFSTVGESLLYMLEKCLGPAFTPATRAAWSQLYGAVVQAMSR-----GWDGE-----   151
Human Hb α  95   DPVNFKLLSHCLLVTLAAHLPAEFTPAVHASLDKFLASVSTVLTSKYR-----------   142
Horse Mb    101  PIKYLEFISDAIIHVLHSKHPGDFGADAQGAMTKALELFRNDIAAKYKELGFQG------   154
Horse Hb β  100  DPENFRLLGNVLVCVLAHHFGKEFTPPVQAAYQKVVAGVANALAHKYH-----------   147
                     :  :.  ::  :       *   .: :  :    .   ::

Human Cygb  180  TPPATLPSSGP                                                  190
Human Ngb   152  -----------                                                  151
Human Hb α  143  -----------                                                  142
Horse Mb    155  -----------                                                  154
Horse Hb β  148  -----------                                                  147
```

Figure 7.9. Alignment of vertebrate globin sequences, showing position of CD3 residue in hNgb (red) compared to other globins (blue).

Kinetics data show that in the penta-coordinated form, rates of bimolecular CO rebinding are fast and similar for hNgbY44F^{ox}, hNgbWT^{red} and hNgbY44F^{red}, demonstrating that Tyr44 to Phe substitution has equivalent impact on ligand binding to five coordinate Ngb, as does the rupture of the disulfide bond. Experimental data are in agreement with the MD simulations that show increased His64 sidechain displacement in hNgbY44F^{ox}, hNgbWT^{red} and hNgbY44F^{red}. The distal histidine is located above the heme iron in hNgbWT^{ox}, whereas the imidazole group "swings" out towards the CD loop in the remaining pentacoordinate simulations, leaving a more exposed distal site. Similar opening of the distal cavity via the histidine gate was observed in phenyl-bound swMb (Ringe et al. 1984), which is suggested to be a representative structure of the conformational reorganization needed for ligand entry directly from the solvent into the distal pocket (Figure 7.10). In phenyl-Mb, the histidine displacement is facilitated by Arg45(CD3) sidechain reorientation, similar to Asn45(CD4) translocation observed in hNgbWT^{red}, hNgbY44F^{ox} and hNgbY44F^{red}. Together, these data suggest that ligand access to the binding site is modulated by displacement of His64 sidechain, which is regulated by Tyr44 and/or disulfide bond.

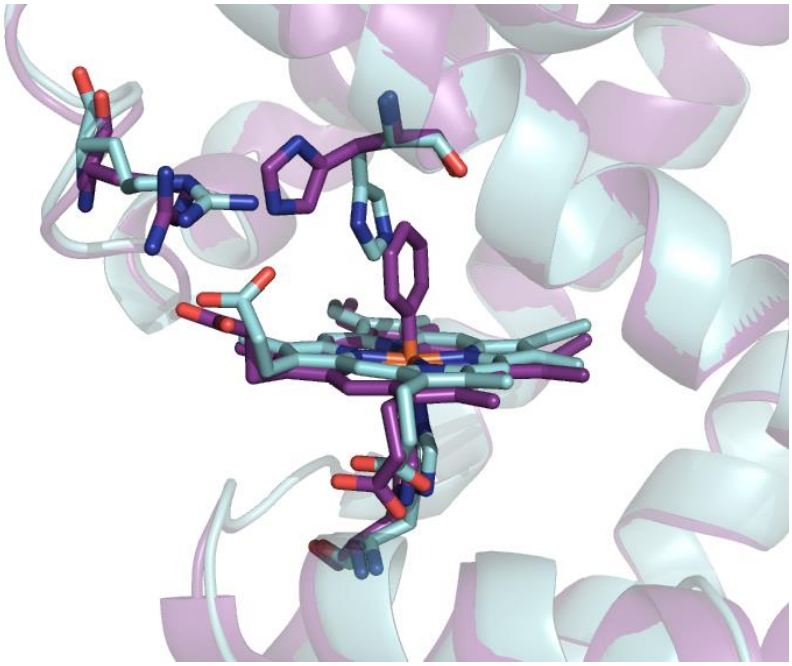

Figure 7.10. Overlay of swMb structures in the ferric-unbound (blue, PDB: 1VXA) and phenyl-bound (purple: PDB: 5IKS) forms. (Wang, Thomas, and Richter-Addo 2016; Yang and Phillips 1996)

Furthermore, ligand interactions with hexa-coordinate hNgb are mainly controlled by the disulfide bond and are less sensitive to the Tyr44 mutation than ligand interactions with pentacoordinated species. Experimental evidence showing faster ligand association in oxidized hexacoordinate hNgbs is consistent with the computational data, which reveled increased solvent accessibility of the distal cavity in oxidized, rather than reduced protein form, suggesting an easier ligand access to the sixth coordination site. Solvation of the distal pocket is allowed by disulfide-sensitive Phe42 orientation, which was observed before (Morozov et al. 2014). Morozov *et al*. therefore hypothesized that reduced rates of distal histidine dissociation in the absence of the disulfide bond is a result of the steric strain between Phe42 and His64 sidechains, which is in agreement with our simulations as well.

7.4. Summary

To gain a better understanding of protein motions that regulate ligand interactions with hNgb, we performed molecular dynamics (MD) simulations of penta- and hexacoordinate forms of all constructs studied here. Combined experimental and computational data suggest that Tyr44 is essential for communication between the CD region and the ligand binding site in pentacoordinate hNgb, but does not significantly contribute to distal histidine-disulfide bond coupling in hexacoordinate species.

LIST OF REFERENCES

Abriata, Luciano A. 2011. "A Simple Spreadsheet Program to Simulate and Analyze the Far-UV Circular Dichroism Spectra of Proteins." *Journal of Chemical Education* 88(9): 1268–73.

Albani, Jihad, and Bernard Alpert. 1987. "Fluctuation Domains in Myoglobin: Fluorescence Quenching Studies." *European Journal of Biochemistry* 162(1): 175–78.

Allen, Michael P., and D J Tildesley. 1987. Liquids, Oxford University Press, New York *Computer Simulation of Liquids*. Oxford University Press.

Andrew, Colin R. et al. 2016. "The Dynamics behind the Affinity: Controlling Heme-Gas Affinity via Geminate Recombination and Heme Propionate Conformation in the NO Carrier Cytochrome C′." *ACS Chemical Biology* 11(11): 3191–3201.

Anselmi, Massimiliano, Maurizio Brunori, Beatrice Vallone, and Alfredo Di Nola. 2007. "Molecular Dynamics Simulation of Deoxy and Carboxy Murine Neuroglobin in Water." *Biophysical journal* 93(2): 434–41.

Antao, Shane T., T.T. Hong Duong, Roshanak Aran, and Paul K. Witting. 2010. "Neuroglobin Overexpression in Cultured Human Neuronal Cells Protects Against Hydrogen Peroxide Insult *via* Activating Phosphoinositide-3 Kinase and Opening the Mitochondrial K_{ATP} Channel." *Antioxidants & Redox Signaling* 13(6): 769–81.

Antonini, Eraldo, and Maurizio Brunori. 1971. *Hemoglobin and Myoglobin in Their Interactions with Ligands*. eds. A. Neuberger and E. L. Tatum. Amsterdam: North-Holland Publishing Company.

Astudillo, Luisana et al. 2012. "Conformational Dynamics in Human Neuroglobin: Effect of His64, Val68, and Cys120 on Ligand Migration." *Biochemistry* 51(50): 9984–94.

———. 2013. "Reduction of the Internal Disulfide Bond between Cys 38 and 83 Switches the Ligand Migration Pathway in Cytoglobin." *Journal of Inorganic Biochemistry* 129: 23–29.

———. 2014. "Conformational Dynamics Associated with Ligand Binding to Vertebrate Hexa-Coordinate Hemoglobins." Florida International University.

Atkins, Peter, and J De Paula. 2006. Chemistry *Atkins' Physical Chemistry*. 8th ed. New York: W. H. Freeman and Company.

Barrick, Doug. 1994. "Replacement of the Proximal Ligand of Sperm Whale Myoglobin with Free Imidazole in the Mutant His-93→Gly." *Biochemistry* 33(21): 6546–54.

Beckerson, Penny, Michael T. Wilson, Dimitri A. Svistunenko, and Brandon J. Reeder. 2015. "Cytoglobin Ligand Binding Regulated by Changing Haem-Co-Ordination in Response to Intramolecular Disulfide Bond Formation and Lipid Interaction." *Biochemical Journal* 465(1): 127–37.

Birukou, Ivan, Rachel L. Schweers, and John S. Olson. 2010. "Distal Histidine Stabilizes Bound O2 and Acts as a Gate for Ligand Entry in Both Subunits of Adult Human Hemoglobin." *Journal of Biological Chemistry* 285(12): 8840–54.

Blank, Miriam, Jessica Wollberg, et al. 2011. "A Membrane-Bound Vertebrate Globin." *PLoS ONE* 6(9).

Blank, Miriam, Laurent Kiger, et al. 2011. "Oxygen Supply from the Bird's Eye Perspective: Globin E Is a Respiratory Protein in the Chicken Retina." *Journal of Biological Chemistry* 286(30): 26507–15.

Blank, Miriam, and Thorsten Burmester. 2012. "Widespread Occurrence of N-Terminal Acylation in Animal Globins and Possible Origin of Respiratory Globins from a Membrane-Bound Ancestor." *Molecular Biology and Evolution* 29(11): 3553–61.

Bocahut, Anthony et al. 2013. "Heme Orientation Modulates Histidine Dissociation and Ligand Binding Kinetics in the Hexacoordinated Human Neuroglobin." *Journal of biological inorganic chemistry : JBIC : a publication of the Society of Biological Inorganic Chemistry* 18(1): 111–22.

Bocahut, Anthony, Sophie Bernad, Pierre Sebban, and Sophie Sacquin-Mora. 2009. "Relating the Diffusion of Small Ligands in Human Neuroglobin to Its Structural and Mechanical Properties." *The journal of physical chemistry. B* 113: 16257–67.

Breslow, E. 1964. "Changes in Side Chain Reactivity Accompanying the Binding of Heme To Sperm Whale Apomyoglobin." *The Journal of biological chemistry* 239(2): 486–96.

Brunori, M et al. 2000. "The Role of Cavities in Protein Dynamics: Crystal Structure of a Photolytic Intermediate of a Mutant Myoglobin." *Proceedings of the National Academy of Sciences of the United States of America* 97(5): 2058–63.

Brunori, Maurizio, and Quentin H. Gibson. 2001. "Cavities and Packing Defects in the Structural Dynamics of Myoglobin." *EMBO Reports* 2(8): 674–79.

Burmester, T., B. Ebner, B. Weich, and T. Hankeln. 2002. "Cytoglobin: A Novel Globin Type Ubiquitously Expressed InVertebrate Tissues." *Molecular Biology and Evolution* 19(4): 416–21.

Burmester, T., and T. Hankeln. 2014. "Function and Evolution of Vertebrate Globins." *Acta Physiologica* 211(3): 501–14.

Burmester, T, B Weich, S Reinhardt, and T Hankeln. 2000. "A Vertebrate Globin Expressed in the Brain." *Nature* 407(6803): 520–23.

Capece, Luciana et al. 2006. "Heme Protein Oxygen Affinity Regulation Exerted by Proximal Effects." *Journal of the American Chemical Society* 128(38): 12455–61.

———. 2013. "Small Ligand-Globin Interactions: Reviewing Lessons Derived from Computer Simulation." *Biochimica et Biophysica Acta - Proteins and Proteomics* 1834(9): 1722–38.

Capellos, Christos, and Benon H. J. Bielski. 1972. *Kinetic Systems: Mathematical Description of Chemical Kinetics in Solution*. Wiley-Interscience.

Carver, Theodore E. et al. 1991. "Contributions of Residue 45(CD3) and Heme-6-Propionate to the Bimolecular and Geminate Recombination Reactions of Myoglobin." *Biochemistry* 30(19): 4697–4705.

Chakraborty, Saumen et al. 2014. "Spectroscopic and Computational Study of a Nonheme Iron Nitrosyl Center in a Biosynthetic Model of Nitric Oxide Reductase." *Angewandte Chemie - International Edition* 53(9): 2417–21.

Chen, Li Ming et al. 2012. "Neuroglobin Attenuates Alzheimer-like Tau Hyperphosphorylation by Activating Akt Signaling." *Journal of Neurochemistry* 120(1): 157–64.

Chu, Kelvin et al. 2000. "Structure of a Ligand-Binding Intermediate in Wild-Type Carbonmonoxy Myoglobin." *Nature* 403(6772): 921–23.

Ciaccio, Chiara et al. 2013. "Functional and Structural Roles of the N-Terminal Extension in Methanosarcina Acetivorans Protoglobin." *Biochimica et Biophysica Acta - Proteins and Proteomics* 1834(9): 1813–23.

Cohen, Jordi, Anton Arkhipov, Rosemary Braun, and Klaus Schulten. 2006. "Imaging the Migration Pathways for O2, CO, NO, and Xe inside Myoglobin." *Biophysical Journal* 91(5): 1844–57.

Cohen, Jordi, Kenneth W. Olsen, and Klaus Schulten. 2008. "Finding Gas Migration Pathways in Proteins Using Implicit Ligand Sampling." *Methods in Enzymology* 437: 439–57.

Corti, Paola et al. 2016. "Globin X Is a Six-Coordinate Globin That Reduces Nitrite to Nitric Oxide in Fish Red Blood Cells." *Proceedings of the National Academy of Sciences* 113(30): 8538–43.

Cosby, Kenyatta et al. 2003. "Nitrite Reduction to Nitric Oxide by Deoxyhemoglobin Vasodilates the Human Circulation." *Nature Medicine* 9(12): 1498–1505.

Dixit, B. P Sudha N et al. 1982. "Rotational Motion of Cytochrome c Derivatives Bound to Membranes Measured by Fluorescence and Phosphorescence Anisotropy." *European Journal of Biochemistry* 126(1): 1–9.

Doyle, Michael P., and James W. Hoekstra. 1981. "Oxidation of Nitrogen Oxides by Bound Dioxygen in Hemoproteins." *Journal of Inorganic Biochemistry* 14(4): 351–58.

Dröge, Jasmin, and Wojciech Makałowski. 2011. "Phylogenetic Analysis Reveals Wide Distribution of Globin X." *Biology Direct* 6(1): 54.

Du, Weihong et al. 2003. "Solution 1H NMR Characterization of Equilibrium Heme Orientational Disorder with Functional Consequences in Mouse Neuroglobin." *Journal of the American Chemical Society* 125(27): 8080–81.

Elbert, R., and M. Karplus. 1990. "Enhanced Sampling in Molecular Dynamics: Use of the Time-Dependent Hartree Approximation for a Simulation of Carbon Monoxide Diffusion through Myoglobint." *Journal of the American Chemical Society* 112(25): 9161–75.

Evans, Stephen V., and Gary D. Brayer. 1990. "High-Resolution Study of the Three-Dimensional Structure of Horse Heart Metmyoglobin." *Journal of Molecular Biology* 213(4): 885–97.

Ezhevskaya, Maria et al. 2011. "EPR Investigation of the Role of B10 Phenylalanine in Neuroglobin - Evidence That B10Phe Mediates Structural Changes in the Heme Region upon Disulfide-Bridge Formation." *Journal of Inorganic Biochemistry* 105(9): 1131–37.

Fago, Angela et al. 2004. "Allosteric Regulation and Temperature Dependence of Oxygen Binding in Human Neuroglobin and Cytoglobin: Molecular Mechanisms and Physiological Significance." *Journal of Biological Chemistry* 279(43): 44417–26.

———. 2006. "The Reaction of Neuroglobin with Potential Redox Protein Partners Cytochrome B5 and Cytochrome C." *FEBS Letters* 580(20): 4884–88.

Fanelli, A. Rossi, E. Antonini, and A. Caputo. 1958. "Studies on the Structure of Hemoglobin I. Physicochemical Properties of Human Globin." *BBA - Biochimica et Biophysica Acta* 30(3): 608–15.

Feitelson, J., and N. Barboy. 1986. "Triplet-State Reactions of Zinc Protoporphyrins." *Journal of Physical Chemistry* 90(2): 271–74.

Feitelson, Jehuda, and Thomas G. Spiro. 1986. "Bonding in Zinc Proto- and Mesoporphyrin Substituted Myoglobin and Model Compounds Studied by Resonance Raman Spectroscopy." *Inorganic Chemistry* 25(6): 861–65.

Fuchs, C., T. Burmester, and T. Hankeln. 2006. "The Amphibian Globin Gene Repertoire as Revealed by the Xenopus Genome." *Cytogenetic and Genome Research* 112(3–4): 296–306.

Gabba, Matteo et al. 2013. "CO Rebinding Kinetics and Molecular Dynamics Simulations Highlight Dynamic Regulation of Internal Cavities in Human Cytoglobin." *PLoS ONE* 8(1): e49770.

Gardner, Paul R. 2012. "Hemoglobin: A Nitric-Oxide Dioxygenase." *Scientifica* 2012: 1–34.

Geuens, Eva et al. 2003. "A Globin in the Nucleus!" *Journal of Biological Chemistry* 278(33): 30417–20.

Gibson, Quentin H. 1956. "An Apparatus for Flash Photolysis and Its Application to the Reactions of Myoglobin with Gases." *The Journal of Physiology* 134(1): 112–22.

———. 1992. "Distal Pocket Residues Affect Picosecond Ligand Recombination in Myoglobin. An Experimental and Molecular Dynamics Study of Position 29 Mutants." *Journal of Biological Chemistry* 267(31): 22022–34.

Gibson, Quentin H., and Stanley Ainsworth. 1957. "Photosensitivity of Hæm Compounds [15]." *Nature* 180(4599): 1416–17.

Gingrich, David J., Judith M. Nocek, Michael J. Natan, and Brian M. Hoffman. 1987. "Porphyrin Vinyl Groups Act as Antennae for Electron Transfer within [Fe,Zn] Hemoglobin Hybrids." *Journal of the American Chemical Society* 109(24): 7533–34.

Greenfield, Norma J. 2006. "Using Circular Dichroism Collected as a Funcion of Temperature to Determine the Thermodynamics of Protein Unfolding and Binding Interactions." *Nature Protocols* 1(6): 2527–35.

Guimarães, Beatriz G. et al. 2014. "The Crystal Structure of Wild-Type Human Brain Neuroglobin Reveals Flexibility of the Disulfide Bond That Regulates Oxygen Affinity." *Acta Crystallographica Section D: Biological Crystallography* 70(4): 1005–14.

Halligan, Katharine E., Frances L. Jourd'heuil, and David Jourd'heuil. 2009. "Cytoglobin Is Expressed in the Vasculature and Regulates Cell Respiration and Proliferation via Nitric Oxide Dioxygenation." *Journal of Biological Chemistry* 284(13): 8539–47.

Hamdane, Djemel et al. 2003. "The Redox State of the Cell Regulates the Ligand Binding Affinity of Human Neuroglobin and Cytoglobin." *Journal of Biological Chemistry* 278(51): 51713–21.

———. 2005. "Hyperthermal Stability of Neuroglobin and Cytoglobin." *FEBS Journal* 272(8): 2076–84.

Hanai, Shumpei et al. 2018. "Roles of N- and C-Terminal Domains in the Ligand-Binding Properties of Cytoglobin." *Journal of Inorganic Biochemistry* 179: 1–9.

Hargrove, Mark S. et al. 1994. "Stability of Myoglobin: A Model for the Folding of Heme Proteins." *Biochemistry* 33(39): 11767–75.

———. 2000. "A Flash Photolysis Method to Characterize Hexacoordinate Hemoglobin Kinetics." *Biophysical Journal* 79(5): 2733–38.

Harrison, S. C., and E. R. Blout. 1965. "Reversible Conformational Changes of Myoglobin and Apomyoglobin." *The Journal of biological chemistry* 240: 299–303.

Hartridge, H., and F. J. W. Roughton. 1923. "The Kinetics of Haemoglobin. II. The Velocity with Which Oxygen Dissociates from Its Combination with Haemoglobin." *Proceedings of the Royal Society* 104(376).

Hayashi, Takashi et al. 2002. "Contribution of Heme-Propionate Side Chains to Structure and Function of Myoglobin: Chemical Approach by Artificially Created Prosthetic Groups." In *Journal of Inorganic Biochemistry*, , 94–100.

Henry, Eric R. et al. 1983. "Geminate Recombination of Carbon Monoxide to Myoglobin." *Journal of Molecular Biology* 166(3): 443–51.

Holde, Kensal E. Van, W. Curtis Johnson, and P. Shing Ho. 1998. Education *Principles of Physical Biochemistry*.

Honig, George R. et al. 1990. "Hemoglobin Warsaw (Pheb42(CD)- Val), an Unstable Variant with Decreased Oxygen Affinity." *Journal of Biological Chemistry* 265(1): 126–32.

Hoogewijs, David et al. 2012. "Androglobin: A Chimeric Globin in Metazoans That Is Preferentially Expressed in Mammalian Testes." *Molecular Biology and Evolution* 29(4): 1105–14.

Huang, X, and S G Boxer. 1994. "Discovery of New Ligand Binding Pathways in Myoglobin by Random Mutagenesis." *Nat. Struct. Biol.* 1(4): 226–29.

Hui, Hilda L. et al. 2004. "Ligand Binding to Symmetrical FeZn Hybrids of Variants of Human HbA with Modifications in the A1-B2 Interface." *Biochemistry* 43(24): 7843–50.

Humphrey, William, Andrew Dalke, and Klaus Schulten. 1996. "VMD: Visual Molecular Dynamics." *Journal of Molecular Graphics* 14(1): 33–38.

Hundahl, Christian Ansgar et al. 2013. "A Gene-Environment Study of Cytoglobin in the Human and Rat Hippocampus." *PLoS ONE* 8(5).

"ISS. Technical Diagrams. Schematic Diagram for PC1." http://www.iss.com/fluorescence/instruments/pc1.html.

Jameson, David M. 2014. *Introduction to Fluorescence*. Boca Raton, FL.

Jamil, Farrukh et al. 2014. "Crystal Structure of Truncated Haemoglobin from an Extremely Thermophilic and Acidophilic Bacterium." *Journal of Biochemistry* 156(2): 97–106.

Jennings, Patricia A., and Peter E. Wright. 1993. "Formation of a Molten Globule Intermediate Early in the Kinetic Folding Pathway of Apomyoglobin." *Science* 262(5135): 892–96.

Jensen, Frank. 2007. John Wiley & Sons, LTD *Introduction to Computational Chemistry*. Second.

John, Rince et al. 2014. "DNA Damage Induced Activation of Cygb Stabilizes P53 and Mediates G1 Arrest." *DNA Repair* 24: 107–12.

Kakar, Smita et al. 2010. "Structure and Reactivity of Hexacoordinate Hemoglobins." *Biophysical chemistry* 152(1–3): 1–14.

Kavanaugh, Jeffrey S., Paul H. Rogers, and Arthur Arnone. 2005. "Crystallographic Evidence for a New Ensemble of Ligand-Induced Allosteric Transitions in Hemoglobin: The T-to-THighquaternary Transitions." *Biochemistry*.

Kawada, N et al. 2001. "Characterization of a Stellate Cell Activation-Associated Protein (STAP) with Peroxidase Activity Found in Rat Hepatic Stellate Cells." *The Journal of biological chemistry* 276(27): 25318–23.

Kelly, Sharon M, Thomas J Jess, and Nicholas C Price. 2005. "How to Study Proteins by Circular Dichroism." *Biochimica et biophysica acta* 1751(2): 119–39.

Kendrew, J. C. et al. 1960. "Structure of Myoglobin: A Three-Dimensional Fourier Synthesis at 2 A Resolution." *Nature* 185(4711): 422–27.

Keskin, Ozlem, Attila Gursoy, Buyong Ma, and Ruth Nussinov. 2008. "Principles of Protein-Protein Interactions: What Are the Preferred Ways for Proteins to Interact?" *Chemical Reviews*.

Khan, Adil a et al. 2006. "Neuroglobin-Overexpressing Transgenic Mice Are Resistant to Cerebral and Myocardial Ischemia." *Proceedings of the National Academy of Sciences* 103(47): 17944–48.

Kholodenko, Yuri et al. 1999. "Heme Protein Dynamics Revealed by Geminate Nitric Oxide Recombination in Mutants of Iron and Cobalt Myoglobin." *Biochemistry* 38(18): 5918–24.

Knight, J D, D Hamelberg, J A McCammon, and R Kothary. 2009. "The Role of Conserved Water Molecules in the Catalytic Domain of Protein Kinases." *Proteins* 76(3): 527–35.

Koshiyama, Tomomi et al. 2011. "Post-Crystal Engineering of Zinc-Substituted Myoglobin to Construct a Long-Lived Photoinduced Charge-Separation System." *Angewandte Chemie - International Edition*.

Kovalevsky, Andrey Y. et al. 2010. "Direct Determination of Protonation States of Histidine Residues in a 2 Å Neutron Structure of Deoxy-Human Normal Adult Hemoglobin and Implications for the Bohr Effect." *Journal of Molecular Biology* 398(2): 276–91.

Kugelstadt, Dominik, Mark Haberkamp, Thomas Hankeln, and Thorsten Burmester. 2004. "Neuroglobin, Cytoglobin, and a Novel, Eye-Specific Globin from Chicken." *Biochemical and Biophysical Research Communications* 325(3): 719–25.

Kumazaki, S. et al. 2000. "Dissociation and Recombination between Ligands and Heme in a CO-Sensing Transcriptional Activator CooA: A Flash Photolysis Study." *Journal of Biological Chemistry* 275(49): 38378–83.

Kuzmanic, Antonija, and Bojan Zagrovic. 2010. "Determination of Ensemble-Average Pairwise Root Mean-Square Deviation from Experimental B-Factors." *Biophysical Journal* 98(5): 861–71.

Lakowicz, Joseph R. et al. 1984. "Analysis of Fluorescence Decay Kinetics from Variable-Frequency Phase Shift and Modulation Data." *Biophysical Journal* 46(4): 463–77.

———. 2002. 6 by JR Lakowicz, Plenum, New York *Topics in Fluorescence Spectroscopy, Protein Fluorescence*. Kluwer Academic Publisher.

———. 2006. Principles of Fluorescence Spectroscopy *Principles of Fluorescence Spectroscopy*.

Lambright, David G., Sriram Balasubramanian, Sean M. Decatur, and Steven G. Boxer. 1994. "Anatomy and Dynamics of a Ligand-Binding Pathway in Myoglobin: The Roles of Residues 45, 60, 64, and 68." *Biochemistry* 33(18): 5518–25.

Lawrie, R A. 1953. "The Relation of Energy-Rich Phosphate in Muscle To Myoglobin and To Cytochrome-Oxidase Activity." *Biochemical Journal* 55(2): 305–9.

Lechauve, Christophe et al. 2010. "Cytoglobin Conformations and Disulfide Bond Formation." *FEBS Journal* 277(12): 2696–2704.

———. 2012. "Neuroglobin Involvement in Respiratory Chain Function and Retinal Ganglion Cell Integrity." *Biochimica et Biophysica Acta - Molecular Cell Research* 1823(12): 2261–73.

Lecomte, Juliette T.J., and Gerd N. La Mar. 1985. "1H NMR Study of Labile Proton Exchange in the Heme Cavity as a Probe for the Potential Ligand Entry Channel in Myoglobin." *Biochemistry* 24(25): 7388–95.

Leonard, John J., Takashi Yonetani, and James B. Callis. 1974. "A Fluorescence Study of Hybrid Hemoglobins Containing Free Base and Zinc Protoporphyrin IX." *Biochemistry* 13(7): 1460–64.

Lepeshkevich, Sergei V. et al. 2014. "Photosensitized Singlet Oxygen Luminescence from the Protein Matrix of Zn-Substituted Myoglobin." *Journal of Physical Chemistry A* 118(10): 1864–78.

Li, Haitao et al. 2012. "Characterization of the Mechanism and Magnitude of Cytoglobin-Mediated Nitrite Reduction and Nitric Oxide Generation under Anaerobic Conditions." *Journal of Biological Chemistry* 287(43): 36623–33.

Li, Xin et al. 2016. "The Identification of Human Aldo-Keto Reductase AKR7A2 as a Novel Cytoglobin-Binding Partner." *Cellular and Molecular Biology Letters* 21(1).

Liang, Zhao Xun et al. 2002. "Dynamic Docking and Electron Transfer between Zn-Myoglobin and Cytochrome B5." *Journal of the American Chemical Society* 124(24): 6849–59.

Liebl, U et al. 1999. "Coherent Reaction Dynamics in a Bacterial Cytochrome c Oxidase." *Nature* 401(6749): 181–84.

Likić, V a, N Juranić, S Macura, and F G Prendergast. 2000. "A 'Structural' Water Molecule in the Family of Fatty Acid Binding Proteins." *Protein science : a publication of the Protein Society* 9(3): 497–504.

Lloyd, Emma et al. 1996. "Electrostatic Modification of the Active Site of Myoglobin: Characterization of the Proximal Ser92Asp Variant." *Biochemistry* 35(36): 11901–12.

Lutz, Stephan, Karin Nienhaus, G. Ulrich Nienhaus, and Markus Meuwly. 2009. "Ligand Migration between Internal Docking Sites in Photodissociated Carbonmonoxy Neuroglobin." *Journal of Physical Chemistry B* 113(46): 15334–43.

Mach, Henryk, C. Russell Middaugh, and Randolph V. Lewis. 1992. "Statistical Determination of the Average Values of the Extinction Coefficients of Tryptophan and Tyrosine in Native Proteins." *Analytical Biochemistry* 200(1): 74–80.

Mackerell, Alexander D. et al. 1998. "All-Atom Empirical Potential for Molecular Modeling and Dynamics Studies of Proteins †." *The Journal of Physical Chemistry B* 102(18): 3586–3616.

Mackerell, Alexander D., N Banavali, and N Foloppe. 2001. "Development and Current Status of the CHARMM Force Field for Nucleic Acids." *Biopolymers* 56(4): 257–65.

Mackerell, Alexander D., Michael Feig, and Charles L. Brooks. 2004. "Extending the Treatment of Backbone Energetics in Protein Force Fields: Limitations of Gas-Phase

Quantum Mechanics in Reproducing Protein Conformational Distributions in Molecular Dynamics Simulation." *Journal of Computational Chemistry* 25(11): 1400–1415.

Makino, Masatomo et al. 2006. "High-Resolution Structure of Human Cytoglobin: Identification of Extra N- and C-Termini and a New Dimerization Mode." *Acta crystallographica. Section D, Biological crystallography* 62(Pt 6): 671–77.

Makino, Masatomo, Hitomi Sawai, Yoshitsugu Shiro, and Hiroshi Sugimoto. 2011. "Crystal Structure of the Carbon Monoxide Complex of Human Cytoglobin." *Proteins* 79(4): 1143–53.

Marks, Gerald S. 1969. *Heme and Chlorophyll*. London: D. Van Nostrand Company.

Miyazaki, Gentaro et al. 1999. "Magnesium (II) and Zinc (II) -Protoporphyrin IX ' s Stabilize the Lowest Oxygen Affinity State of Human Hemoglobin Even More Strongly than Deoxyheme."

Mizutani, Yasuhisa, and Teizo Kitagawa. 1997. "Direct Observation of Cooling of Heme upon Photodissociation of Carbonmonoxy Myoglobin." *Science* 278(5337): 443–46.

Morozov, Alexander N., James P. Roach, Margarita Kotzer, and David C. Chatfield. 2014. "A Possible Mechanism for Redox Control of Human Neuroglobin Activity." *Journal of Chemical Information and Modeling* 54(7): 1997–2003.

Moschetti, Tommaso et al. 2009. "The Structure of Neuroglobin at High Xe and Kr Pressure Reveals Partial Conservation of Globin Internal Cavities." *Biophysical Journal* 97(6): 1700–1708.

Mukhi, Nitika et al. 2016. "Structural and Functional Significance of the N- and C-Terminal Appendages in Arabidopsis Truncated Hemoglobin." *Biochemistry* 55(12): 1724–40.

Naito, Naomi R. et al. 1998. "Binding and Electron Transfer between Cytochrome B5and the Hemoglobin α- and β-Subunits through the Use of [Zn, Fe] Hybrids." *Journal of the American Chemical Society* 120(44): 11256–62.

Nakatani, Kazuki et al. 2004. "Cytoglobin/STAP, Its Unique Localization in Splanchnic Fibroblast-like Cells and Function in Organ Fibrogenesis." *Laboratory Investigation* 84(1): 91–101.

Neya, Saburo et al. 2016. "Utility of Heme Analogues to Intentionally Modify Heme-Globin Interactions in Myoglobin." *Biochimica et Biophysica Acta - Bioenergetics* 1857(5): 582–88.

Nienhaust, Karin, Jan M. Kriegl, and G. Ulrich Nienhaust. 2004. "Structural Dynamics in the Active Site of Murine Neuroglobin and Its Effects on Ligand Binding." *Journal of Biological Chemistry* 279(22): 22944–52.

Olson, John S. et al. 1988. "The Role of the Distal Histidine in Myoglobin and Haemoglobin." *Nature* 336(6196): 265–66.

Olson, John S., J. Soman, and G. N. Phillips. 2007. "Ligand Pathways in Myoglobin: A Review of Trp Cavity Mutations." *IUBMB Life* 59(8–9): 552–62.

Orlowski, Slawomir, and Wieslaw Nowak. 2007. "Locally Enhanced Sampling Molecular Dynamics Study of the Dioxygen Transport in Human Cytoglobin." *Journal of Molecular Modeling* 13(6–7): 715–23.

Ostojić, Jelena et al. 2006. "Neuroglobin and Cytoglobin: Oxygen-Binding Proteins in Retinal Neurons." *Investigative Ophthalmology and Visual Science* 47(3): 1016–23.

Papadopoulos, S et al. 2001. "Radial and Longitudinal Diffusion of Myoglobin in Single Living Heart and Skeletal Muscle Cells." *Proceedings of the National Academy of Sciences of the United States of America* 98(10): 5904–9.

Papp, S. et al. 1990. "Reactions of Excited Triplet States of Metal Substituted Myoglobin with Dioxygen and Quinone." *Biophysical Journal* 58(1): 177–86.

Perutz, M.F., and F.S. Mathews. 1966. "An X-Ray Study of Azide Methaemoglobin." *Journal of Molecular Biology* 21(1): 199–202.

Perutz, M F et al. 1960. "Structure of Haemoglobin: A Three-Dimensional Fourier Synthesis at 5.5-A Resolution, Obtained by X-Ray Analysis." *Nature* 185(4711): 416–22.

Pesce, Alessandra et al. 2003a. "Human Brain Neuroglobin Structure Reveals a Distinct Mode of Controlling Oxygen Affinity." *Structure* 11(9): 1087–95.

———. 2003b. "Human Brain Neuroglobin Structure Reveals a Distinct Mode of Controlling Oxygen Affinity." *Structure* 11(9): 1087–95.

Petrich, J. W., C. Poyart, and J. L. Martin. 1988. "Photophysics and Reactivity of Heme Proteins: A Femtosecond Absorption Study of Hemoglobin, Myoglobin, and Protoheme." *Biochemistry* 27(11): 4049–60.

Phillips, James C. et al. 2005. "Scalable Molecular Dynamics with NAMD." *Journal of Computational Chemistry* 26(16): 1781–1802.

Pietra, Francesco. 2013. "On the Pathways for CO Egress from Carboxy Human Cytoglobin. A Molecular-Dynamics Investigation." *Chemistry and Biodiversity* 10(1): 86–95.

Reeder, Brandon J., and Michael A. Hough. 2014. "The Structure of a Class 3 Nonsymbiotic Plant Haemoglobin from Arabidopsis Thaliana Reveals a Novel N-Terminal Helical Extension." *Acta Crystallographica Section D: Biological Crystallography* 70(5): 1411–18.

Reeder, Brandon J., Dimitri A. Svistunenko, and Michael T. Wilson. 2011. "Lipid Binding to Cytoglobin Leads to a Change in Haem Co-Ordination: A Role for Cytoglobin in Lipid Signalling of Oxidative Stress." *The Biochemical journal* 434(3): 483–92.

Reeder, Brandon J., and John Ukeri. 2018. "Strong Modulation of Nitrite Reductase Activity of Cytoglobin by Disulfide Bond Oxidation: Implications for Nitric Oxide Homeostasis." *Nitric Oxide - Biology and Chemistry* 72: 16–23.

Reuss, Stefan et al. 2016. "Distribution of Cytoglobin in the Mouse Brain." *Frontiers in neuroanatomy* 10(April): 47.

Rhodes, Maria M, Kamila Réblová, Jiří Šponer, and Nils G Walter. 2006. "Trapped Water Molecules Are Essential to Structural Dynamics and Function of a Ribozyme." *Proceedings of the National Academy of Sciences* 103(36): 13380–85.

Ringe, Dagmar, Gregory A. Petsko, David E. Kerr, and Paul R.Ortiz de Montellano. 1984. "Reaction of Myoglobin with Phenylhydrazine: A Molecular Doorstop." *Biochemistry* 23(1): 2–4.

Roesner, Anja, Christine Fuchs, Thomas Hankeln, and Thorsten Burmester. 2005. "A Globin Gene of Ancient Evolutionary Origin in Lower Vertebrates: Evidence for Two Distinct Globin Families in Animals." *Molecular Biology and Evolution* 22(1): 12–20.

Romero, Natalia et al. 2003. "Reaction of Human Hemoglobin with Peroxynitrite. Isomerization to Nitrate and Secondary Formation of Protein Radicals." *Journal of Biological Chemistry* 278(45): 44049–57.

Rosenheck, K, and P Doty. 1961. "The Far Ultraviolet Absorption Spectra of Polypeotide and Protein Solutions and Their Dependence on Conformation." *Proc. Natl. Acad. Sci. USA* 47: 1775–85.

Rostkowski, Micha, Mats HM Olsson, Chresten R. Søndergaard, and Jan H. Jensen. 2011. "Graphical Analysis of PH-Dependent Properties of Proteins Predicted Using PROPKA." *BMC Structural Biology* 11.

Sali, Andrej et al. 1995. "Evaluation of Comparative Protein Modeling by MODELLER." *Proteins: Structure, Function and Genetics* 23(3): 318–26.

de Sanctis, Daniele et al. 2004a. "Mapping Protein Matrix Cavities in Human Cytoglobin through Xe Atom Binding." *Biochemical and Biophysical Research Communications* 316(4): 1217–21.

———. 2004b. "Mapping Protein Matrix Cavities in Human Cytoglobin through Xe Atom Binding." *Biochemical and biophysical research communications* 316(4): 1217–21.

Savard, Pierre Yves et al. 2011. "Structure and Dynamics of Mycobacterium Tuberculosis Truncated Hemoglobin N: Insights from NMR Spectroscopy and Molecular Dynamics Simulations." *Biochemistry* 50(51): 11121–30.

Savino, Carmelinda et al. 2009. "Pattern of Cavities in Globins: The Case of Human Hemoglobin." *Biopolymers - Peptide Science Section* 91(12): 1097–1107.

Schmidt, Marc et al. 2003. "How Does the Eye Breathe? Evidence for Neuroglobin-Mediated Oxygen Supply in the Mammalian Retina." *Journal of Biological Chemistry* 278(3): 1932–35.

———. 2004. "Cytoglobin Is a Respiratory Protein in Connective Tissue and Neurons, Which Is Up-Regulated by Hypoxia." *Journal of Biological Chemistry* 279(9): 8063–69.

Scholtz, J Martin et al. 1991. "Calorimetric Determination of the Enthalpy Change for the A-Helix to Coil Transition of an Alanine Peptide in Water." *Biochemistry* 88: 2854–58.

Scott, Emily E., Quentin H. Gibson, and John S. Olson. 2001. "Mapping the Pathways for O2 Entry Into and Exit from Myoglobin." *Journal of Biological Chemistry* 276(7): 5177–88.

Shaw, R. J. et al. 2006. "Promoter Methylation of P16, RARβ, E-Cadherin, Cyclin A1 and Cytoglobin in Oral Cancer: Quantitative Evaluation Using Pyrosequencing." *British Journal of Cancer* 94(4): 561–68.

———. 2009. "Cytoglobin Is Upregulated by Tumour Hypoxia and Silenced by Promoter Hypermethylation in Head and Neck Cancer." *British Journal of Cancer* 101(1): 139–44.

Shikama, Keiji. 1998. "The Molecular Mechanism of Autoxidation for Myoglobin and Hemoglobin: A Venerable Puzzle." *Chemical Reviews* 98(4): 1357–74.

Shiro, Yoshitsugu et al. 1994. "Spectroscopic Study of Ser92 Mutants of Human Myoglobin: Hydrogen Bonding Effect of Ser92 to Proximal His93 on Structure and Property of Myoglobin." *Biochemistry* 33(50): 14986–92.

Shiva, Sruti et al. 2007. "Deoxymyoglobin Is a Nitrite Reductase That Generates Nitric Oxide and Regulates Mitochondrial Respiration." *Circulation Research* 100(5): 654–61.

Shivapurkar, Narayan et al. 2008. "Cytoglobin, the Newest Member of the Globin Family, Functions as a Tumor Suppressor Gene." *Cancer Research* 68(18): 7448–56.

Smerdon, Stephen J. et al. 1993. "Serine92 (F7) Contributes to the Control of Heme Reactivity and Stability in Myoglobin." *Biochemistry* 32(19): 5132–38.

Song, Yifan et al. 2013. "High-Resolution Comparative Modeling with RosettaCM." *Structure* 21(10): 1735–42.

Šrajer, Vukica et al. 1996. "Photolysis of the Carbon Monoxide Complex of Myoglobin: Nanosecond Time- Resolved Crystallography." *Science* 274(5293): 1726–29.

———. 2001. "Protein Conformational Relaxation and Ligand Migration in Myoglobin: A Nanosecond to Millisecond Molecular Movie from Time-Resolved Laue X-Ray Diffraction." *Biochemistry* 40(46): 13802–15.

Storz, Jay F., Juan C. Opazo, and Federico G. Hoffmann. 2011. "Phylogenetic Diversification of the Globin Gene Superfamily in Chordates." *IUBMB Life* 63(5): 313–22.

Sugimoto, Hiroshi et al. 2004. "Structural Basis of Human Cytoglobin for Ligand Binding." *Journal of molecular biology* 339(4): 873–85.

Sun, Yunjuan et al. 2001. "Neuroglobin Is Up-Regulated by and Protects Neurons from Hypoxic-Ischemic Injury." *Proceedings of the National Academy of Sciences of the United States of America* 98(26): 15306–11.

———. 2003. "Neuroglobin Protects the Brain from Experimental Stroke in Vivo." *Proceedings of the National Academy of Sciences* 100(6): 3497–3500.

Teale, F. W. 1959. "Cleavage of the Haem-Protein Link by Acid Methylethylketone." *Biochimica et Biophysica Acta* 35: 543.

Tejero, Jesús et al. 2016. "Peroxidase Activation of Cytoglobin by Anionic Phospholipids: Mechanisms and Consequences." *Biochimica et Biophysica Acta - Molecular and Cell Biology of Lipids* 1861(5): 391–401.

Thuy, Le Thi Thanh et al. 2016. "Absence of Cytoglobin Promotes Multiple Organ Abnormalities in Aged Mice." *Scientific reports* 6(April): 24990.

Tilton, Robert F., Irwin D. Kuntz, and Gregory A. Petsko. 1984. "Cavities in Proteins: Structure of a Metmyoglobin-Xenon Complex Solved to 1.9 Å." *Biochemistry* 23(13): 2849–57.

Tiso, Mauro et al. 2011. "Human Neuroglobin Functions as a Redox-Regulated Nitrite Reductase." *Journal of Biological Chemistry* 286(20): 18277–89.

Tiwari, Purushottam Babu et al. 2015. "Characterization of Molecular Mechanism of Neuroglobin Binding to Cytochrome c: A Surface Plasmon Resonance and Isothermal Titration Calorimetry Study." *Inorganic Chemistry Communications* 62: 37–41.

Traylor, Teddy G., and Vijay S. Sharma. 1992. "Why Nitric Oxide?" *Biochemistry* 31(11): 2847–49.

Trent, James T., and Mark S. Hargrove. 2002. "A Ubiquitously Expressed Human Hexacoordinate Hemoglobin." *Journal of Biological Chemistry* 277(22): 19538–45.

Tsujino, Hirofumi et al. 2014. "Disulfide Bonds Regulate Binding of Exogenous Ligand to Human Cytoglobin." *Journal of Inorganic Biochemistry* 135: 20–27.

Uzan, Julien et al. 2004. "Neuroglobin and Other Hexacoordinated Hemoglobins Show a Weak Temperature Dependence of Oxygen Binding." *Biophysical journal* 87(2): 1196–1204.

Vallone, Beatrice, Karin Nienhaus, Annemarie Matthes, et al. 2004. "The Structure of Carbonmonoxy Neuroglobin Reveals a Heme-Sliding Mechanism for Control of Ligand Affinity." *Proceedings of the National Academy of Sciences of the United States of America* 101(50): 17351–56.

Vallone, Beatrice, Karin Nienhaus, Maurizio Brunori, and G Ulrich Nienhaus. 2004. "The Structure of Murine Neuroglobin: Novel Pathways for Ligand Migration and Binding." *Proteins* 56(1): 85–92.

Vinogradov, Serge N., and Luc Moens. 2008. "Diversity of Globin Function: Enzymatic, Transport, Storage, and Sensing." *Journal of Biological Chemistry* 283(14): 8773–77.

Vos, Marten H. 2008. "Ultrafast Dynamics of Ligands within Heme Proteins." *Biochimica et Biophysica Acta - Bioenergetics* 1777(1): 15–31.

Wakasugi, Keisuke, Tomomi Nakano, and Isao Morishima. 2003. "Oxidized Human Neuroglobin Acts as a Heterotrimeric Galpha Protein Guanine Nucleotide Dissociation Inhibitor." *Journal of Biological Chemistry* 278(38): 36505–12.

Wang, Bing, Leonard M. Thomas, and George B. Richter-Addo. 2016. "Organometallic Myoglobins: Formation of Fe–carbon Bonds and Distal Pocket Effects on Aryl Ligand Conformations." *Journal of Inorganic Biochemistry* 164: 1–4.

Weber, G., and F. J. W. Teale. 1959. "Electronic Energy Transfer in Haem Proteins." *Discussion of the Faraday Society* 27: 134–41.

Weissbluth, M. 1974. *Hemoglobin. Cooperativity and Electronic Properties.* eds. A. Kleinzeller, G. F. Springer, and H. G. Wittmann. New York: Springer-Verlag.

Wittenberg, Beatrice A., and Jonathan B. Wittenberg. 1987. "Myoglobin-Mediated Oxygen Delivery to Mitochondria of Isolated Cardiac Myocytes." *Proceedings of the National Academy of Sciences of the United States of America* 84(21): 7503–7.

Wittenberg, Jonathan B., and Beatrice A. Wittenberg. 1990. "Mechanisms of Cytoplasmic Hemoglobin and Myoglobin Function." *Annual Review of Biophysics and Biophysical Chemistry* 19: 207–41.

Würth, Christian et al. 2013. "Relative and Absolute Determination of Fluorescence Quantum Yields of Transparent Samples." *Nature Protocols* 8(8): 1535–50.

Xu, Jia, Guowei Yin, and Weihong Du. 2011. "Distal Mutation Modulates the Heme Sliding in Mouse Neuroglobin Investigated by Molecular Dynamics Simulation." *Proteins: Structure, Function and Bioinformatics* 79(1): 191–202.

Yang, Fan, and George N. Phillips. 1996. "Crystal Structures of CO-, Deoxy- and Met-Myoglobins at Various PH Values." *Journal of Molecular Biology* 256(4): 762–74.

Ye, S, C Shen, T M Cotton, and N M Kostić. 1997. "Characterization of Zinc-Substituted Cytochrome c by Circular Dichroism and Resonance Raman Spectroscopic Methods." *Journal of inorganic biochemistry* 65(3): 219–26.

Ye, Shi Qiao et al. 2009. "Silencing Neuroglobin Enhances Neuronal Vulnerability to Oxidative Injury by Down-Regulating 14-3-3γ." *Acta Pharmacologica Sinica* 30(7): 913–18.

Ye, Xiong et al. 2003. "Investigations of Heme Protein Absorption Line Shapes, Vibrational Relaxation and Resonance Raman Scattering on Ultrafast Time Scales." *Journal of Physical Chemistry A* 107(40): 8156–65.

Young, L., R. L. Jernigan, and D. G. Covell. 1994. "A Role for Surface Hydrophobicity in Protein-protein Recognition." *Protein Science*.

Yu, Z. et al. 2012. "Identification of Neuroglobin-Interacting Proteins Using Yeast Two-Hybrid Screening." *Neuroscience* 200: 99–105.

Zemel, Haya, and Brian M. Hoffman. 1981. "Long-Range Triplet-Triplet Energy Transfer within Metal-Substituted Hemoglobins." *Journal of the American Chemical Society* 103(5): 1192–1201.

Zhang, Jun et al. 2013. "Neuroglobin, a Novel Intracellular Hexa-Coordinated Globin, Functions as a Tumor Suppressor in Hepatocellular Carcinoma via Raf/MAPK/Erk." *Molecular pharmacology* 83(5): 1109–19.

Zhang, Shuning et al. 2017. "Cytoglobin Promotes Cardiac Progenitor Cell Survival against Oxidative Stress via the Upregulation of the NFκB/INOS Signal Pathway and Nitric Oxide Poduction." *Scientific Reports* 7(1): 1–13.

Zhang, Yong, Hiroshi Fujisaki, and John E. Straub. 2007. "Molecular Dynamics Study on the Solvent Dependent Heme Cooling Following Ligand Photolysis in Carbonmonoxy Myoglobin." *Journal of Physical Chemistry B* 111(12): 3243–50.

Zhang, Zhenyu et al. 2009. "Measurements of Heme Relaxation and Ligand Recombination in Strong Magnetic Fields." *Journal of Physical Chemistry B* 113(31): 10923–33.

Zhu, L, J T Sage, and P M Champion. 1994. "Observation of Coherent Reaction Dynamics in Heme Proteins." *Science (New York, N.Y.)* 266(5185): 629–32.

VITA

ANTONIJA TANGAR

2011	B.S. in Chemistry B.A. in Mathematics Valdosta State University, Georgia
2012	Quality Control Technician BASF Sparks, Georgia
2012-2018	Teaching/Graduate Assistant Florida International University Miami, Florida

SELECTED CONFERENCE PRESENTATIONS

"Probing the Role of Cytoglobin's Extended Termini".
Poster, 59th Annual Bophysical Society Meeting, 2015
Antonija Tangar, Sophie Bernad, Valerie Derrien, Pierre Sebban, Jaroslava Miksovska

"Determination of Ligand Migration Pathways in Human Cytoglobin"
Poster, 61st Annual Bophysical Society Meeting, 2017
Antonija Tangar, Michael Goncalves, Jessica Lopez, Sophie Bernad, Valerie Derrien, Pierre Sebban, Jaroslava Miksovska

"Determination of Ligand Migration Pathways in Human Cytoglobin"
Oral presentation, South Florida-ACS, 2017
Antonija Tangar, Michael Goncalves, Jessica Lopez, Sophie Bernad, Valerie Derrien, Pierre Sebban, Jaroslava Miksovska

"Reactivity of hexacoordinated heme proteins on ultrafast timescales"
Poster, 62nd Annual Bophysical Society Meeting, 2018
Antonija Tangar, Thomas Carlino, Shiori Yamazaki, Sophie Bernad, Valerie Derrien, Pierre Sebban, Amy M. Scott, Jaroslava Miksovska

"Photophysical characterization of zinc protoporphyrin IX-incorporated hexacoordinate hemoglobins"
Oral presentation, 20th Annual Biomedical and Comparative Immunology Symposium, FIU
Antonija Tangar, Sophie Bernad, Valerie Derrien, Pierre Sebban, Amy M. Scott, Jaroslava Miksovska